State estimation of a hexapod robot using a proprioceptive sensory system

E. Lubbe

21696888

Dissertation submitted in fulfilment of the requirements for the degree *Magister in Computer and Electronic Engineering* at the Potchefstroom Campus of the North-West University

Supervisors: Dr. K.R. Uren

Co-supervisor: Dr. D. Withey

November 2014

SUMMARY

The Defence, Peace, Safety and Security (DPSS) competency area within the Council for Scientific and Industrial Research (CSIR) has identified the need for the development of a robot that can operate in almost any land-based environment. Legged robots, especially hexapod (six-legged) robots present a wide variety of advantages that can be utilised in this environment and is identified as a feasible solution.

The biggest advantage and main reason for the development of legged robots over mobile (wheeled) robots, is their ability to navigate in uneven, unstructured terrain. However, due to the complicated control algorithms needed by a legged robot, most literature only focus on navigation in even or relatively even terrains. This is seen as the main limitation with regards to the development of legged robot applications. For navigation in unstructured terrain, postural controllers of legged robots need fast and precise knowledge about the state of the robot they are regulating. The speed and accuracy of the state estimation of a legged robot is therefore very important.

Even though state estimation for mobile robots has been studied thoroughly, limited research is available on state estimation with regards to legged robots. Compared to mobile robots, locomotion of legged robots make use of intermitted ground contacts. Therefore, stability is a main concern when navigating in unstructured terrain. In order to control the stability of a legged robot, six degrees of freedom information is needed about the base of the robot platform. This information needs to be estimated using measurements from the robot's sensory system.

A sensory system of a robot usually consist of multiple sensory devices on board of the robot. However, legged robots have limited payload capacities and therefore the amount of sensory devices on a legged robot platform should be kept to a minimum. Furthermore, exteroceptive sensory devices commonly used in state estimation, such as a GPS or cameras, are not suitable when navigating in unstructured and unknown terrain. The control and localisation of a legged robot should therefore only depend on proprioceptive sensors. The need for the development of a reliable state estimation framework (that only relies on proprioceptive information) for a low-cost, commonly available hexapod robot is identified. This will accelerate the process for control algorithm development.

In this study this need is addressed. Common proprioceptive sensors are integrated on a commercial low-cost hexapod robot to develop the robot platform used in this study. A state estimation framework for legged robots is used to develop a state estimation methodology for the hexapod

platform. A kinematic model is also derived and verified for the platform, and measurement models are derived to address possible errors and noise in sensor measurements. The state estimation methodology makes use of an Extended Kalman filter to fuse the robots kinematics with measurements from an IMU. The needed state estimation equations are also derived and implemented in Matlab®.

The state estimation methodology developed is then tested with multiple experiments using the robot platform. In these experiments the robot platform captures the sensory data with a data acquisition method developed while it is being tracked with a Vicon motion capturing system. The sensor data is then used as an input to the state estimation equations in Matlab® and the results are compared to the ground-truth measurement outputs of the Vicon system. The results of these experiments show very accurate estimation of the robot and therefore validate the state estimation methodology and this study.

Keywords

State estimation, Extended Kalman filter, Hexapod Robot, Legged Robot

ACKNOWLEDGEMENTS

Firstly I would like to give all the glory and honour to my Lord Jesus Christ and thank Him for always giving me strength during this study.

I would like to thank the CSIR for giving me the opportunity to further my studies. I would especially like to acknowledge the TSO operational group management and my TSO mentor, Stefan Kersop, for their involvement and contributions towards this study. I would also like to thank the MIAS operational group for the use of their Vicon system.

I would like extend my sincerest thanks and appreciation to my supervisor at the CSIR Dr. D. Withey, for sharing with me his vast amount of knowledge and experience in the field of robotics. I truly appreciate the passionate manner in which he helped and assisted me throughout the duration of my studies. His guidance and support was essential toward the success of this study. I would like to thank Dr. K.R. Uren, my university supervisor, from whom I have learned so much about the research process. His advice always have a way of calming your nerves and helping you to focus on the important things, not only with regards to the research but also in other aspects of life. I truly appreciate the effort and time he spend on helping me perfect this dissertation.

I would like to thank my husband Alwyn, for all of his love and support. This dissertation is dedicated to him. His encouragement and understanding carried me through the tough times. I would also like to thank my family and especially my parents, Wiaan, Ellie, Elsie and Francois for their support and understanding.

Table of Contents

LIST OF FIGURES

Chapter 2

Chapter 3

Chapter 4

Chapter 5

Chapter 7

Appendix B

LIST OF TABLES

Chapter 2

Chapter 3

Chapter 4

Chapter 7

LIST OF ABBREVIATIONS AND ACRONYMS

3D	Three dimensional
Bps	Bites per second
CAD	Computer-aided design
CSIR	Council for Scientific and Industrial Research
DOF	Degrees of freedom
DIY	Do it yourself
DPSS	Defence, Peace, Safety and Security
EKF	Extended Kalman filter
GPS	Global positioning system
ID	Identifier
IDE	Integrated development environment
IO	In-out
IMU	Inertial measurement unit
LiPo	Lithium Polymer
OCEKF	Observability Constrained Extended Kalman filter
PC	Personal computer
PSD	Power spectral density
pdf	Probability density function
PS2	Play Station 2
RC	Remote Control
RMS	Root mean square
ROS	Robot Operating System
SLAM	Simultaneous Localisation and Mapping
TTL	Transistor-transistor logic
UKF	Unscented Kalman filter
USB	Universal Serial Bus
VMCS	Vicon Motion Capture System

LIST OF SYMBOLS

Lower-case symbols	Unit	Description
$\boldsymbol{a}$	$\mathrm{m/s^2}$	Absolute acceleration
a	m	Link length
$\boldsymbol{b}$	-	Bias vector
b	-	Bias parameter
$\boldsymbol{b}_f$	$\mathrm{m/s^2}$	Acceleration bias
$\boldsymbol{b}_\omega$	rad/s	Angular rate bias
$b_{initial}$	-	Initial bias
b_{in_run}	-	In-run bias
d	m	Link offset
$exp(\cdot)$	-	Quaternion exponential map
$\boldsymbol{f}$	-	Process dynamics function or prediction model
$\boldsymbol{f}_{\boldsymbol{IMU}}$	g	IMU output acceleration quantity
$\boldsymbol{f}$	$\mathrm{m/s^2}$	Proper acceleration
$\tilde{\boldsymbol{f}}$	$\mathrm{m/s^2}$	Measured proper acceleration
$f(\cdot)$	-	Density of a variable
$\boldsymbol{g}$	$\mathrm{m/s^2}$	Gravity vector
g	$\mathrm{m/s^2}$	Physical unit of g-force acceleration
$\boldsymbol{g}_l$	$\mathrm{m/s^2}$	Local measured gravity vector
g_l	$\mathrm{m/s^2}$	Local gravitational acceleration
$\boldsymbol{h}$	-	Process observation or measurements model
h	m	Altitude above sea level
i	-	General index
k	s	Discrete time step
$\boldsymbol{kin}$	-	Kinematic model
$\boldsymbol{n}$	-	Measurement noise vector
$\boldsymbol{n}_i$	-	Transformed measurement noise quantity

$\boldsymbol{n}_s$	m	Discrete kinematic model Gaussian noise
$\boldsymbol{n}_\theta$	rad	Discrete joint position Gaussian noise
p	-	Probability
$\boldsymbol{p}$	m	Robot foot position
$\boldsymbol{q}$	-	Centre of robot body quaternion
$\hat{\boldsymbol{q}}$	-	Centre of robot body quaternion estimate
$\boldsymbol{r}$	m	Centre of robot body position
$\boldsymbol{s}$	m	Foot contact position vector with respect to $\boldsymbol{B}$
$\tilde{\boldsymbol{s}}$	m	Measured position vector of foot contact with respect to $\boldsymbol{B}$
t	s	Continuous time
Δt	s	Time step ($\Delta t = t_{k+1} + t_k$)
$\boldsymbol{u}$	-	Process input vector
$\mathbf{u}$	rad	Euler angle vector
$\boldsymbol{v}$	m/s	Centre of robot body velocity
$\boldsymbol{w}$	-	State noise vector
$\boldsymbol{w}_f$	$\mathrm{m/s^2}/\sqrt{\mathrm{Hz}}$	Continuous additive acceleration white Gaussian noise
$\boldsymbol{w}_\omega$	$\mathrm{rad/s}/\sqrt{\mathrm{Hz}}$	Continuous additive angular rate white Gaussian noise
$\boldsymbol{w}_{bf}$	$\mathrm{m/s^3}/\sqrt{Hz}$	Continuous white Gaussian noise (of acceleration bias)
$\boldsymbol{w}_{b\omega}$	$\mathrm{rad/s^2}/\sqrt{\mathrm{Hz}}$	Continuous white Gaussian noise (of angular rate bias)
$\boldsymbol{w}_p$	m	Foot slippage white noise term
$\boldsymbol{y}$	-	Measurements vector or measurement residual
$\hat{\boldsymbol{y}}$	-	Predicted measurement
$\boldsymbol{x}$	-	State vector
$\hat{\boldsymbol{x}}$	-	State estimate vector
$\hat{\boldsymbol{x}}^+$	-	Update or *a posteriori* state vector
$\hat{\boldsymbol{x}}^-$	-	Predict or *a priori* state vector
$\mathbf{x}$	-	Random variable
$\Delta\boldsymbol{x}$	-	Correction vector

Upper-case symbols	Unit	Description
$\boldsymbol{\mathcal{B}}$	-	Process input matrix
$\boldsymbol{B}$	-	Body coordinate frame
$\boldsymbol{C}$	-	Rotation matrix
E	-	Expected value
$\boldsymbol{F}$	-	Process dynamics matrix
$\boldsymbol{F}_c$	-	Continuous linearised error dynamics matrix
$\boldsymbol{F}_k$	-	Discrete linearised error dynamics matrix
$F(\cdot)$	-	Distribution a variable
$\boldsymbol{G}$	-	Translation vector operator
$G(\cdot)$	-	Gaussian distribution
$\boldsymbol{H}$	-	Process observations/measurements matrix
$\boldsymbol{I}$	-	Inertial coordinate frame
$\mathbb{I}$	-	Identity matrix
$\boldsymbol{J}$	-	Jacobian
$\boldsymbol{J}_{kin}$	-	Jacobian of the kinematic model
$\boldsymbol{K}$	-	Kalman gain matrix
$\widehat{\boldsymbol{K}}$	-	General axis rotation parameter
$\boldsymbol{L}_c$	-	Continuous noise Jacobian
L	°	Latitude
O	-	Origin of a frame
$\boldsymbol{P}$	m	Position vector
$\boldsymbol{\mathcal{P}}$	-	Covariance matrix
$\boldsymbol{\mathcal{P}}^+$	-	Update or *a posteriori* covariance matrix
$\boldsymbol{\mathcal{P}}^-$	-	Predict or *a priori* covariance matrix
$Q(\cdot)$	-	Quaternion matrix map
$\boldsymbol{Q}$	-	Process noise covariance matrix
$\boldsymbol{Q}_c$	-	Continuous process noise covariance matrix
$\boldsymbol{Q}_k$	-	Discrete process noise covariance matrix
$\boldsymbol{Q}_{bf}$	-	Covariance matrix for the noise term $\boldsymbol{w}_{\boldsymbol{bf}}$

$\boldsymbol{Q}_{b\omega}$	-	Covariance matrix for the noise term $\boldsymbol{w_{b\omega}}$
$\boldsymbol{Q}_{f}$	-	Covariance matrix for the noise term $\boldsymbol{w_{f}}$
$\boldsymbol{Q}_{\omega}$	-	Covariance matrix for the noise term $\boldsymbol{w_{\omega}}$
$\boldsymbol{R}$	-	Measurement noise covariance matrix
$\boldsymbol{R}_{i}$	-	Covariance matrix for the measurement noise quantity $\boldsymbol{n}_{i}$
$\boldsymbol{R}_{s}$	-	Covariance matrix for the noise term $\boldsymbol{n_{s}}$
$\boldsymbol{R}_{\theta}$	-	Covariance matrix for the noise term $\boldsymbol{n}_{\theta}$
$\mathbb{R}$	-	Real number
R	-	Resistor variable
$\boldsymbol{S}$	-	Residual covariance matrix
$\boldsymbol{T}$	-	Transformation matrix operator
V	-	Voltage variable
$\widehat{\boldsymbol{X}}$	-	X-axis unit vector
$\hat{X}$	-	X-axis orientation descriptor
$\widehat{\boldsymbol{Y}}$	-	Y-axis unit vector
$\hat{Y}$	-	Y-axis orientation descriptor
$\widehat{\boldsymbol{Z}}$	-	Z-axis unit vector
$\hat{Z}$	-	Z-axis orientation descriptor

Greek symbols	**Unit**	**Description**
α	rad or °	Link twist
β	-	Rotation variable
$\boldsymbol{\Gamma}$	-	Auxiliary quantity
$\boldsymbol{\delta b}_{f}$	$\mathrm{m/s^2}$	Acceleration bias error vector
$\boldsymbol{\delta b}_{\omega}$	rad/s	Angular rate bias error vector
$\boldsymbol{\delta x}$	-	State error vector
$\boldsymbol{\delta p}$	m	Robot foot position error vector
$\boldsymbol{\delta q}$	-	Centre of robot body quaternion error vector
$\boldsymbol{\delta r}$	m	Centre of robot body position error vector

$\boldsymbol{\delta v}$	$\mathrm{m/s}$	Centre of robot body velocity error vector
$\boldsymbol{\delta \phi}$	rad	Centre of robot body rotation error vector
η	-	Mean
θ	rad or °	General angle variable
θ_{servo}	rad or °	Joint position measured by position sensor
$\theta_{translated}$	rad or °	Translated joint position
$\boldsymbol{\theta}$	rad	Joint angles vector
$\widetilde{\boldsymbol{\theta}}$	rad	Joint position measurement vector
σ	-	Standard deviation
σ^2	-	Variance
$\boldsymbol{\phi}$	rad	Rotation vector
$\boldsymbol{\omega}$	$\mathrm{rad/s}$	Angular rate
$\widetilde{\boldsymbol{\omega}}$	$\mathrm{rad/s}$	Measured angular rate
$\boldsymbol{\Omega}$	-	Vector to 4×4 matrix map

Additional superscript	**Description**
$\times$	Skew-symmetric operator
T	Matrix or vector translation operator
-1	Inverse
^	Estimate
$+$	Update or *a posteriori* state
$-$	Predict or *a priori* state

Additional subscript	**Description**
c	Continuous
d	Discrete
V	Vicon reference frame

Chapter 1: Introduction

"Growth means change and change involves risk,

stepping from the known to the unknown."

~ Author Unknown

1.1 Background

The Defence, Peace, Safety and Security (DPSS) competency area within the Council for Scientific and Industrial Research (CSIR) has identified the need for the development of a robot that can operate in almost any land-based environment. Legged robots present a wide variety of advantages that can be utilised in this environment and is identified as a feasible solution. In comparison to other legged robots, hexapod (six-legged) robots exhibit robustness, even with leg defects. They can maintain static stability on a minimum of three legs and can support more weight than bipeds (two-legged) and quadrupeds (four-legged).

The biggest advantage and main reason for the development of legged robots, is their ability to navigate in uneven, unstructured terrain. However, upon investigation it was found that most literature only focus on legged robots walking on relatively even terrain. This limitation surfaced due to the complicated control algorithms needed in order for a legged robot to navigate in unstructured environments. Such control algorithms need to deal with static and dynamic stability of the robot, terrain model acquisition, path and adaptive feet trajectory planning as well as energy consumption minimisation, to name a few. The performance of these control algorithms rely on accurate sensory data and reliable state estimation.

The research and development of control algorithms for legged robots are constrained by the time and effort spend on the development of a robot platform with reliable state estimation. This statement is further validated by [1], where, it is stated that economic and human resources are taken away from the main focus of a robotic project due to research relying on custom designed hardware. The need for the development of a reliable state estimation framework for a low-cost, commonly available hexapod platform is identified. This will accelerate the process for control algorithm development.

Even though state estimation for mobile robots has been researched thoroughly, limited research is available on state estimation with regards to legged robots. Navigation in unstructured terrain increases the demands on state estimation for legged robots. Postural controllers of a legged robot need fast and precise knowledge about the state of the robot they are regulating [2]. In contrast to mobile robots, six degrees of freedom pose information about the robot base is needed in order to control a legged robot [3]. This is because locomotion of a legged robot makes use of intermittent ground contacts, making stability a main concern.

The sensory devices used for state estimation of legged robots is also a topic of concern. Since legged robots have limited payload capacities, any extra devices on the robot, including sensory devices, should be kept to a minimum. Furthermore, exteroceptive sensory devices commonly used in state estimation, such as a GPS or cameras, are not suitable when navigating in unstructured terrain [3]. Not only is the information they provide not accurate enough for stability control of a legged robot, loss of signal with regards to a GPS, or loss of light with regards to a camera, will induce errors in the state estimation. The control and localisation of a legged robot should therefore only ***depend*** on proprioceptive (internal) sensors. (Exteroceptive sensors can be used to improve the state estimation done by proprioceptive sensors, but control and localisation should not rely on exteroceptive information.)

1.2 Problem statement

The purpose of this study is to develop and implement a state estimation methodology of a hexapod robot platform using only proprioceptive sensors. Emphasis is placed on the contribution this study will make towards future projects focussing on control approaches for a hexapod robot platform. The methodology will be implemented on a low-cost commercially available hexapod robot by using commonly available proprioceptive sensors.

The study will require the development of a hexapod platform by integrating one commercially available hexapod robot with a sensory system. The sensory system will consist of a combination of proprioceptive sensors needed for the state estimation. A method for the sensor data acquisition will also be derived and implemented. For state estimation, a kinematic model of the robot platform is essential.

Different state estimation frameworks for legged robots will be studied in order to derive the state estimation equations needed for the hexapod platform. The state estimation equations should provide accurate six degrees of freedom information about the robot base to make it usable for

stability control. The state estimation equations will be implemented and validated for the developed robot platform.

1.3 Issues to be addressed and methodology

In this study, the state estimation of a hexapod robot using a proprioceptive sensory system, can be divided into five main components:

The first component involves the acquisition of a hexapod robot. The design of the robot will directly influence its capabilities. Through a literature study, knowledge on the mechanical characteristics and the impact these characteristics have on a robot's performance will be obtained. Thereafter, different commercially available hexapod robots will be compared in order to determine the best solution. Factors like the robot's size, payload capabilities, quality, cost and available information will need to be considered. The ease with which the software and hardware of the robot can be modified, will also be investigated.

The second component involves a study on state estimation. Common state estimation algorithms will be studied. An in-depth review about different state estimation frameworks for legged robots to be conducted. From this review, a possible approach for the state estimation of this study will be identified.

The third component involves the sensory system. A review on hexapod sensory systems will be conducted in order to identify the common sensory devices needed by hexapod robots. Taking into consideration the possible state estimation approach, different sensor types needed for the state estimation will be identified. Sensory specifications will be investigated and sensory devices will be acquired. The sensory devices will then be integrated onto the commercial robot along with a single board computer that will handle the sensor data acquisition. A software program for the data acquisition will be developed.

The fourth component involves the state estimation approach. The state estimation equations will be derived for the hexapod platform. The equations will be implemented in Matlab®. Using the sensor data of the robot platform, the state estimation methodology will be evaluated.

The fifth and last component involves the validation of the study. Here, emphasis will be placed on the verification of the state estimation equations and the validation of the state estimation methodology. The accuracy of the kinematic model derived will also be verified.

1.4 Contributions made by the study

The completion of this study will introduce a number of contributions. The use of an inexpensive (hobby class) commercially available hexapod platform plays an important role in the value of this study. This allows anyone to implement the findings in this study and as a result have a platform on which control algorithms can be developed, implemented and tested. This is also true with respect to the development of the sensory system where low-cost commercially available sensors will be implemented.

The state estimation framework presented in, *"State estimation for legged robots – Consistent fusion of leg kinematics and IMU."* by Bloesch et al. [2] will play a major role in this study. Although it is stated that their Observability Constrained Extended Kalman filter (OCEKF) can be implemented for state estimation on various kinds off legged robots, simulations and physical tests were only conducted on a quadruped robot by Bloesch et al. [2]. Recently, a simulation test was also conducted on a humanoid by Rotella et al. [3]. In this study, this state estimation framework will, to the best of the author's knowledge, for the first time be adopted for a hexapod and tested with a physical hexapod robot.

Results in the paper presented by Bloesch et al. [2] indicated a drift in the position estimation due to inaccurate leg kinematics as well as fault-prone feet contact detection. By integrating force sensors in the hexapod's feet, one can eliminate any uncertainties and errors created by faulty feet contact detection. Furthermore, for the implementation of the state estimation, the full kinematic model for the chosen hexapod robot (PhantomX) will be mathematically derived. To the best of the author's knowledge, this derivation has not been published.

1.5 Validation and verification

In order to verify the derived kinematic model, the robot platform will be modelled as an assembly in SolidWorks®. For specific joint angle inputs the SolidWorks® model's foot position results will be compared to the kinematic model's results. The results obtained from the SolidWorks® model should be comparable to those of the kinematic model.

The state estimation of the hexapod robot will be validated with a number of physical experiments involving the robot platform and a Vicon Motion Capture System (VMCS) [4]. Vicon systems are commonly used throughout the research community to capture motion due to its extreme accuracy. The Vicon system that will be used consists of twelve cameras that track rigid bodies in 3D space and capture the information on a network to be used in a Robot Operating System (ROS).

A number of experiments will be conducted using the Vicon system and at the same time recording the state estimation computed by the filter for the robot. The estimated position, velocity, roll, pitch and yaw of the centre of the robot's body will then be evaluated with a comparison to the ground truth measurements provided by the Vicon system.

1.6 Overview of dissertation

Chapter 2 contains a detailed literature review that provides background with respect to the focus of this study. Important terminology and concepts that were used throughout this study are introduced and discussed. From the information provided in Chapter 2, the need for this study is identified and a detailed problem statement is derived.

Chapter 3 contains a detailed literature study on specific topics that were identified in Chapter 2. Trade-off studies are conducted to support platform and sensory device decisions that were made in this study. Common state estimation algorithms are discussed and an in-depth literature study about state estimation for legged robots is provided. The main state estimation framework implemented in this study is also identified.

The kinematic model needed for the state estimation of the robot platform is derived in Chapter 4. A leg kinematic model is firstly derived for the legs of the robot platform. The kinematic model, which describes the forward kinematics of the robot platform, is then derived by transforming the leg kinematic model into the body coordinate frame. The kinematic measurement model used to describe specific noise processes needed by the state estimation, is also derived in Chapter 4.

Chapter 5 discusses the specific sensory devices that are integrated onto the robot platform to perform the state estimation. The method chosen to acquire the sensor data is also discussed. For each sensory device the measurement model, describing the noise processes needed for the state estimation, is also derived.

The derivation of the state estimation approach is discussed in Chapter 6. With the use of the kinematic model, derived in Chapter 4, and the measurement models, derived in Chapter 4 and 5, the specific algorithm that is used for the state estimation of the hexapod robot platform is derived. The algorithm fused the kinematics with the sensory data to produce the full body estimate of the robot.

Chapter 7 discusses implementation and results with respect to this study. Firstly, the kinematic model derived in Chapter 4 is verified. The implementation of the state estimation algorithm is then

discussed. The state estimation approach is also validated with multiple experiments that are compared to ground truth measurements.

In Chapter 8 the dissertation is concluded with a summary of the study outcomes. Possible improvements are identified and areas for future work are discussed.

Chapter 2: Literature survey

"In literature and in life we ultimately
pursue, not conclusions, but beginnings."
~ *Sam Tanenhaus*

2.1 Introduction

Chapter 2 contains a literature survey of research related to this study. Specific background information that led to the author's inspiration to conduct this study as well as vital terminology and concepts are discussed. The chapter contains background information regarding hexapod robots, important topics surrounding them, hexapod applications as well as their limitations. Literature regarding the importance of sensory systems, their application in hexapod robots as well as the sensory feedback expected for a hexapod robot is also discussed. The chapter concludes by addressing the importance of state estimation for a robot. Here, sensor integration and interpretation, more specifically, multiple sensors as an information source and multisensor data fusion, is discussed.

2.2 Background

The field of biomimetic robotics, where biological creatures are used as inspiration for innovative robot design has been steadily developing throughout the years. The mimicking of biological creatures in terms of their functionality, movement, operation and intelligence has played a vital role in developing more advanced robots and using them for advanced applications. This is especially evident with regards to legged robots.

Research conducted in 1986 identified the need for exploring legged robots based on two motivations [5]. The first is mobility, based on the need for locomotion in uneven, unstructured terrain. This includes the idea that the path of the feet or legs of the robot can be decoupled from the path of the body or trunk, and therefore legged robots can provide a smooth and stable environment for a payload on a robot. The second motivation is that it will advance and contribute to the better understanding of biological creature locomotion.

A great number of research and development have been done in the last decade on multi-legged robots. Some of the more common configurations are humanoids (two-legged), quadrupeds (four-legged), hexapods (six-legged) and even octopods (8 legged). The increasing level of capabilities that are being developed with regards to legged robots has boundless potential. As a result of this, countless fields, even space science [6], have identified it and are developing legged robot projects. However, there are still a lot of limitations and problems to overcome regarding legged robots that need to be resolved by applied research. These limitations are identified and discussed throughout this literature survey and will provide the reader with context with regard to the derivation of the specific research problem addressed in this study.

2.3 Hexapod robots

This section provides background on hexapod robots. It discusses important topics surrounding them as well as the current hexapod applications available. The section concludes with a discussion on the current hexapod limitations which emphasises the need for this study.

2.3.1 Background

A hexapod robot is a multi-legged robot that walks on six legs. This type of robot shows great advantages, not only over wheeled robots, but also over other legged robots. This is mainly due to the fact that they can easily maintain static stability on a minimum of three legs, allowing them to have a large range of possible movements. It also provides them with the ability to operate on as little as three legs while their remaining limbs can be utilised for other tasks. Hexapod robots are also more efficient for statically stable walking than other legged robots [7].

The speed of a statically stable legged robot is theoretically dependent on its number of legs. It is known that statically stable legged robots already move slow, therefore it is seen as a big advantage that a hexapod will be faster than a quadruped and a humanoid [8]. Hexapod robots further exhibit robustness, even with leg defects and can support more weight than bipeds and quadrupeds. Their robustness and abilities make them the better choice for a broader variety of applications in comparison to other types of legged robots [9]. For these reasons, hexapod robots were chosen over other legged and wheeled robots for this study.

2.3.2 Important topics surrounding hexapod robots

2.3.2.1 Design

A substantial amount of research focuses on the modelling and design of hexapod robots [10]. Most of the developments made in the design of the physical body are inspired from insects and animals [11]–[13]. The design of a hexapod robot has a direct influence on its capabilities. The body shape influences features like the static stability whereas the leg distribution can influence the size of the actuator required [8]. For a legged robot, the robot is in a *static stable* condition if the centre of gravity is within the tripod (made by the three ground contact points of the feet) of ground contact [14].

Hexapod robots are typically divided into two categories describing their body, (or trunk) shape and leg distribution. The first is known as *hexagonal* or *circular* and have six axisymmetrically dispersed legs. The second classification has six symmetrically dispensed legs on two sides and is known as *rectangular* [7]. Fig. 2.1 shows a two dimensional top view of both these categories.

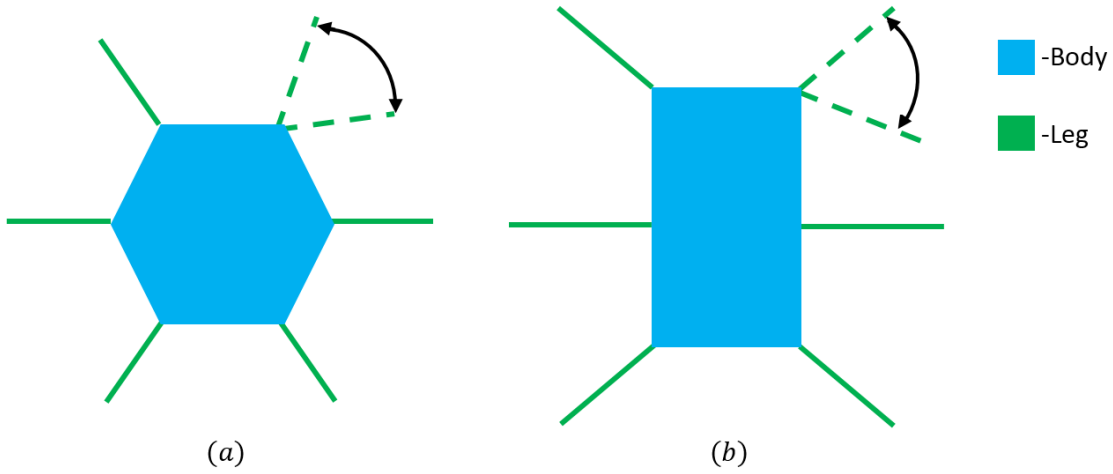

Figure 2. 1: Hexapod configurations: hexagonal (a) and rectangular (b).

Most of the initial research and development done on hexapod robots was based on the rectangular configuration and were biologically-inspired by research conducted specifically on the cockroach and stick insect [13]. Although most research and development is still being done on the rectangular configuration, researchers has also started looking at the hexagonal configuration for the advantages it has with respect to turning gait [9].

2.3.2.2 Control

In order for any robot to perform a task it has to be controlled by a control system. Whether a robot is just remotely operated to move in a direction or operating completely autonomously, some kind of

control system needs to be present. A robot control system consists of many sub-control systems that can be open- or closed-loop. For a control system of a hexapod walking over uneven terrain it is important that, for example, the legs are controlled with a closed-loop feedback system. Such a closed-loop feedback system will make use of a sensory system providing measurements from a number of different sensors as well as reliable real-time estimates of the robot's state. This will allow the robot to balance itself and stay stable.

A number of studies on hexapod robots involve the development and testing of control algorithms that minimise the robot's energy consumption [15], plan adaptive footholds [16] and stabilise the robot while walking [10]. These algorithms all make use of the robot's sensory system to provide them with the necessary sensory feedback for state estimation. *The sensory system is therefore considered the feedback foundation, and the state estimation, the information foundation for the control of a robot*. The sensory feedback used for control in hexapod applications will be discussed later in this chapter.

2.3.2.3 Locomotion

Locomotion is one of the most important topics when it comes to robots. *Locomotion* of a robot describes the robot's ability to move. *Gait locomotion* of multi-legged robots is the sequence of movement of the legs, thus the sequence of how and when the legs are lifted. *Foothold planning* for locomotion is how and where the feet are placed to position the robot as best as possible to achieve its goal.

Gait or locomotion planning is one of the most studied problems found in multi-legged robots [3, 5]. This is mainly due to the fact that it is not possible for a remote operator to manually define each leg's movement while the robot is walking. The operator of the robot can define where the robot should go or give the robot a specific goal, but the foothold planning and leg trajectories should be done on-board [17]. Different possible gaits for different situations have been studied by analysing hexapod locomotion [7].

Some of the most common gait patterns that are implemented to provide hexapod robots with locomotion are shown in Fig. 2.2. The black bars in Fig. 2.2 indicate the leg swing for the right-sided legs, R1-R3, and the left-sided legs, L1-L3, over time.

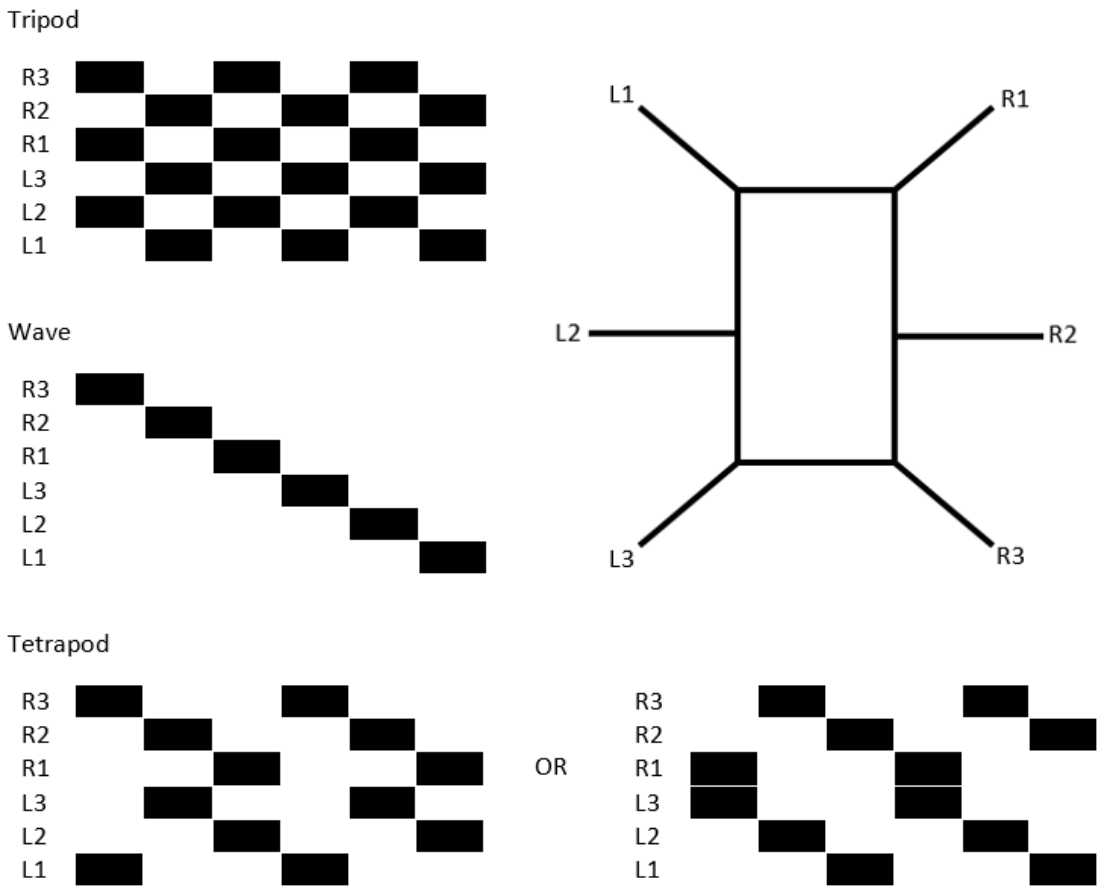

Figure 2. 2: Common hexapedal gait patterns [18], [19].

2.3.3 Applications

Over the last few years a number of different hexapod applications have been developed. These robots differ in size, design, functionality and complexity. Most of these robots have been developed for a specific function or to achieve a specific goal. This is in accordance with the research done by Minati and Zorat [1], where they state that current robotic research mostly rely on custom designed hardware. It was found that commercially available solutions are either very expensive and lack flexibility, or amateur-level, lacking sufficient computational capabilities.

Some examples of the latest hexapod applications can be seen in Fig. 2.3. The Messor robot is a versatile walking robot used for search and rescue missions [20]. The SILO6 robot is used for humanitarian demining missions [8]. ATHLETE is a hybrid hexapod with wheels as feet and is used as a cargo and habitat transporter for the moon [21]. The DLR Crawler is an experimental hexapod platform used to test different control, gait and navigation algorithms on [22]. RHex [23] and X-RHex [24], [25] are high-mobility six-legged robots that uses only one actuator per leg to navigate over rough terrain and overcome obstacles such as stairs .

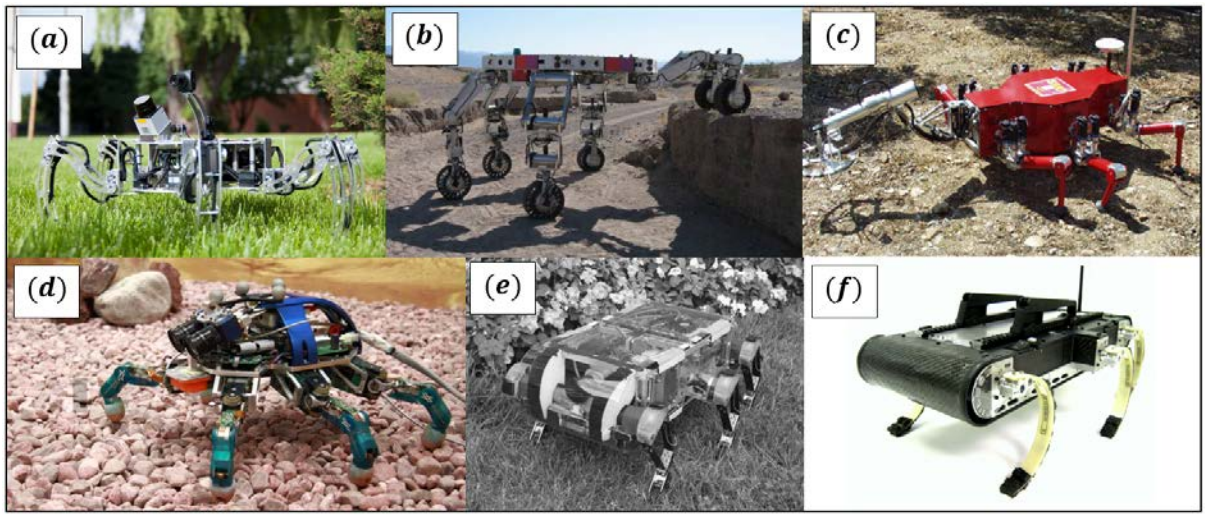

Figure 2. 3: Hexapod applications: (a) Messor [20], **(b) ATHLETE** [21], **(c) SILO6** [8], **(d) DRL Crawler** [22], **(e) RHex** [23], **(f) X-RHex** [24], [25].

2.3.4 Hexapod robot limitations

Even though multi-legged robots show great potential when it comes to handling rough terrain, most literature ignore this advantage and only focus on walking on flat or slightly uneven terrain where wheeled systems are superior [26]–[28]. This is due to complicated control algorithms that are needed for a multi-legged robot to navigate itself in uneven terrain. Such control algorithms usually deals with model acquirement of the terrain, path planning through the terrain, foothold selection and planning while moving through the terrain, feet and/or leg trajectories as well as static and dynamic stability [5], [16], [17].

Information needed by such a control algorithm has to be provided by a state estimation of the robot using a sensory system on or around the robot. A sensory system for a hexapod can consist of multiple sensors such as force, distance and vision sensors. These sensors and/or their data are usually fused together in state estimation algorithms to provide the control system with a broad range of information that can be interpreted. The design of sensory systems for hexapod robots are restricted by the limited payload, energy and the on-board computing power of the robot, as well as budget limits provided for projects [16].

In order to really take advantage of what a hexapod robot has to offer, a lot of research and development needs to be done on control algorithms that will optimise their performance and efficiency. Research showed that a lot of time has to be spent on developing a robot platform that has a good sensory system that provides real-time state estimates, before attempting the control of the system. This is also shown in [1] where it is stated that most robotic research in the industry and the

academia relies on custom designed hardware. This takes economic and human resources away from the main focus of a project. These constraints are seen as the biggest limitation for hexapod development and might serve as demotivation to developers focussing on specific problems like control algorithms.

Considering the background given regarding hexapod research, it is evident that the development of the control algorithms for a hexapod depends on the mechanical design (kinematics) and the available sensory and state estimation information. The role and importance of a sensory system on a robot will now be discussed to substantiate the research problem.

2.4 Sensory systems

A sensory system in a robot is responsible for processing and providing sensory measurements that can also be used to provide state estimation information. *The main goal of a sensory system can therefore be described as the transformation of the physical world into a representation where the information can be interpreted and used.*

This section discusses the importance of a sensory system in general, investigates sensory systems and the specific sensors found in hexapod applications, provides two different approaches to the development of a sensory system for a robot, and discusses the sensory system challenges regarding hexapod robots.

2.4.1 The importance of a sensory system

In the field of bionics we observe that animals and insects make use of different sensing mechanisms to sense their physical condition as well as the environment around them. Data from their sensing mechanisms can describe conditions such as forces generated, positions and movements of limbs, including the velocity of limb movements and acceleration of limbs [29]. The data collected by their sensing mechanisms is then used as information that will be utilised in their navigation judgement [30]. By looking at nature the importance of a sensory system is evident towards developing any form of intelligence.

Over the last few decades the sensory systems of insects have been studied and are used as inspiration in a biomimetic, (or bio-inspired) approach to solve engineering problems [29]. For the development of legged robots, the biomimetic approach has been shown to produce better solutions than the traditional engineering design methods. However, these solutions are still far from optimised when compared to the speed and agility of insects walking over uneven terrain. As discussed previously, the

importance of a sensory system is also made obvious when considering its necessity in any closed-loop robotic control system.

According to Siciliano and Khatib [31], sensing and estimation are crucial aspects in the design of any robotic system. Sensing and estimation for a robot can be divided into two categories. The first is *proprioception*, meaning, retrieving the state of the robot itself. The second is *exteroception*, meaning, retrieving the state of the environment or external world around the robot [31]. In order to acquire proprioception and exteroception, specific sensors and the integration of these sensors are needed.

The specific sensors needed in a sensory system for a hexapod robot will now be investigated, whereas the integration of those specific sensors will be discussed in the state estimation section of this chapter.

2.4.2 Sensory system for a hexapod robot

2.4.2.1 Sensory feedback in hexapod applications

Table 2.1 describes the goals of some relevant hexapod applications and provides the different sensors that are implemented on them to form their sensory system. This table provides a general summary to create context regarding sensory feedback for specific applications.

Table 2. 1: Summary of hexapod application goals and their sensors

Hexapod	**Goal**	**Sensors** (Proprioceptive = green text, exteroceptive = black text)
ANTON [12] 	Control development platform	• 24 Potentiometers installed in each joint. • 6 three-component force sensors mounted in each leg's shank. • 2-axis gyroscopic sensor located inside the body. • 2 mono cameras in the head of the robot.
LAURON IV [13] 	Inspection of environments not accessible for humans or wheeled robots.	• Three camera systems (stereo, omni-directional and time-of-flight) • Inertial sensor system • GPS sensors • 3D foot force sensors

		• Spring force sensors • Motor current sensors
Golem [1] 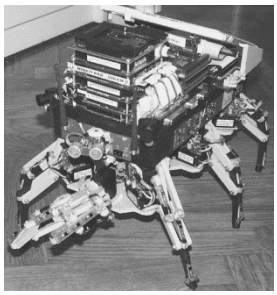	A flexible, scalable, general purpose development and experimenting tool targeted to academia, industry and defence environments.	• 4 sonar sensors • 39 infrared proximity detectors distributed over the entire structure. • Position and pressure feedback on all axes. • 4 accelerometers. • A two-axis magnetic compass. • 3 Hall Effect sensors. • 3 cameras. • 2 microphones.
SensoRHex [32] 	Dynamic locomotion at high speed over rough terrain.	• Gearhead/motor/encoder units. • Voltage/current/temperature sensors. • Hall Effect sensor. • Inertial measurement node. • Infrared distance measurement node.
Messor robot [20] 	Used for Urban Search and Rescue missions.	• Inertial measurement unit (3 accelerometers and 3 gyroscopes) • Resistive sensor to determine contact force with ground. • Current sensor to determine the torque in each joint. • Video camera • Laser Range Finder • Structural light system (vertical laser stripe used for stair climbing)

An overview will now be given on the commonly used types of sensors found in legged robotics. Their implementation, goals, importance and classification will be discussed:

Kinematic Sensors

Kinematic sensors in legged robots are sensors that can detect the position of a leg. Therefore, they are classified as proprioceptive sensors. Examples of such sensors include inclinometers that measure

the tilt or angle of an axis, motor/gearhead/encoder units that convert the angular position of the actuators, and other joint position sensors. Information provided by kinematic sensors can contribute to estimating the pose of a robot and is very important for the control of the robot [2].

Force Sensors

Force sensors in the form of resistive sensors are typically applied to the feet of legged robots. They are used to measure the force and torque extended on the robot's leg and to determine contact of the feet with the environment. The force and torque in different joints of legged robots can also be determined by current sensors on the actuator motors [20]. Force sensors are classified as proprioceptive sensors.

The information provided by force sensors can be used to ensure the operating safety of legged robots. For example, a sudden decrease in force or loss in friction can indicate that a leg is slipping. In order to ensure the safety of the actuating motors, the robots maximum payload can also be determined by force information [20], [33]. Force information and feedback is extremely important for the control of legged robots, especially for navigation in uneven terrain [27]. Kaliyamoorthy and Quinn [33] states that a force control strategy is more appropriate for legged robots navigating in unknown terrain, than a position control strategy.

IMU

An inertial measurement unit (IMU) or inertial sensor, classified as a proprioceptive sensor, is a device that is used in robotic applications to estimate relative position, velocity and acceleration. It usually consists of three orthogonal accelerometers and three orthogonal gyroscopes. Accelerometers measure external forces acting on a robot and gyroscopes measure changes in the orientation of a robot [31], [34]. The information from an IMU can therefore contribute to the estimation of a legged robot's body pose [2]. The combination of accelerometers and gyroscopes can be found in almost all legged robot applications.

GPS

The global positioning system (GPS) is another device that is very commonly found on robots that produce similar information than the IMU, but is usually classified as an exteroceptive sensor. A GPS is a satellite navigation system that usually provides location (global position) and time information to a robot used for its navigation. The information provided by a GPS is commonly fused with information from inertial measurement systems to improve position, velocity and acceleration estimation [35], [36].

Cameras

A camera is a device that records visual images and is classified as an exteroceptive sensor. Different types of cameras are commonly found on legged robots. Integrated onto a robot, these devices are usually used to provide information about the robots' surrounding environment. This information can be used to detect, avoid and even identify obstacles. Simultaneous Localisation and Mapping (SLAM) is also commonly implemented using cameras as sensors [20].

Distance measuring sensors

These include sensors such as laser range finders and infrared distance measuring and proximity detector sensors. Operating on the time of flight principle, these sensors send out light pulses and measure the time it takes for them to return to determine the distance to a structure. These kind of sensors are classified as exteroceptive sensors and are mainly used for map building and obstacle analysis [20].

2.4.2.2 Proprioceptive vs. exteroceptive sensors

The importance of the proprioceptive sensors in a legged robot becomes evident when comparing the relationship found between the amounts of proprioceptive sensors to the amounts of exteroceptive sensors found in Table 2.1. This is especially evident in the robot examples that are designed for application purposes as to those designed for research purposes.

For state estimation, it is commonly found that proprioceptive sensors, such as an IMU, are used in combination with exteroceptive sensors, such as a GPS [37]. However, the process of gathering information by using exteroceptive sensors can't be contained within the robot as in the case of proprioceptive sensors. Using exteroceptive sensors as important information sources to a system can introduce a lot of limitations. For example, a GPS can lose its signal due to bad weather or if the device is indoors, and a camera using light from the visual spectrum will not work in the dark. Most exteroceptive sensors can also be hacked or jammed resulting in untrustworthy information.

Using a proprioceptive sensory system for state estimation of a robot will reduce these limitations. Rotella et al. [3] states that for legged robots operating in unstructured environments, exteroceptive sensors are unfit and the task of control and localization should depend on proprioceptive sensors. However, by using proprioceptive sensors drift in the position estimate is inevitable since absolute position and heading can't be sensed directly [2], [37]. The limitations of the different sensors will need to be taken into consideration when a sensory system is developed.

2.4.3 Sensory system development for a hexapod robot

The development of a sensory system for a hexapod robot can be done by means of two different approaches, a systems engineering approach or a biomimetic approach. Both these approaches will now be discussed, focusing on their methods, limitations and advantages.

The approach taken by most researchers and developers towards the development of a sensory system for a robot can be summarised in the following sentence: The application and goal of a robot define the amount and types of sensors that are needed for the robot to operate successfully. This approach can be described as a systems engineering process [31]. This process includes an analysis of the system requirements, modelling the environment, determining the system behaviour under different conditions and lastly, selecting the suitable sensors.

After completing this process, the hardware components have to be assembled and the necessary software modules for the data fusion and interpretation have to be developed. The system is finally tested and its performance is analysed. Once the sensory system is constructed, the different components of the system have to be monitored for the purpose of analysis, debugging and testing. Quantitative measurements are also required in terms of robustness, system efficiency and time and space complexity.

Although this approach can deliver great results for a robot with a specific goal or function, it might not allow the extreme flexibility exhibited by animals. If the robot's control system is changed at a later stage, the sensory system might not provide the control system with the needed information in order for the robot to operate successfully [29].

The biomimetic designing approach does not consider a specific final purpose when designing or developing a project. Instead, it considers biological features. For legged robots, such as hexapods, they specifically try to mimic the sensory systems of insects. The main idea behind the biomimetic developing approach of a sensory system is based on the fact that biological sensors evolve through adaptation of existing functional capabilities and structures. This is explained with the following example; a legged creature has to be able to stand, walk and run with its legs, therefore its sensory feedback loops have to aid in all three of these activities [29].

When developing a biomimetic sensory system for a hexapod, two main challenges have to be addressed; choosing or designing adequate sensors that are appropriate, and the integration and interpretation of the sensors to ensure that the sensor signals can be used effectively. But this is not an easy task. Delcomyn [29] states that walking robots may require more redundancy and variation in their sensor arrays than what might seem necessary at first. In order to handle signals appropriately

and effectively, the signal processing must be flexible. This implies that certain feedback signals for some specific behaviour can be suppressed or dampened in order to prevent interference from them when other sensor information is more relevant at the specific time.

Although a biomimetic approach to the development of a sensory system for a hexapod might result in a more versatile platform solution, the complexity that goes together with this approach should not be taken lightly. The quest to mimic nature for better results can therefore be seen as a trade-off between accuracy and simplicity.

By comparing these two approaches one can make the following conclusion: The biomimetic and systems engineering approaches have to be combined in some sense. To avoid the development of an unnecessarily complex sensory system, the systems engineering approach to a minimum amount of sensors needed to be considered. However, some aspects of the biomimetic approach should be included in the development of a sensory system to insure the system stays flexible and allow future adjustments.

2.4.4 Sensory system challenges for a hexapod

For multi-legged robots, sensory systems should provide the robot with measurements to create a perception of the environment it is surrounded by and of the state of the robot. This should provide a legged robot with the information it will need to make decisions and adapt to its environment. Research done by Belter et al. [16] and Kalakrishnan et al. [28] describes terrain mapping and foothold selection as crucial to the successful navigation and stability of a legged robot. Neither one of these can be accomplished without measurements from multiple-sensors and the fusion of these sensors.

Allowing the fusion of multiple sensors is a challenge in the development of any sensory system. In fact, it is such a challenging problem that there exists a number of research fields dedicated to it. This will be addressed in the state estimation section of this chapter. The fusion of multiple-sensors is not the only challenge when it comes to developing a sensory system for a hexapod.

In order for a hexapod robot to be useful as a developing platform towards end applications, it has to operate in real-time. This is an increasingly complex problem in sensory system development due to added features like the use of many different types of sensors [31], [38], [39]. Software engineering issues that receive more attention due to this problem include real-time issues, reusability, using commercial off-the-shelf (COTS) components, reliability, embedded testing and sensor selection [31].

Other important factors to take into account when developing a sensory system for a hexapod include, as mentioned before, the limited payload of a robot, the available energy on the robot, the on-board computing power and the cost of the sensors [16].

2.5 State estimation of a robot

For a robot system, *state estimation* is a methodology which provides the best possible approximation for the robot's state by processing available information. It enables the estimation of unmeasured variables or parameters, filters out noise and predicts the system's future behaviour by combining the system information (provided by a mathematical model of the system) and on-line measurement information (provided by sensors).

In this section the importance of state estimation for legged robots is discussed. Due to its imperative role in state estimation, the integration and interpretation of sensors is also discussed. Here the focus is on providing background information on sensor fusion, a process where data from different sensors are fused together to reduce sensor errors and increase available information provided by sensors. The accuracy of, and information provided by a state estimation approach depends enormously on the sensor fusion techniques applied in the state estimation algorithm. An in-depth literature study on state estimation for legged robots is done in Chapter 3.

2.5.1 Importance of state estimation

For robotic systems, state estimation is vital for process monitoring, where important variables, such as velocity might not be directly measurable with enough accuracy. It is also important for control where a system model contains errors such as unmeasured disturbances. With this in mind, robotic systems mostly make use of state estimation for navigation and stability. For wheeled robots, state estimation algorithms typically fuses wheel odometry with an exteroceptive sensor such as a GPS to estimate the robot's absolute position and yaw. This is done in order to correct errors caused by, for example wheel slippage.

For the control of a legged robot, the state estimation has to provide information on the full six degrees of freedom pose of the base of the robot [3]. This translates to the pose in a three dimensional space which is, translation and rotation on three perpendicular axes. Six degrees of freedom pose estimation is especially important when the legged robot has to operate in rough, unstructured terrains with no prior knowledge about the environment. In contrast to wheeled robots, that are expected to stay stable and in contact with the ground at all times, legged robots interact with their

environment through intermittent ground contacts. Therefore, the controllers of the robot need fast and precise knowledge of the state of the robot in order for the robot to maintain stability[2], [3].

The needed knowledge for stability of a legged robot is supplied by means of state estimation that utilise a dynamic model of the robot to provide estimates of variables needed for pose calculation. In order to increase the accuracy of the pose estimation and at the same time eliminate any errors in sensor readings, multiple-sensors are used as information sources.

2.5.2 Sensory integration and interpretation for state estimation

2.5.2.1 Multiple-sensors as an information source

Over the last few years the applications and functionalities of robotic systems increased greatly. This inspired a new trend in robotics, namely intelligent robots. According to [30], the foundation of intelligent robots is sensor technology. This is due to the fact that an intelligent robot makes use of sensory data to make informed decisions, to react and to interact.

Multiple-sensors are needed in order for a robot to gather all of the required information [30]. With new and developing sensor technology being light in weight, low in cost and much more efficient, the use of multiple-sensors has become very common in applications. In order to take full advantage of the information that sensors provide, the data has to be inferred. Therefore, they should be interpreted as a sensory system. If the information gathered from the sensors is interpreted separately, inter relationships are lost. These relationships can provide a control system with much more useful information.

A combination of sensors can be categorised as either homogeneous or inhomogeneous, according to the information that they provide. *Homogeneous* sensors are sensors that acquire the same or a comparable physical measurement. These sensors are usually used together to improve the accuracy of a specific measurement. *Inhomogeneous* sensors capture different characteristics and their information has to be pre-processed since it isn't directly inferable [40]. These sensors are usually used together to provide estimates of measurements that are not directly represented by them separately. For example, depth information together with colour information can be used for easier feature extraction or object classification [41]. The process of multisensor data fusion is applied in state estimation of a robot in order to use sensor data optimally.

2.5.2.2 Multisensor data fusion

The process of fusing data from sensors is a wide ranging subject and throughout literature many different terminologies have been used interchangeably to describe it. Examples of these different terminologies include sensor fusion, information fusion, data fusion, multisensory data fusion and multiple-sensor fusion [42]. Just as the terminologies differ, there are many different definitions for multisensor data fusion. According to [43], sensor fusion is a method of integrating signals from multiple sources. A similar definition is given by [42], where it is seen as a technology that enables the combination of information gathered from several sources to produce a *"unified picture".* A review done by [44] discusses many different data fusion definitions. They conclude by proposing the following definition for information fusion; *"Information fusion is the study of efficient methods for automatically or semi-automatically transforming information from different sources and different points in time into a representation that provides effective support for human or automated decision making."*

The main motivation for multi-sensor data fusion is described by [40] *as the improvement in the usability and quality of the measurement result.* This includes advantages such as better resolution, improved noise suppression, increased robustness and improved accuracy. For the control of a robotic system, this means more accurate state estimation resulting in better control of the robot. The fusion of data from multiple-sensors are studied in numerous fields including signal processing, artificial intelligence, control theory, mathematical statistics, information theory as well as bionics [30], [42].

Multisensor data fusion systems can be classified according to their sensor configuration as competitive, complementary and cooperative integration [40]. *Competitive integration* is when each sensor in a sensor configuration delivers an independent measurement of the same property. Competitive integration is used to avoid erroneous measurements and to reduce uncertainty in measurements. *Complementary integration* is when the sensors in a sensor configuration do not measure the same quantity. The sensors can be integrated to provide a more complete image of the phenomenon under observation and therefore is seen as a solution for incompleteness.

Cooperative integration is when inhomogeneous sensors in a sensor configuration are integrated to obtain information that wouldn't be available from the sensors individually. Cooperative integration eliminates ambiguities and provides increased information of object details. All of these methods are usually included to some extent in state estimation. Fig. 2.4 provides a visual explanation of these classifications as methods of data acquisition. Here, coordinate-transformation describes the process where each sensor's local frame has to be transformed into a common frame so that fusion can occur.

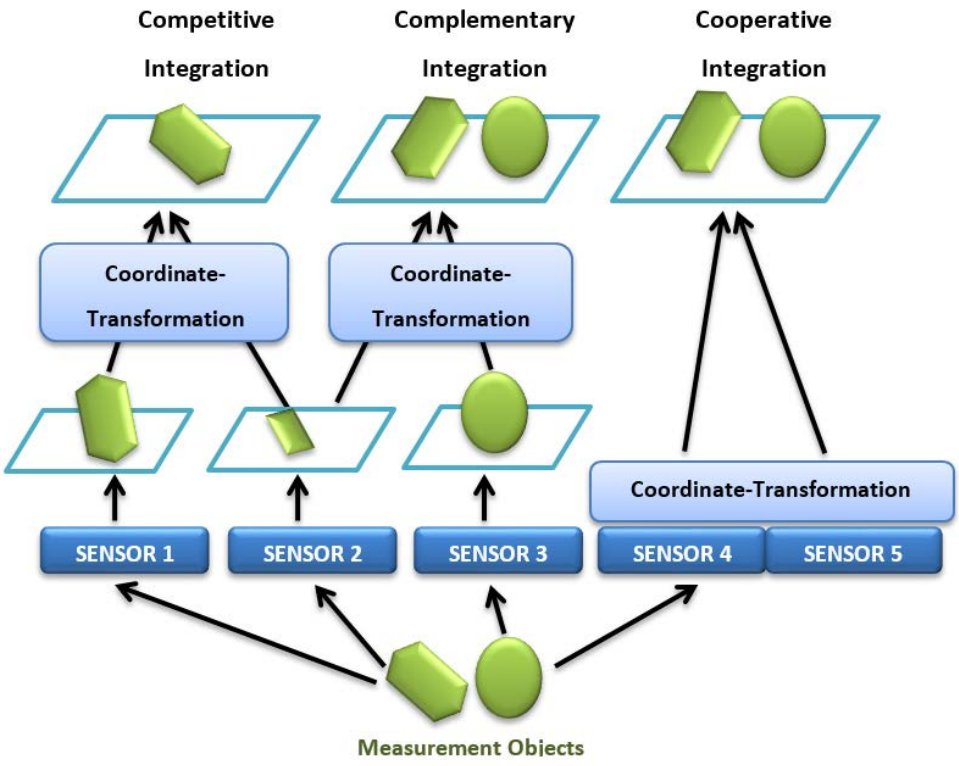

Figure 2. 4: Methods for data acquisition [40].

Multi-sensor data fusion challenges

There are numerous challenges that make data fusion for a sensory system such a complicated task. Most of these challenges are caused by the specific data that needs to be fused, their imperfections and the diversity of sensor technology found in the system [42]. According to Khaleghi et al. [42] the data fusion methodologies can be categorised based on the challenges that they address. Fig. 2.5 shows the main challenges involved with multiple-sensor data fusion.

From Fig. 2.5 it can be seen that there are four main challenging problems involved with the fusion of multiple-sensors: data imperfections, data correlation, inconsistencies found in data and disparateness. *Data imperfections* describe the level of impreciseness and the uncertainties found in sensor data. *Data correlation* is found when the same noise (external) influence the sensors being fused. This may cause over/under confidence in the fusion algorithm. *Data inconsistencies* are data that may resemble errors but are actually correct due to inconsistencies present in the environment. *Disparate data* describes a system that used a wide variety of different data sources (different sensors) to build a global view.

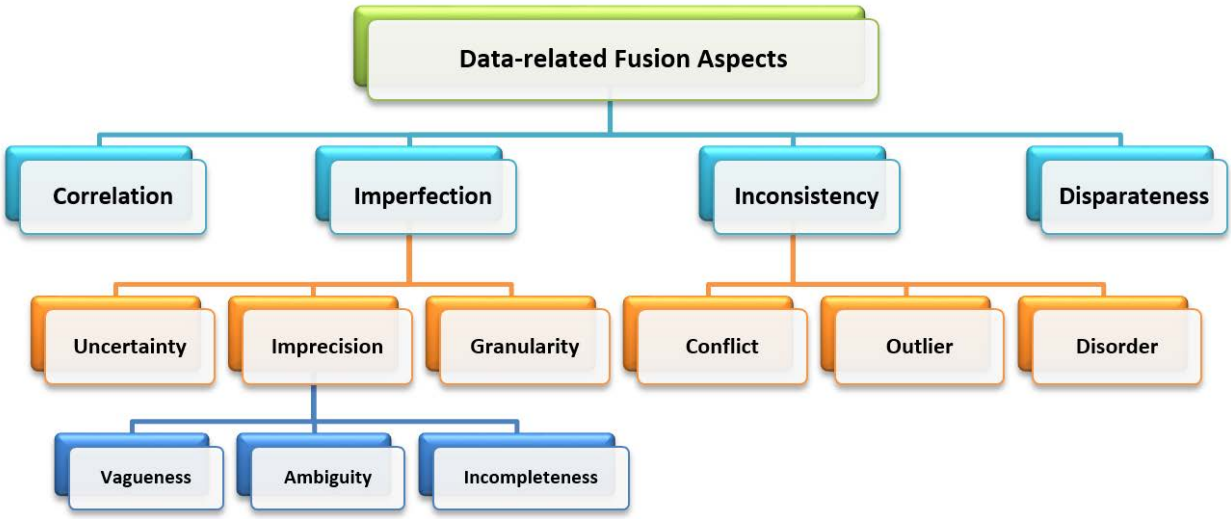

Figure 2. 5: Taxonomy of data fusion methodologies [42].

Multisensor Data Fusion Algorithms

Research done by Sasiadek [43] divides the sensor fusion algorithms into three basic categories. The first is based on least-squares techniques, the second on probabilistic models and the third is known as intelligent fusion. The *least-squares techniques* utilise optimisation theory, uncertainty ellipsoids, regularization and Kalman filtering. The *probabilistic model methods* are robust statistics, evidence theory, recursive operators and Bayesian reasoning. The *intelligent fusion* involves fuzzy logic, genetic algorithms and neural networks [43].

The review done by Khaleghi et al. [42], explores data fusion algorithms according to a novel taxonomy that is based on data-related aspects of fusion. Khaleghi et al. [42] specifically look at the data-related challenges that are solved with algorithms and provides tables that summarise the different algorithms, methods and solutions and their characteristics. In robotic systems these algorithms are used in state estimation approaches to estimate certain variables while filtering out errors and noise in sensors. Some of the most common state estimation algorithms will be discussed in Chapter 3.

2.6 Conclusion

The literature survey conducted provides a thorough background with regard to the focus of this study. Important terminology and concepts were introduced and discussed. Hexapod robots were identified as an important research topic due to of their ability to navigate in unstructured environments and their advantages over wheeled and other legged robots. The complicated control algorithms needed by a hexapod robot were identified as the main limitation in hexapod research.

However, literature showed that this limitation is further restricted by the time and resources needed to develop a platform and provide reliable state estimation of the robot. The importance of a sensory system, specifically a proprioceptive sensory system was identified for state estimation and stability control of a legged robot.

In order to address these limitations, this study will focus on implementing a state estimation approach on a commercially available hexapod platform. This will require a literature study on the mechanical characteristics of hexapod platforms in order to perform an analysis on the commercially available platforms. Further, the study will require the development of a proprioceptive sensory system for a specific platform. An in-depth literature study on state estimation for legged robots will guide the sensory system development. It will also provide information on the different approaches and algorithms that can be implemented to compute the state estimation for the hexapod platform.

Due to the deep theoretical background needed in order to derive a state estimation algorithm for a robot and the amount of time needed for the implementation and testing of the state estimation algorithm, the state estimation of the robot is the main focus of this study. In the following chapter a commercial hexapod platform will be chosen, specific proprioceptive sensors needed will be selected and a suitable state estimation approach will be identified.

Chapter 3: Literature study

"Part of the inhumanity of the computer is that, once it is competently programmed and working smoothly, it is completely honest."

~ Isaac Asimov

3.1 Introduction

Chapter 3 contains a literature study on specific topics identified in the literature survey chapter. From a literature study on hexapod platforms the best commercially available platform was selected. Common state estimation algorithms was discussed followed by an in-depth literature study regarding state estimation for specifically legged robots. A state estimation framework was also identified for this study. Lastly, the specific proprioceptive information needed by a legged robot was summarised and used to draw up the sensor requirements for the development of the sensory system.

3.2 Background

From the literature presented in Chapter 2, it was found that the main reason for the development of walking robots is to take advantage of their ability to navigate over unstructured terrain. But, the task of developing a legged robot for that purpose has been identified as very complex. Every design aspect, from the mechanical and electronic hardware up to the software and control system is time consuming and needs intricate integration.

The need for a hexapod platform with accurate state estimation using a proprioceptive sensory system was identified. Based on the need for research on hexapod control algorithms, a decision to use commercially of the shelf products for this study was made. This will equip other researchers with a fast and reliable solution to a platform on which control algorithms can be tested and implemented.

The following literature study focusses specifically on all the aspects and knowledge that is needed in order to do the state estimation for a hexapod robot with a proprioceptive sensory system. Literature is reviewed regarding hexapod platforms, proprioceptive sensory systems and current state of the art state estimation. This literature serves as the basis for all the design decisions that were made in order

to complete this study. The mechanical platform, the specific sensors and the state estimation processes will play a vital role in this study.

3.3 Hexapod platforms

In chapter 2 it was identified that the mechanical design of a hexapod robot directly influences some features of the robot. This will in turn influence the electronic design and thus the sensory system development. The hexapod platform's kinematics will also influence the state estimation and the control of the robot. It is therefore important to look at specific properties in the mechanical design of hexapods in order to make an informed decision when acquiring a platform for this study.

3.3.1 Mechanical characteristics of hexapod robots

A hexapod robot's mechanical design mainly consists of two major components namely: the legs and the body or trunk. Observations from literature that will influence this study are now discussed for both of these components.

3.3.1.1 Leg design

For legged robots there are two biologically inspired leg configurations. The first resembles those of animals (leg swing around a horizontal axis) whereas the second resembles those of insects (leg swing around a vertical axis). For hexapod robots it is found that the insect leg configuration is used more commonly. This is mainly due to the fact that the insect leg configuration provides better static and dynamic stability compared to the animal leg configuration [45].

The leg of the stick insect consists of four segments namely: coxa, femur, tibia and the foot (or tarsus). This results in each leg having four degrees of freedom (DOF). It is found that throughout literature the foot segment of the leg is neglected in robot design [10], [20], [46]. The main reason for this is simplification. By eliminating the feet, the number of joints in a hexapod robot reduces from 24 to 18. This not only decreases the robot's cost and weight but also simplifies the control and saves energy. A comparison between an insect leg (with a foot) and a robot designed leg (without a segment representing the foot) can be seen in Fig. 3.1.

Manoiu-Olaru et al. [45] states that for a legged robot, a successful design mostly depends on the design of the legs. This is motivated by considering that all aspects of walking by a legged robot are eventually governed by the limitations of the leg. When evaluating possible hexapod platforms, it is therefore important to look at leg designs that will impose the least constrains on the walking and

allow a maximum range of motion. The legs should further be as light as possible to provide a high payload/weight ratio [8].

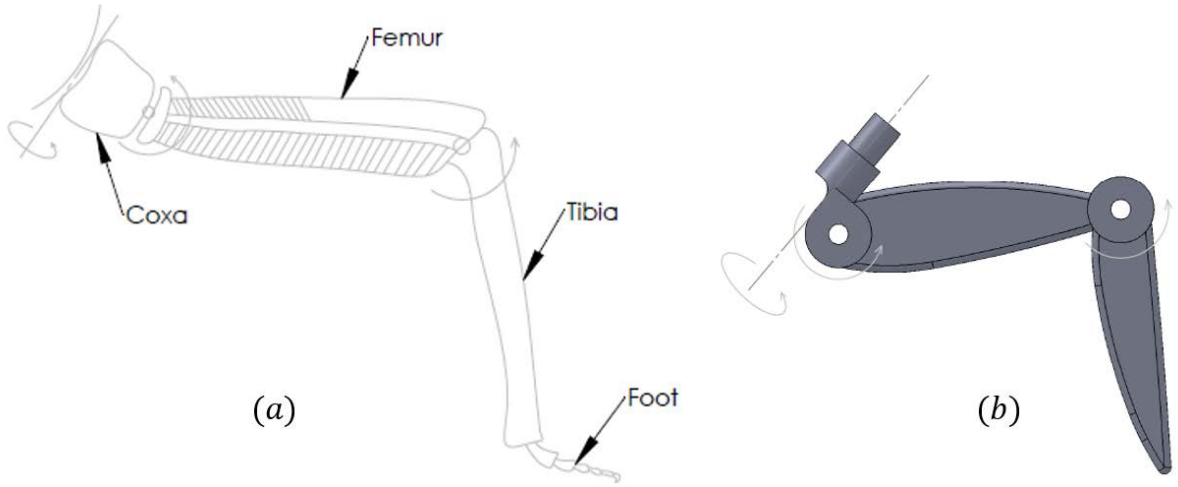

Figure 3. 1: Comparison between an insect (a) and a designed robot leg (b) [47].

3.3.1.2 Body design

As discussed in Chapter 2, a hexapods' body design is typically either based on a rectangular architecture or a hexagonal architecture. Although there are several studies that are based on the hexagonal architecture [9], [10], [21], the rectangular design is more common [8], [13], [15], [20], [48]. Preumont et al. [49] stated that while the hexagonal design, in contrary to the rectangular design, do not require a special gait in order to change walking direction, its control is more difficult. This is due to the legs that have different trajectories with respect to the body. Thus, the rectangular architecture has advantages regarding straight forward gait whereas the hexagonal architecture has advantages in turning gait [49], [50].

Research done by de Santos et al [8], [15] showed that the rectangular configuration can be optimised by broadening the section of the trunk where the middle legs are mounted. Last mentioned can result in a reduction in the energy consumed by the robot and contributes to the robot's stability. The influence of this research is made visible when looking at the trunk design of the Messor robot [20]. A trunk design similar to the trunk of Messor can be seen in Fig. 3.2.

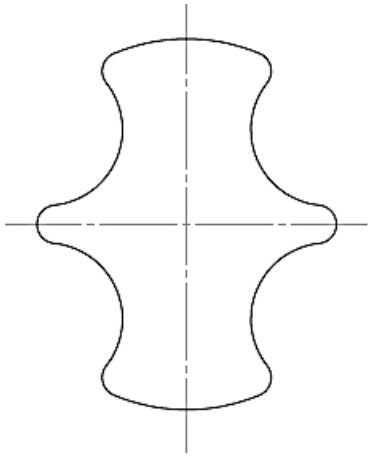

Figure 3. 2: Top view of trunk of the a typical hexapod robot [20]

A bio-inspired design where the body consists of three segments resembling insects such as the ant, has also been studied [12], [47]. This type of design has increased mobility as the body movement can contribute to stability control of the robot and the overcoming of obstacles. However, the extra weight is a disadvantage and the extra segments result in more complicated control algorithms. An example of such a design is shown in Fig. 3.3.

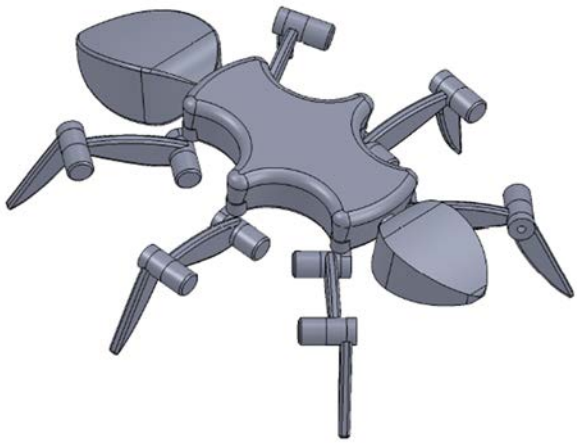

Figure 3. 3: Three segment body design.

3.3.2 Commercially available platforms

In this study the state estimation will be performed on a commercially available platform. The next section discusses the different low-cost (hobby classified) commercially available platforms from which one will be chosen for this study.

3.3.2.1 PhantomX AX Hexapod Mark II

The PhantomX AX Mark II hexapod robot is developed by Interbotix Labs and distributed by Trossen Robotics. All information about the PhantomX Mark II was found on the Trossen Robotics website [51]. The platform can be ordered containing either the standard Dynamixel AX-12A servos ($1199.95) or the faster, stronger Dynamixel AX-18A servos ($1949.95). The platform is also available without any servos ($549.95) or as a barebones kit ($269.99). Other than the servos, the platform kit comes with an Arduino-compatible ArbotiX Robocontroller, ArbotiX commander, two Xbee $1\ \mathrm{mW}$ modules, $11.1\ \mathrm{V}$ $2200\ \mathrm{mAh}$ LiPo battery, battery charger, USB Xbee interface and a USB A to Mini-B cable.

The PhantomX Mark II is made from Plexiglas with a rectangular body design (extended middle) and three DOF legs. On the Trossen Robotics website it is stated that the platform's hardware and software is open-source and suitable for hobbyists, education and research. The mechanical structure of the robot allows the adding of sensors and other electronic components. The possible servos that can be integrated onto the platform are restricted due to the mechanical design. These servos are however of good quality and have the advantage of providing feedback on position, temperature, voltage, speed and torque. The recommended payload for the robot is $2\ \mathrm{kg}$, but it can handle up to $4\ \mathrm{kg}$ with either of the provided Dynamixel servos. Photos of the PhantomX Mark II provided by Trossen Robotics can be seen in Fig. 3.4.

Figure 3. 4: PhantomX Mark II [51]

3.3.2.2 T-Hex (18 servo walker)

The T-Hex hexapod robot kit is manufactured by Lynxmotion and distributed by RobotShop. All information about the T-Hex hexapod robot can be found on the RobotShop website [52]. The robot kit is available with HS-645MG servos ($1032.97 without batteries) or a combination of HS-5685MH and HS-5990TG servos ($2130.01 without batteries). It has a rectangular design body with three DOF legs. A 24 servo configuration with a four DOF leg design is also available. The robot has a payload of $\pm 0.14\ \mathrm{kg}$. The robot kit includes a SSC-32, Bot Board II and a BASIC Atom Pro 28 for control and

processing and an Xbee/DIY RC stick radio control and TTL serial control for communication. It is however recommended by Lynxmotion to use a wireless PS2 controller. The structure of the platform is made of aluminium ServoErector Set brackets. The robot is compatible with a $6\,\mathrm{V}\ \mathrm{Ni-MH}\ 2800\,\mathrm{mAh}$ battery pack. Photos of the Lynxmotion T-Hex eighteen DOF Hexapod kit from the RobotShop website can be seen in Fig. 3.5.

Figure 3. 5: Lynxmotion T-Hex 18DOF hexapod walking robot kit [52].

3.3.2.3 DFRobot Hexapod Robot

The DFRobot Hexapod robot kit is manufactured and distributed by DFRobot for $\$990.00$ and disturbed by RobotShop for $\$890.00$. Information about the DFRobot Hexapod robot was found on the RobotShop website [53] as well as the DFRobot website [54]. The platform has a rectangular body design (extended middle) and a three DOF leg design. The platform is designed to use CDS5516 servos which have $14\,\mathrm{kg/cm}$ maximum holding torque. The servos also provide angle, torque and operating temperature feedback through a serial interface. The kit also includes an Arduino Mega 1280 microcontroller board and a Mega IO expansion shield, which allow the addition of sensors onto the platform. The robot needs to be powered by a $7.4\,\mathrm{V}$ battery. Photos of the DFRobot Hexapod robot kit can be seen in Fig. 3.6.

Figure 3. 6: DFRobot hexapod robot kit [53].

3.3.3 Platforms considerations

In order to compare commercial hexapod platforms the following topics have to be considered:

Open-source hardware and software: The ease in which the platform can be modified will have a big influence on this study. This will allow for more freedom in the sensory system design and development. It is also seen as an advantage in the sense that the platform can be used for further research and future work.

Payload: The payload of the robot refers to the amount of weight that can be added onto the platform without constraining its operational capabilities. It is mainly determined by the mechanical design and actuator strength. The payload capabilities of the platform will influence the electronic design of the sensory system as well as the stability margin of the robot. For this reason a higher payload capability is preferred as opposed to a lower payload capability.

Size: A small sized robot platform ($\pm$ 3 kg, fit in a $\pm$ 0.027 m^3 box) will be used for this study. This is determined by the size availability of commercial available platforms. A smaller sized platform is also more cost effective and practical for a research project.

Cost vs. quality: There exist a trade-off between the cost and the quality of a hexapod platform. The cost of the platform should not have an excessive influence on the platform choice. This will allow the development of a high quality, robust prototype.

Information: Available information such as the platforms' kinematics, detailed drawings or a model of the platform will contribute to the study by minimizing time and effort spent on unimportant tasks with regards to this study. Detailed drawings will also reduce measurement errors with regards to the development of the kinematic model for the robot.

Restrictions: Although most commercial hexapod platforms can be ordered without any electronic hardware, they are still designed to fit specific electronic components. This can influence the robot's capabilities by placing limitations on the electronic design. An example of such a limitation is when the space provided for an actuator in a leg reduces the possibilities in choice of servo motors that can be integrated onto the platform.

3.3.3.1 Hexapod platform trade-off study

Table 3.1 presents the trade-off study done between the commercially available hexapod platforms. A score out of ten is given for each platform consideration with regards to each of the platform options. The weight of each platform consideration was assigned using the information presented in

the platform considerations section. For all the platform options, the scores allocated to them are multiplied by the relevant weight and added up the produce a total score out of ten. Accordingly, the platform with the highest score will be the best option for this study.

Table 3. 1: Hexapod platform trade-off study

	Robot Platforms	**Platform Considerations**							
OPTIONS		Open-source hardware and software	Payload	Size	Cost	Quality	Information	Restrictions	**Total**
	PhantomX Mark II	8	8	9	5	8	4	3	6.85
	T-Hex (18 DOF)	6	2	6	5	8	3	3	5.2
	DFRobot Hexapod Robot	6	6	9	5	4	2	3	4.85
WEIGHT		0.25	0.15	0.05	0.1	0.25	0.1	0.1	

From the trade-off study in Table 3.1 it is clearly visible that the PhantomX Mark II has the highest total and will therefore be used for this study. The specific platform considerations that make the PhantomX Mark II the best platform is its open-source platform, high payload specifications and its quality design.

3.4 State estimation

This section discusses state estimation. Different algorithms for state estimation are considered followed with a detailed literature study on state estimation for legged robots. Proprioceptive state information needed for a legged robot is also summarised followed by a sensor requirement analysis used to specify the specific sensors that will be used in this study. The section ends with a discussion on the sensor considerations that need to be addressed when acquiring sensors for state estimation.

3.4.1 State estimation algorithms

3.4.1.1 Background

The processes of a robotic system can mathematically be modelled as state space models [55]. A state space model consists of a process or prediction model and a measurement model. The *prediction model* describes how the state of the process, $\boldsymbol{x}$, propagates in time based on external influences (inputs or noises). The *measurement model* describes how measurements, $\boldsymbol{y}$, are taken from the process. For the discrete time step k, a non-linear state space model usually consists of two non-linear functions, $\boldsymbol{f}$ and $\boldsymbol{h}$, such that

$$\boldsymbol{x}_{k+1} = \boldsymbol{f}(\boldsymbol{x}_k, \boldsymbol{u}_k, \boldsymbol{w}_k), \tag{3. 1}$$

$$\boldsymbol{y}_k = \boldsymbol{h}(\boldsymbol{x}_k, \boldsymbol{n}_k). \tag{3. 2}$$

In (3.1), $\boldsymbol{u}$, represents the process input vector, and $\boldsymbol{w}$, the state noise vector. In (3.2), $\boldsymbol{n}$, represents the measurement noise vector. The functions, $\boldsymbol{f}$ and $\boldsymbol{h}$, usually manage the dynamics of the process and the observations from the process, and are constructed from a set of discretized differential equations. Fig. 3.7 represents this general non-linear state space model.

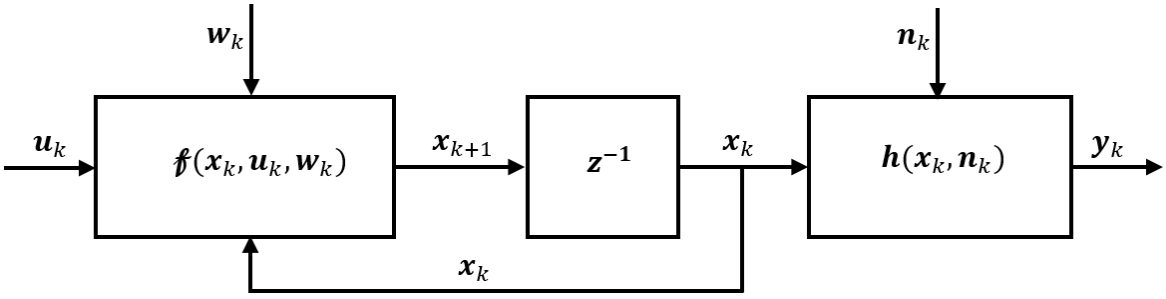

Figure 3. 7: A general non-linear state space model representation [55].

For the functions, $\boldsymbol{f}$ and $\boldsymbol{h}$, that are linear in state as well as input, a linear state-space model can be defined. Therefore, a linear state-space model is based on a linear process. The process can either be inherently linear or a non-linear process that has been linearised by means of a first-order Taylor approximation [55]. For a linear state-space model, the state propagation calculations are reduced to linear algebra by expressing the functions, $\boldsymbol{f}$ and $\boldsymbol{h}$, using matrices $\boldsymbol{F}$, $\boldsymbol{\mathcal{B}}$ and $\boldsymbol{H}$, such that

$$\boldsymbol{x}_{k+1} = \boldsymbol{F}_k \boldsymbol{x}_k + \boldsymbol{\mathcal{B}}_k \boldsymbol{u}_k + \boldsymbol{w}_k, \tag{3. 3}$$

$$\boldsymbol{y}_k = \boldsymbol{H}_k \boldsymbol{x}_k + \boldsymbol{n}_k, \tag{3. 4}$$

where, $\boldsymbol{F}$, is the process dynamics matrix, $\boldsymbol{\mathcal{B}}$, is the process input matrix, and $\boldsymbol{H}$, is the process observations or measurements matrix.

Fig. 3.8 represent a linear state-space model.

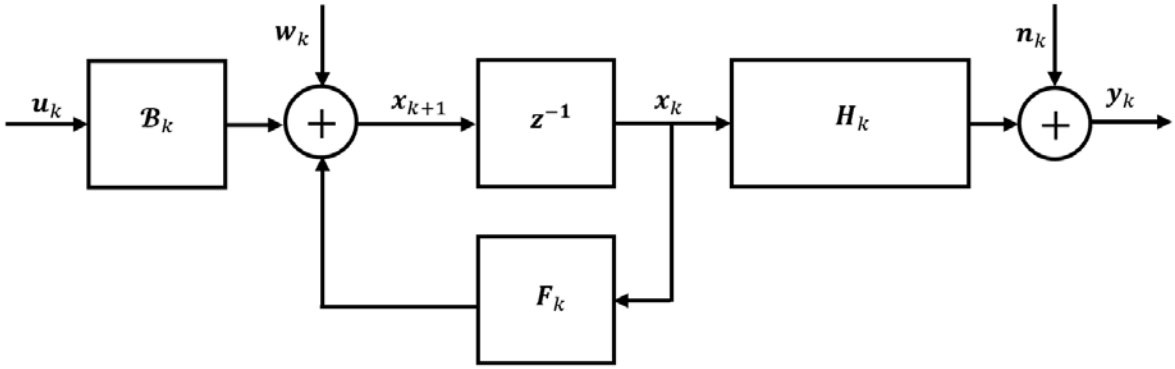

Figure 3. 8: A block diagram of a linear state space model [55].

With state estimation the state of a process that isn't directly observable can be estimated by using the current state to predict the next, and correcting the prediction by updating it with the noisy measurement data. This is done by estimating the probability density function (pdf) of the state of the process. Many different state estimation algorithms exist. Some of the most common algorithms will now be discussed.

3.4.1.2 Common state estimation algorithms

Recursive Bayesian estimation

Recursive Bayesian estimation is known as the most general form for state estimation and the optimal way of predicting the state pdf for any process [55], [56]. The recursive Bayesian estimator uses the estimate of the previous time step, $k-1$, together with new measurements to calculate the new estimate. This is done recursively for each time step in two steps, the prediction step, and the update step. By using the state propagation belief, $p(\boldsymbol{x}_k|\boldsymbol{x}_{k-1})$, computed from $\boldsymbol{f}$, the prediction step extrapolate the current state onto the next time step to predict the next state. The *a priori* pdf for the state, $\boldsymbol{x}_k$, at time step k, based on the measurements up to time step $k-1$, is calculated with the Chapman-Kolmogorov equation, such that [55]

$$p(\boldsymbol{x}_k|\boldsymbol{y}_{1:k-1}) = \int p(\boldsymbol{x}_k|\boldsymbol{x}_{k-1})p(\boldsymbol{x}_{k-1}|\boldsymbol{y}_{1:k-1})d\boldsymbol{x}_{k-1}. \quad (3.5)$$

The update step uses the measurement probability, $p(\boldsymbol{y}_k|\boldsymbol{x}_k)$, computed from $\boldsymbol{h}$, to correct the prediction by taking the new measurements into account [55]. This is done by using Bayes rule,

$$p(\boldsymbol{x}_k|\boldsymbol{y}_{1:k}) = \frac{p(\boldsymbol{y}_k|\boldsymbol{x}_k)p(\boldsymbol{x}_k|\boldsymbol{y}_{1:k-1})}{\int p(\boldsymbol{y}_k|\boldsymbol{x}_k)p(\boldsymbol{x}_k|\boldsymbol{y}_{1:k-1})d\boldsymbol{x}_k}. \quad (3.6)$$

Recursive Bayesian estimation does however not scale well for practical applications and is generally only considered as a theoretical foundation for state estimation.

Kalman filter

The Kalman filter is the most commonly used approach for state estimation. The Kalman filter reduces the well-known Bayesian estimation technique by introducing certain constraints on the process model. Only the mean and covariance of the probability distribution function of the state are calculated in an optimal way by minimizing the mean square error [57]. The Kalman filter requires the functions in the state model to be linear, with the noise terms uncorrelated, Gaussian and white with zero mean. By implementing these constraints, the state model can now be formulated as

$$\boldsymbol{x}_{k+1} = \boldsymbol{F}_k\boldsymbol{x}_k + \boldsymbol{\mathcal{B}}_k\boldsymbol{u}_k + \boldsymbol{w}_k, \quad (3.7)$$

$$\boldsymbol{y}_k = \boldsymbol{H}_k\boldsymbol{x}_k + \boldsymbol{n}_k, \quad (3.8)$$

with $\boldsymbol{F}, \boldsymbol{\mathcal{B}}$ and $\boldsymbol{H}$ matrices that replace $\boldsymbol{f}$ and $\boldsymbol{h}$.

The state estimation is then calculated in a two-step process: the prediction step and the update step. Fig. 3.9 demonstrates the Kalman filter loop where, for time step k, $\hat{\boldsymbol{x}}_k^-$ represents the *a priori* state estimate with covariance matrix, $\boldsymbol{\mathcal{P}}_k^-$, and $\hat{\boldsymbol{x}}_k^+$, represents the *a posteriori* state estimate with covariance matrix, $\boldsymbol{\mathcal{P}}_k^+$.

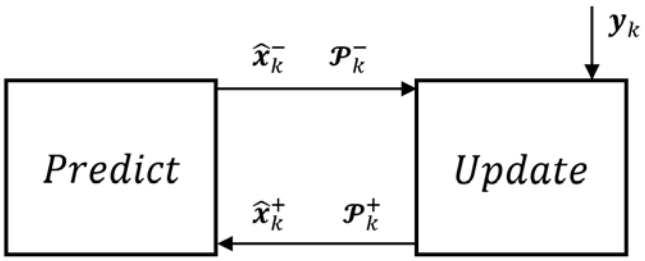

Figure 3. 9: Kalman filter loop [55].

While the Kalman filter is very easy to compute, it is only applicable to linear systems [58]. For non-linear systems the Extended Kalman filter, the Unscented Kalman filter and the Particle filter are the most commonly implemented state estimation approaches. Each of these approaches will now be discussed.

Extended Kalman filter

The need to apply the Kalman filter on non-linear systems, produced what is known as the Extended Kalman filter (EKF). The EKF linearise the system by calculating the Jacobian of $\boldsymbol{f}$ and $\boldsymbol{h}$ around the estimated state at each time step [3], [55]. This linearisation method makes use of the first-order Taylor expansions of the non-linear functions [3], [57]. Thereafter, the estimation is done by applying the normal Kalman filter equations.

If the consecutive linearisation do not represent a good approximation of the non-linear model, the algorithm diverges. Therefore, the linear approximation needed for the EKF can introduce errors in the estimated states and might not be appropriate for some systems [57]. This approach is however easy to implement and has low computational costs [3], making it one of the most common state estimators for non-linear systems.

Unscented Kalman filter

Another version of the Kalman filter that can be applied to non-linear systems is the Unscented Kalman filter (UKF). This approach propagates a set of points, called sigma points, through the non-linear functions. Where, the points are chosen in such a manner that their mean, covariance and higher order moments, represent the Gaussian random variable [55].

Since the UKF does not require derivatives, it resolves the limitations brought on by possible errors introduced in the EKF and is simple and easy to implement [57]. Another advantage observed by Orderud [55] is that non-Gaussian or non-additive noises can be accounted for since noise can be handled in a non-linear fashion. György et al. [57] state that the most computational intensive operation regarding the UKF approach is the calculation of the set of sigma points at each time step.

Particle filters

One of the limitations of the Kalman filters is the fact that they are constrained to model Gaussian probabilities. Orderud [55] state that they are therefore not capable of handling multimodal or skewed distributions. In order to estimate non-Gaussian distributions, one of the most common approaches is Particle filters.

The Particle filter approach can best be described as a recursive implementation of the Monte Carlo based statistical signal processing [57]. By using a set of randomly chosen weighted samples, the Particle filter approximates the Bayesian posterior probability density function. Here, each sample of the state is called a particle. Where, a large enough number of particles almost insures convergence of the true probability distribution function.

Although this approach addresses some of the limitations of Kalman filters, it is more computationally challenging. Since Particle filters are very computationally intensive, they are often intractable with regard to usage in real-time settings [55].

3.4.1.3 State estimation for a legged robot

Although state estimation is a broad research field with regards to wheeled robots, only a number of papers addresses it for legged robots. Also, in most of the research the walking of the legged robot is limited to structured and well-defined environments. Up to date, research presented for estimating the pose of a legged robot usually addresses the problem by using information from the environment outside and the robot itself. This information is provided by specific sensors and the fusion of those sensors.

However, as stated in Chapter 2, the robust state estimation for a legged robot should not rely on exteroceptive information and produce a full body pose estimation (6 DOF). With regard to legged robots, ultimately the robot needs to be fully autonomous and operate without having any knowledge of the terrain. This is especially evident with regard to small legged robots that can't carry heavy distance lasers to map the environment such as Ambler [59] and Dante II [60]. Also, the robot, and therefore the state estimation and control, should not be restricted to a specific gait pattern. The following literature was found regarding the state estimation of legged robots.

Gassmann et al. [61] stated that for unstructured terrain, legged robots need knowledge of their spatial position and their orientation. They based this statement on the observation that there is no complete *a priori* knowledge of the robot's operating environment conditions. They introduced a method that uses a Kalman filter to estimate absolute position and orientation information for a hexapod robot by using odometry calculations together with an IMU and a GPS. The odometry calculations were used to provide permanent basic relative measurements. The IMU was used to obtain information on the absolute spatial orientation. Although the method presented by Gassmann et al. [61] is able to provide the robot's global position, it makes use of a GPS (exteroceptive sensor) and is not able to handle non-statically stable gaits.

The pose estimation approach taken by Lin et al. [23] can handle non-statically stable gaits by fusing data from a IMU with a leg-strain-based model. The leg-strain-based model provides reliable position information while the robot has ground contact and isn't slipping, and the IMU provides continuous velocity information. Their approach accurately estimate body position and orientation for a hexapod robot but only when the robot has tripod ground support.

Chilian et al. [22] state that the pose estimation of a legged robot should be done by only using its own sensors, mainly consisting of proprioceptive sensors but also including visual sensors. Their presented approach, based on an indirect feedback information filter, fuses IMU data with 3D leg odometry measurements and relative 3D visual odometry measurements from a stereo camera, for the state estimation of a hexapod. For their state estimation they make no assumptions with regard the gait. However, their leg odometry measurements are only valid for three or more ground contact points and they use exteroceptive sensors.

The body pose information obtained by Messor [20], a hexapod robot is provided by a 6-DOF IMU consisting of three accelerometers and three gyroscopes. This inertial information is used to stabilize the platform as well as correct the heading while the robot is walking [20]. Walas and Belter [20] acquire the information as to when the robots feet is in contact with the ground, with two different methods. The first is simply with the use of a resistive force sensor that is mounted at the tip of each foot. At contact point the resistance of the sensor drop increasing the voltage that is measured by a microcontroller to obtain the force information. The second method uses current sensors attached to each motor in the legs of Messor. By fusing these two methods, they obtain more reliable information about the robot's feet contact with the ground. However, the use of force sensors in legged robot's feet can introduce errors with sensor failure caused by harsh environmental conditions.

Estremera et al. [62] identify that the detection of feet contact with the ground is essential for terrain adaption and that the monitoring of the feet forces is useful to enhance locomotion features. It enables the improvement of foot traction and the optimization of weight distribution. They designed virtual sensors based on neural networks in order to estimate forces exerted by the feet of a legged robot SILO4. *Virtual sensors* are methods used to obtain sensorial magnitudes with the indirect analysis of related available sensory data.

Their virtual sensors make use of data that is extracted from the robot's joint position sensors as input and were calibrated using force sensors placed on the robot's feet. By removing the need for physical force sensors on the feet during operation, this method eliminates the possibility of incomplete and erroneous information due to sensor failure. The use of virtual sensors in a legged robot can allow it

to operate in harsh conditions where the feet are constantly exposed to different terrain and obstacles. A method to estimate the global position of SILO4 in outdoor environments was developed by Cobano et al. [63]. The approach uses an EKF to combine a dead-reckoning estimation, using change in position, with Differential GPS measurements. However, the full six degrees of freedom body pose wasn't estimated and they make use of an exteroceptive sensor.

A particle filter was implemented by Chitta et al. [64] to globally localize the quadruped, LittleDog. The filter only used proprioceptive sensors. More specifically, joint encoders were used to get the leg kinematics and an IMU was implemented for inertial measurements. However, their approach requires knowledge about the robot's surroundings and assumes a statically-stable gait.

Reinstein and Hoffmann [37], [65] implemented an EKF that fuses data from an IMU and legged odometry (only proprioceptive sensors). The legged odometry uses a combination of joint-angle sensors and pressure sensors. The algorithm produces position, velocity and attitude estimation. The velocity is computed with the assumption of uninterrupted gait using a learned model. However, their approach limit its implementation on other platforms with its gait assumption as well as the model.

From all of the reviewed literature, the following approach was chosen to be implemented for this study:

Bloesch et al. [2] introduced a state estimation framework that allows the estimation of the full pose for the quadruped, starlETH. This is done without having to make any assumptions about the geometrical structure of the environment where the robot is located or its gait. The estimation is done with an Observability Constrained Extended Kalman filter (OCEKF) which fuses the data obtained from a kinematic model with on-board IMU measurements. Joint position sensors are used as input for the kinematic model which represent the relative pose measurement between the centre of the robot's body and the foot contacts. Therefore, the pose of the main body as well as the position of the footholds are estimated with only proprioceptive sensors.

Through an observability analysis performed, it is shown that all states other than absolute position and yaw can be estimated for one or more foot contacts. As the state estimation for this study is focussed on the stability control and not the global localization of the robot, neither absolute position or yaw is seen as extremely important. The specific approach can handle little foot slippage and uncertainties in the kinematics. Bloesch et al. [2] state that the key point to their filter design is the inclusion of the foot contact points. This enables a simple and consistent representation of the model equations. The estimation of the foot contact points can be used to build a map of where the robot is navigating. Therefore, it can be seen as a simultaneous localization and mapping algorithm.

From their test results, in comparison with other proprioceptive state estimation approaches, Bloesch et al. [2] state that the approach produced the highest level of precision published thus far. The formulation published is of a very generic form and allows the extension of the filter if other sensory measurements are needed. This is seen as a big advantage, not only with regard to this study but also for future work. The filter further allows its implementation on other kind of legged robots, which makes it applicable to this study. Rotella et al. [3] recently implemented a version of this state estimation framework on a humanoid robot simulated platform with positive results.

3.4.2 Proprioceptive state information for a legged robot

The main goal of a sensory system is to provide accurate and reliable sensory measurements for the state estimation of the robot. For the development of a legged robot, other than the complicated control algorithms that is needed, the complexity of the electronic and mechanical hardware is a very negative aspect. For this reason there exists a trade-off between accurate, robust information and hardware complexity when designing a sensory system for a hexapod robot. This trade-off has to be balanced by concentrating on the efficient use of sensors and sensory data for state estimation. It is therefore important to firstly identify the specific measurements that a proprioceptive sensory system has to provide for the state estimation of a hexapod.

From the proprioceptive information one should be able to recover the state of the robot itself [31]. This may include general information such as the battery level or temperature of the robot. More crucial proprioceptive information that is needed for robot control include the body position and orientation, velocities and accelerations, the angles of the legs and forces on the legs and at the feet.

As shown in Chapter 2, proprioceptive information for hexapod robots is typically gathered by sensors such as IMUs, joint position sensors and force sensors. By using multisensor data fusion techniques, ways have been found that reduces the number of physical sensors but still provide the accurate and reliable sensory information that is needed. By taking into consideration the state estimation techniques that can be used to obtain the required proprioceptive information, the specific types of sensors needed for this study can now be analysed.

3.4.3 Sensor requirements

The sensor requirements in terms of the information that they should supply can now be analysed. By doing a sensor requirement analysis one can determine the minimum amount of inhomogeneous sensors that needs to be implemented. From the literature discussed in Section 3.3.1.3, one can make the following observations:

- Fusing an IMU located on the body of the robot with the robot's kinematics (provided by joint position sensors in the actuators) can provide a full body state estimate.
- Force sensors placed on the tips of the feet of the robot can estimate forces acting on the feet and legs and provide information about the feet contact with the ground.
- The use of a virtual force sensor will eliminate the need for physical force sensors in the robot's feet.

These observations are visually shown in Table 3.2 where a sensor requirement analysis was done.

Table 3. 2: Sensor requirement analysis

		Requirements				
		Body pose	Leg pose	Feet force contact	**Full body pose (body, legs, feet)**	**Force estimate and contact information**
Sensors	IMU (accelerometers and gyroscopes)	✓				
	Joint position sensor		✓			
	Force sensor			✓		✓
Fused Sensors	IMU & Joint position	✓	✓		✓	
	Virtual force sensor (Based on full body estimate)			✓		✓

3.4.4 Sensor considerations for the proprioceptive sensory system

From the sensor requirement analysis it can be determined that the minimum amount of inhomogeneous sensors needed for the development of a proprioceptive sensory system, which can estimate the pose of the robot and the contact of the feet with the ground, are three. Although the proposed sensors should theoretically produce a viable sensory system, errors in sensor data will influence the sensory system information negatively. In this case, sensor fusion and filtering techniques, included in the state estimation, will have to be applied to the sensor data to ensure that accurate and reliable information is provided for control.

It is therefore necessary to investigate commercially available sensors that apply to this study in order to identify their advantages and more importantly, their disadvantages. The specification considerations related to the sensors should also be identified to ensure the optimal sensors are chosen to be integrated into the sensory system.

3.4.4.1 General considerations

The following specifications need to be considered in the designing phase of this study regarding the sensor choices:

- *Weight*: In order to ensure the robot still has a high payload capability after the electronic hardware for the sensory system has been integrated, the sensors should be as light as possible.
- *Size*: The size of the sensors should be of such nature that they can be integrated onto the platform with ease.
- *Power requirements*: The supply voltage and current needed by the sensors should be considered to avoid unnecessary power scaling or usage in the electronic design. The need for power scaling introduces more components and unnecessary power consumption.
- *Sensor models*: Specific sensor noises should be investigated to provide adequate sensors models to increase the accuracy of state estimation.

3.4.4.2 Joint position sensors

The PhantomX hexapod platform requires the use of the AX-12A or AX-18A Dynamixel servo actuators. These actuators provide position feedback with the use of a potentiometer. Resistive potentiometers have many advantages when used as position sensors. Resistive sensors are typically low in cost, commonly available and easy to implement. Drawbacks associated with potentiometers include: noticeable mechanical load, need to be physically connected to the object, subject to wear, and the friction and applied voltage causes heating of the potentiometer.

3.4.4.3 IMU

The development of low-cost (less than $3000) IMUs such as micro electro mechanical systems (MEMS), has increased their implementation in applications dramatically. MEMS also hold other advantages such as small physical size, light weight and low power usage. These advantages makes MEMS IMUs popular in robotic applications. Unfortunately, compared to the higher grade, expensive IMUs, they exhibit larger measurement errors like scale factor drifts, turn-on and in-run biases and noise [66], [67].

COTS IMUs that can be used for attitude estimation and navigation consists of accelerometers, which measure linear acceleration, and angular rate sensors (gyroscopes). These two types of sensors are used together to complement each other and provide more accurate estimates. The angular rate sensors are subject to drift errors caused by bias errors and they perform well in a high frequency range but are not accurate in a low frequency range. In contrast, the accelerometer sensors are not subject to drift and they perform well in a low frequency range but are not accurate in a high frequency range.

The errors produced by inertial sensors can be either deterministic (systematic) or random (dynamic). Bias and scale factor errors that remain constant and are caused by external factors, such as temperature, are deterministic. These errors are usually eliminated with the factory calibration done by the IMU developer. Because low-cost MEMS sensors have larger systematic errors compared to high cost IMUs, they need to be calibrated more frequently [67]. Most IMU distributers provide clients with the service of recalibrating their IMU sensors.

Random errors in inertial sensor data are caused by random noise in the sensor signals. Over time these random noise lead to drift in the bias or scale factor. Both a high frequency and low frequency component is found in random noise [67]. The high frequency component is characterized by white noise and is usually eliminated by a wavelet de-noising algorithm [68]. The low frequency component has correlated noise characteristics that causes slow drifting and scale factor errors. These errors are modelled by processes such as random walk or constant, Gaussian Markov and Auto Regressive models [67]. These processes usually involve the use of the noise autocorrelation or Allan variance function in order to obtain the first-order Gaussian Markov model [67].

Bloesch et al. [2] modelled the bias terms as Brownian motions where their derivatives can be represented by white Gaussian noise. They specify the noise terms by the corresponding covariance parameters that can be evaluated by examining the Allan variances. However, Bhatt et al. [67] state that traditional approaches (applied to high-cost IMUs) like the Gauss Markov model and Allan variance method is unsatisfactory for modelling random errors of MEMS sensors. Gebre-Egziabher [69] advises that care should be taken when applying the Allan variance method to low-cost inertial sensors. The Allan variance plots for low-cost sensors have correlated error slopes that are not necessarily equal to one of the standard error sources represented by the Allan variance slopes [69].

Noureldin et al. [36], [70] modelled MEMS errors with an artificial intelligence approach that utilizes Neural Networks. This approach proved to perform better than the conventional techniques but Bhatt et al. [67] state that it suffers from poor generalisation capabilities and that it deteriorates after a

short time. The approach is also limited for real-time implementations. As a solution to this, Bhatt et al. [67] proposes an enhanced Nu-Support Vector Regression technique in order to model the random MEMS sensor errors.

It is important to note that the quantities provided by the sensors do not directly provide the information that one might always want. For example, the angular rate needs to be integrated once to provide the attitude, and to determine position, the acceleration has to be integrated twice. This implies that an error in the acceleration measurement will cause a linear growing error in the velocity calculation and an exponentially growing error in the position calculation. The errors in measurements add up over time, which make the calculated values unusable [67]. For this reason Chao et al. [66] states that an IMUs' estimation accuracy heavily relays on the sensor fusion algorithm it uses.

In order to further minimize these errors it is important to consider IMUs that have aiding sensors included. Aiding sensors are sensors that can provide other independent estimates of the information that one needs from an IMU. The most common aiding sensors found in IMUs are a GPS and a magnetometer. Another type of sensor that is commonly found in IMUs is a temperature sensor. Temperature sensors are used in the factory calibration of the units to eliminate any errors in the data estimates that are caused by temperature differences.

The following has to be considered in order to evaluate and choose a suitable IMU for the hexapod sensory system:

- Internal sensors: The IMU needs at least a 3-axis accelerometer, a 3-axis gyroscope as well as a 3-axis magnetometer (as a proprioceptive aiding sensor).
- Output data: The IMU should provide acceleration, angular rate and magnetic field data. Other information such as the velocity, Euler angles, quaternion and rotation matrix will also be beneficial but can be calculated from the acceleration, angular rate and magnetic field data as needed for this study.
- Mechanical sensitivity: The IMU has to have low vibration and shock sensitivity in any direction to keep the noise in the sensor readings to a minimum.
- Axis misalignment: Axis misalignment is when the axes of sensor triads are not exactly orthogonal to each other. This should be as small as possible as it will cause cross-axis sensitivity errors.
- Scale factor: The scale factor is the ratio of the change in the output over the change in the intended input to be measured.

3.4.4.4 Force sensors

A wide range of different types of force sensors that work in different ways exists. In the robotics field, tactile force sensors are most commonly used in feet and finger tips to detect forces [71]. Tactile force sensors are force transducers that are very popular as they are very thin. The most common, low-cost tactile force sensors are force sensing resistors (FSR).

The following is suggested as desirable characteristics for tactile sensors [71]:

- The entire sensory area should be in contact when a force is applied (single-point contact). A sensor with a small sensory area is thus beneficial.
- The sensitivity range that is determined by the sensors' physical characteristics should be considered. The typical sensitivity range that will be appropriate for this study are for example 0-1 kg (0-10 N)
- The sensitivity due to the manner of application of the sensor should also be considered. This is for example a barrier between the sensors and the contact object.
- A sensor bandwidth of 100 Hz minimum.
- The hysteresis and drift parameters should be as low as possible to avoid errors in feedback.

3.5 Conclusion

From the literature study conducted, a trade-off study was completed between different commercially available hexapod platforms. As a result, the PhantomX Mark II hexapod robot kit was chosen to serve as a platform for this study. This platform has a high payload capability, provides joint-angle feedback and can easily be modified to include hardware such as sensors. For the state estimation of the robot, a kinematic model will have to be derived. However, no measurement information regarding the robot design is made available. This is seen as the main challenge presented with the use of the PhantomX Mark II platform. Measurements will have to be taken from the physical platform to compute a computer-aided model of the robot. The derivation of the platform's kinematic model will be discussed in Chapter 4.

Through an in-depth literature study that investigated state estimation approaches applied to legged robots, an EKF framework, presented by Bloesch et al. [2], was chosen to be implemented for the state estimation of the hexapod. Even though Bloesch et al. [2] only tested the filter on a quadruped, it is stated that their EKF can be implemented on various kinds of legged robots. The framework provides estimates regarding the position, velocity and quaternion of the centre of the robot body as well as

the positions of the robot's feet contact points. Bias estimations regarding the IMU measurements are also provided. The EKF presented not only provides all the information that is necessary for stability control of the robot, it can also be interpreted as a SLAM algorithm. The EKF also allows expansion by including further sensory measurements and can handle unknown environments and arbitrary locomotion gaits. The derivation of the EKF for the hexapod platform will be discussed in Chapter 6.

The chapter concludes by identifying specific types of proprioceptive sensors needed for the platform's sensory system. These sensor types were chosen in such a manner to implement the state estimation of the robot but also to allow future work on the platform and possible improvements to the state estimation. Specific requirements that need to be considered when acquiring the sensors for the sensory system were also discussed. The sensory devices chosen for this study as well as the derivation of their measurement models will be discussed in Chapter 5.

Chapter 4: Kinematic model

"The most important thing is to keep the most important thing the most important thing."

~ From 'Foundation design', by Coduto, Donald P.

4.1 Introduction

The methodology followed to derive the kinematic model of the hexapod robot platform will be discussed in this chapter. The kinematic model will specifically describe the forward kinematics of the robot. This means that given a set of joint angles, the solution of the kinematic model will give the position and orientation of the feet relative to a base frame on the body of the robot (body coordinate frame). Since all of the legs of the hexapod robot are physically the same, it is possible to simplify the derivation of the robot's kinematic model by first deriving the kinematic model for one leg. After modelling one leg of the hexapod, the entire robot can be modelled by transforming the leg kinematics into the body coordinate frame. Lastly, the kinematic measurement model is derived for the state estimation of the robot.

4.2 Background

In this section background is discussed regarding the descriptions and their operators used to specify attributes that will be needed to derive the kinematic model of the hexapod robot. The description of positions, orientations and frames will be considered along with their corresponding operators, namely translation, rotation and transformation. *Introduction to robotics: mechanics and control* was used for the theory of the kinematics [72].

4.2.1 Position

By establishing a coordinate system, the location of any point in space can be determined with a 3×1 position vector. Let the point, ${}^{A}\boldsymbol{P}$, be represented by a position vector located in coordinate system, $\{A\}$, and let the individual elements of the vector be represented by p_x, p_y and p_z such that

$$ {}^{A}\boldsymbol{P} = \begin{bmatrix} p_x \\ p_y \\ p_z \end{bmatrix}. \tag{4. 1} $$

Fig. 4.1 shows a coordinate system $\{A\}$ with three mutually orthogonal unit vectors, $\hat{\boldsymbol{X}}_A, \hat{\boldsymbol{Y}}_A$ and $\hat{\boldsymbol{Z}}_A$, and a point ${}^A\boldsymbol{P}$, representing a vector locating a position in space.

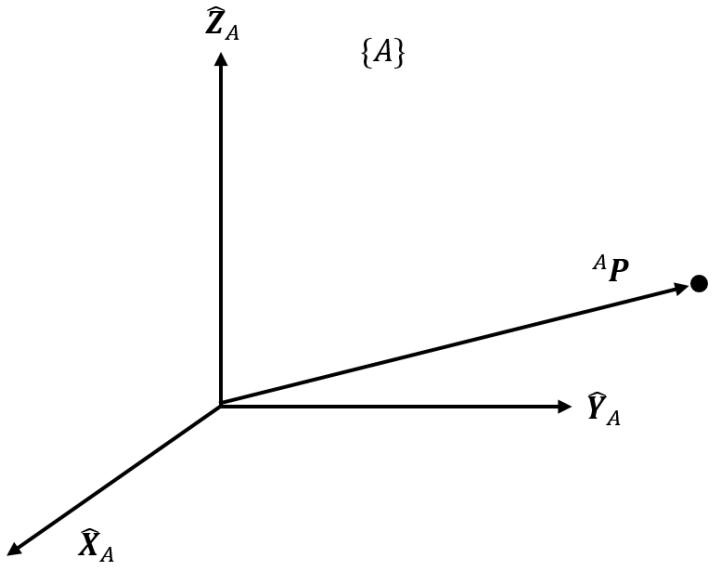

Figure 4. 1: Position vector relative to a coordinate frame.

Translation can be defined as an operator that moves a point, ${}^A\boldsymbol{P}_1$, a finite distance along a given vector direction provided by vector, ${}^A\boldsymbol{G}$. The result of the translation operator is a new point ${}^A\boldsymbol{P}_2$, shown in Fig. 4.2 and given by

$$ {}^A\boldsymbol{P}_2 = {}^A\boldsymbol{P}_1 + {}^A\boldsymbol{G}. \tag{4. 2}$$

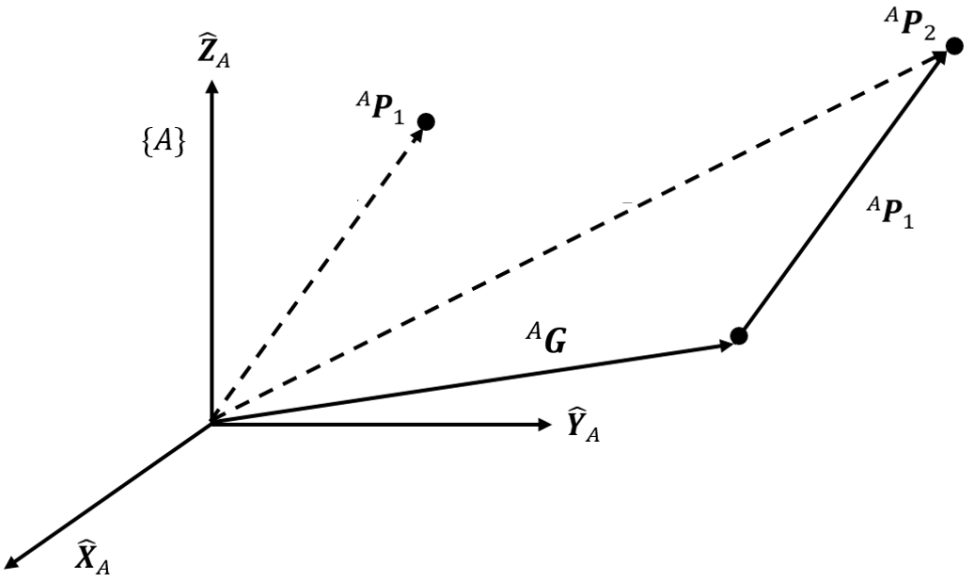

Figure 4. 2: Translation of a point.

4.2.2 Orientation

Let ${}^{A}\boldsymbol{P}$ be a point on a body in space. It is necessary to describe the orientation of the body in space as seen from a reference system. By attaching a coordinate system $\{B\}$ onto the body, a description of the orientation of the body relative to a reference coordinate system $\{A\}$ can be provided. This is done by writing the unit vectors of the three principal axes of $\{B\}$, $\hat{\boldsymbol{X}}_B$, $\hat{\boldsymbol{Y}}_B$ and $\hat{\boldsymbol{Z}}_B$, in terms of the reference coordinate system $\{A\}$. These vectors are written as ${}^{A}\hat{\boldsymbol{X}}_B$, ${}^{A}\hat{\boldsymbol{Y}}_B$ and ${}^{A}\hat{\boldsymbol{Z}}_B$. Let the rotation matrix ${}^{A}_{B}\boldsymbol{C}$ describe $\{B\}$ relative to $\{A\}$ such that

$$ {}^{A}_{B}\boldsymbol{C} = \begin{bmatrix} {}^{A}\hat{\boldsymbol{X}}_B & {}^{A}\hat{\boldsymbol{Y}}_B & {}^{A}\hat{\boldsymbol{Z}}_B \end{bmatrix} = \begin{bmatrix} \hat{\boldsymbol{X}}_B \cdot \hat{\boldsymbol{X}}_A & \hat{\boldsymbol{Y}}_B \cdot \hat{\boldsymbol{X}}_A & \hat{\boldsymbol{Z}}_B \cdot \hat{\boldsymbol{X}}_A \\ \hat{\boldsymbol{X}}_B \cdot \hat{\boldsymbol{Y}}_A & \hat{\boldsymbol{Y}}_B \cdot \hat{\boldsymbol{Y}}_A & \hat{\boldsymbol{Z}}_B \cdot \hat{\boldsymbol{Y}}_A \\ \hat{\boldsymbol{X}}_B \cdot \hat{\boldsymbol{Z}}_A & \hat{\boldsymbol{Y}}_B \cdot \hat{\boldsymbol{Z}}_A & \hat{\boldsymbol{Z}}_B \cdot \hat{\boldsymbol{Z}}_A \end{bmatrix}. \quad (4.3) $$

Fig. 4.3 shows the orientation of the point ${}^{A}\boldsymbol{P}$ on a body relative to a reference frame.

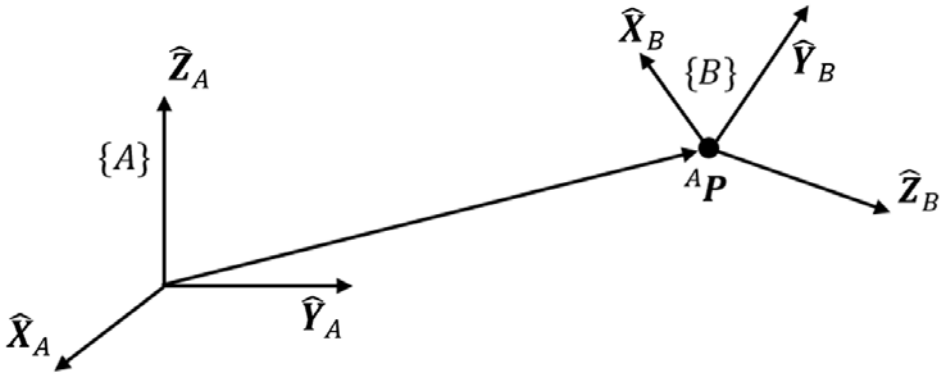

Figure 4. 3: Location and orientation of a point relative to a reference system.

The rotation matrix can also be used as an operator $\boldsymbol{C}_{\boldsymbol{K}}(\theta)$ to rotate a point ${}^{A}\boldsymbol{P}_1$ about some axis direction $\hat{\boldsymbol{K}}$ by θ degrees. The result of the rotation operator is a new point ${}^{A}\boldsymbol{P}_2$, shown in Fig. 4.4 and given by

$$ {}^{A}\boldsymbol{P}_2 = \boldsymbol{C}_{\boldsymbol{K}}(\theta)\, {}^{A}\boldsymbol{P}_1. \quad (4.4) $$

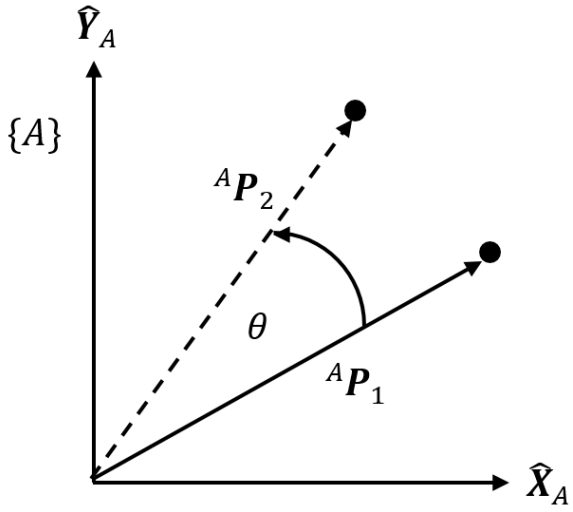

Figure 4. 4: Rotation of a point about the $\hat{Z}$ axis by θ degrees (${}^A\boldsymbol{P}_2 = \boldsymbol{C}_Z(\boldsymbol{\theta})\ {}^A\boldsymbol{P}_1$).

4.2.3 Frames

A robot can physically be described as a system of rigid bodies that are connected with joints. For each rigid body, its orientation together with its position in space is defined as its *pose* [31]. In order to determine the pose of a rigid body in space, we define an entity called a *frame* as a set of four vectors consisting of orientation and position [72]. A frame is therefore a coordinate system that gives the orientation as well as the position vector that locates the frame's origin relative to some other frame.

With regard to this study, a *right-handed frame* is defined as a frame with a three dimensional coordinate system in which the axes satisfy the *right-hand rule*. The *right-hand rule* is described as follows. For the right hand, with the thumb and index finger (first finger) stretched out, the second finger bend in to form a $90°$ angle relative to the index finger, and the third and fourth fingers curled in towards the palm, the *right-hand rule* states that:

- The orientation of the thumb define the positive Z-axis, the orientation of the index finger define the positive X-axis, and the orientation of the second finger define the positive Y-axis.
- The curl direction of the third and fourth finger indicate the positive rotation along the Z-axis and define that the positive rotation along any of the axes are anti-clockwise.

Fig. 4.5 shows the right-hand rule.

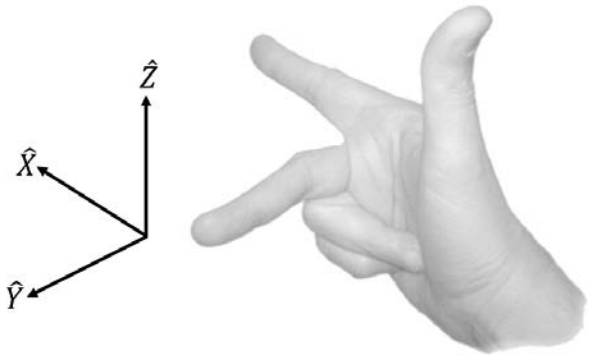

Figure 4. 5: Right-hand rule.

For this study, the symbol $\boldsymbol{B}$ is defined to represent the body coordinate frame (on the robot) and the symbol $\boldsymbol{I}$ is defined to represent the inertial coordinate frame (non-accelerating reference in space). The relationship between the body coordinate frame $\boldsymbol{B}$ and the inertial coordinate frame $\boldsymbol{I}$ can be described by the rotation matrix ${}^{I}_{B}\boldsymbol{C}$ and the position vector, ${}^{I}\boldsymbol{P}_{BORG}$, locating the *origin* of frame $\boldsymbol{B}$ relative to frame $\boldsymbol{I}$.

$$\boldsymbol{B} = \{{}^{I}_{B}\boldsymbol{C}, {}^{I}\boldsymbol{P}_{BORG}\}. \tag{4. 5}$$

Related to the descriptor frame, the matrix operator *transformation,* $\boldsymbol{T}$, can be defined. The transformation operator rotates and translates a vector ${}^{A}\boldsymbol{P}_{1}$. The result of the transformation operator is a new vector ${}^{A}\boldsymbol{P}_{2}$, given by

$${}^{A}\boldsymbol{P}_{2} = \boldsymbol{T}{}^{A}\boldsymbol{P}_{1}. \tag{4. 6}$$

The transformation operator can also be used to rotate and translate a vector point ${}^{B}\boldsymbol{P}$ in frame $\{B\}$ into frame $\{I\}$, written as

$${}^{I}\boldsymbol{P} = {}^{I}_{B}\boldsymbol{T}{}^{B}\boldsymbol{P}. \tag{4. 7}$$

4.3 Robotic platform

The PhantomX® [51] hexapod robot platform is used as a base platform for this study. This specific platform is chosen based on the results of the trade-off study conducted in the literature study with regards to different commercially available hexapod platforms. Since the robot is only a prototype, no mechanical design was implemented with regard to the integration of the different components onto the platform. The extra components needed for this study were simply placed on the robot in an organized manner, distributing their weight equally throughout the robot body. This section is merely

provided as context to the reader with regard to the derivation of the kinematic model and the location of the sensors. Fig. 4.6 is a photo of the final robot prototype as used in this study.

Figure 4. 6: Robot prototype with integrated sensors.

The following components were integrated onto the PhantomX® robot platform:

- Six FlexiForce® A201 force sensors, one per foot [73].
- One MicroStrain 3DM-GX3®-25 IMU [74].
- One UDOO (single-board computer) [75].
- One Lithium Polymer battery.

An in-depth discussion on the specific integrated sensors can be found in Chapter 5. The internal coordinate frame of the IMU is used as the body coordinate frame for the robot in all calculations. The IMU is mounted on top of a 2 mm thick Perspex plate, with the Z-axis of the IMU aligning with the middle of the robot body. Fig. 4.7 shows the location of the IMU on the robot as well as the location of the IMU's internal coordinate frame. The exact dimensions of the location of the origin of the internal coordinate frame inside the IMU can be found in its mounting diagram [76].

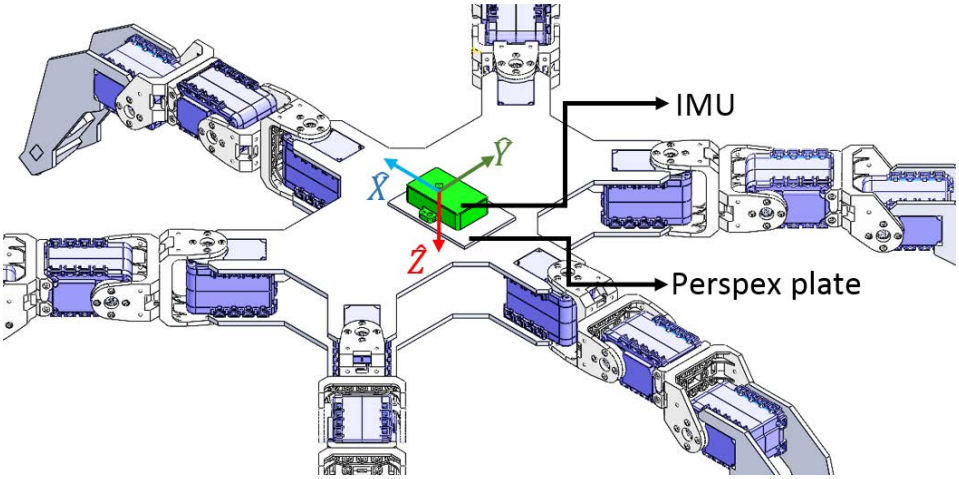

Figure 4. 7: Location of the IMU on the robot platform.

Each of the servo motors on the robot has been assigned with an ID. Fig. 4.8 shows a top view of the robot indicating the specific servo motors and their corresponding ID's for each leg. Throughout this study, this figure will be used as a reference to identify specific servo motors.

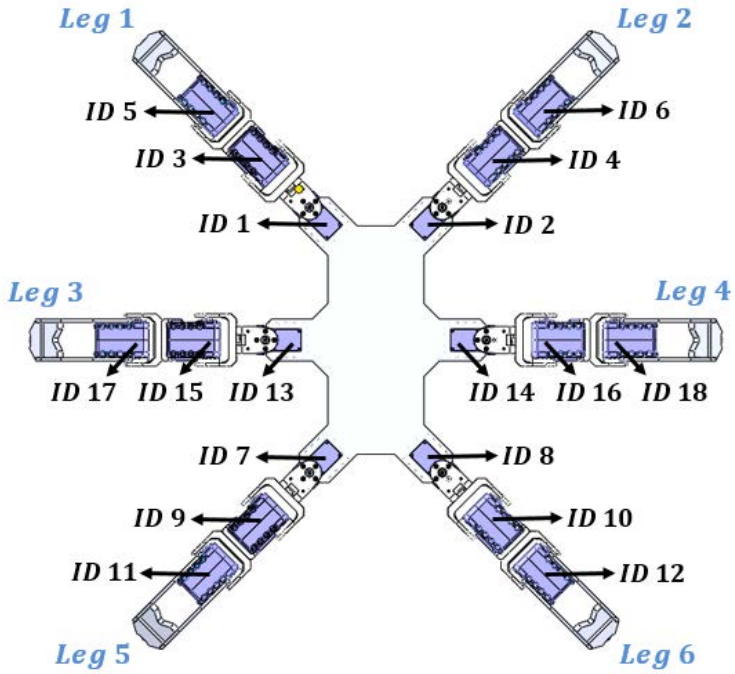

Figure 4. 8: Top view of robot with servo motor ID's.

4.4 Kinematic model for a robot leg

The PhantomX® hexapod robot has six legs. Each leg can be characterised by four rigid bodies, the base, coxa, femur and tibia. Each rigid body can mathematically be presented as a $link$. Servo motors

connect the neighbouring rigid bodies. Each servo motor is mathematically presented as a $revolute\ joint$ which exhibits only one degree of freedom. Fig. 4.9 shows a simple example of a revolute joint.

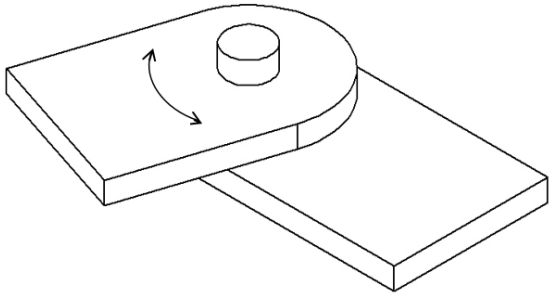

Figure 4. 9: Example of a revolute joint.

Fig.4.10 shows the link-connection description of the robot leg relative to the sectional view of the actual PhantomX® robot leg. The base is represented by $link\ 0$, the coxa is represented by $link\ 1$, the femur is represented by $link\ 2$ and the tibia is represented by $link\ 3$. The line in space created where $link\ i$ rotates relative to $link\ i-1$, is defined as joint $axis\ i$.

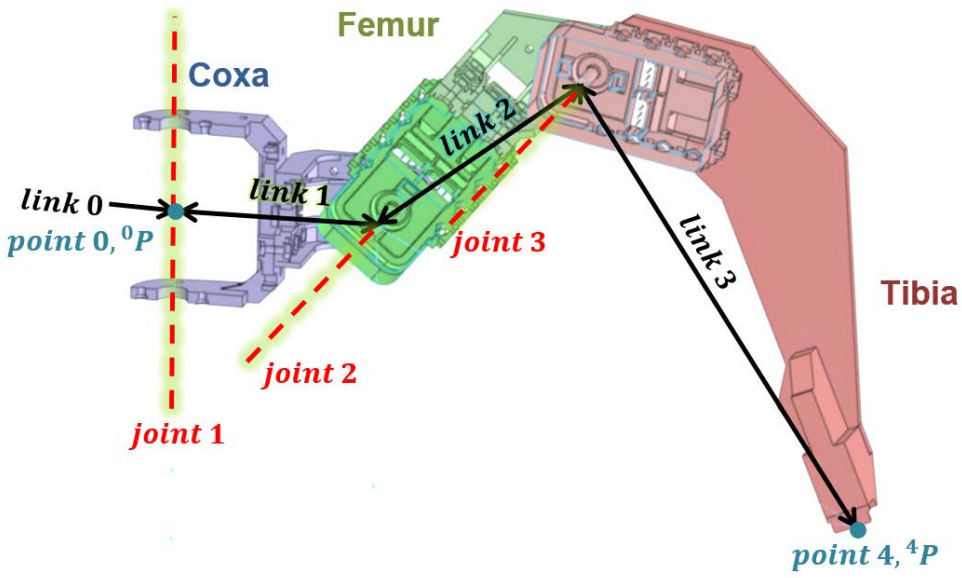

Figure 4. 10: The relationship between the sectional view of the robot leg and the links and joint axes.

It is important to notice that a link only represents the relationship between two neighbouring joint axes. Let ${}^{0}_{4}\boldsymbol{T}$ be the transformation needed to define the foot of the robot, ${}^{4}\boldsymbol{P}$ (point 4) relative to the base of the robot, ${}^{0}\boldsymbol{P}$ (point 0 or origin of the leg). Then ${}^{4}\boldsymbol{P}$ can be transformed into ${}^{0}\boldsymbol{P}$. The kinematic equation for the robot leg may then be given by

$$^{0}\boldsymbol{P} = {}^{0}_{4}\boldsymbol{T}\ {}^{4}\boldsymbol{P}. \tag{4. 8}$$

4.4.1 Derivation of link parameters and affixing frames to links

In order to derive the kinematic model for the robot leg, the Denavit-Hartenberg notation is used [72]. In order to describe the robot leg kinematically, four parameters, namely; link length, link twist, link offset and joint angle will now be defined and assigned to each link. The assignment of the link parameters is shown in Fig.4.11.

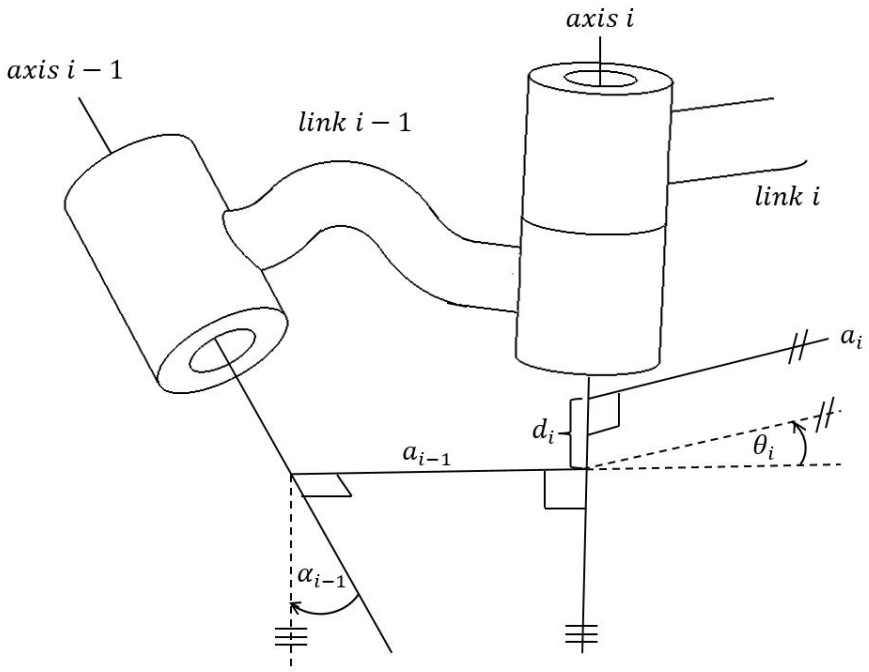

Figure 4. 11: Example of allocation of the four link parameters.

Let the $link\ length, a_{i-1}$ of $link\ i-1$ be defined as the length of a line that exists mutually perpendicular to both $axis\ i$ and $axis\ i-1$. The line that defines the link length will always exist and, except in the case where both axes are parallel, will always be unique. It is now possible to construct a plane with its normal, the line defining the link length. By projecting the $axis\ i-1$ and the $axis\ i$ onto this plane, the angle existing between them can be measured. Let the $link\ twist\ \alpha_{i-1}$ of $link\ i-1$, be defined as the angle measured about a_{i-1} from $axis\ i-1$ to $axis\ i$. This measurement should be done using the right-hand principle.

For any two $links\ i-1$ and i, that are connected, there exists a common joint $axis\ i$ between them. Let the $link\ offset\ d_i$, be defined as the signed distance between the intersection of a_{i-1} with the axis of $joint\ i$, and the intersection of a_i with the axis of $joint\ i$. Let the $angle\ \theta_i$, be defined as the angle measured about the common $joint\ axis\ i$, between the connected $links\ i-1$ and i. For a revolute joint, the joint angle is a variable.

The relationship between any two axes in space can be defined by only the link length and the link twist. The link offset and joint angle are used to specify how links are connected to each other. In order to define the location of neighbouring links relatively to each other, a frame will be attached to each link. The following convention is used to attach a frame to each link:

The number of a specific frame is in accordance with the link it is attached to. Therefore, $frame\ \{i-1\}$ is attached to $link\ i-1$, $frame\ \{i\}$ is attached to $link\ i$, and so on. The following method is used to locate frames on the links [72]:

- For $frame\ \{i\}$, the X-axis is called $\hat{X}_i$, the Y-axis is called $\hat{Y}_i$ and the Z-axis is called $\hat{Z}_i$.
- The origin O_i, of $frame\ \{i\}$ is located where the line defining the $link\ length\ a_i$ intersects the $joint\ i$ axis perpendicular.
- $\hat{Z}_i$ is coincident with $joint\ axis\ i$.
- $\hat{X}_i$ is located on a_i pointing from $joint\ i$ towards $joint\ i+1$. When $a_i = 0$, $\hat{X}_i$ is normal to the plane of both $\hat{Z}_i$ and $\hat{Z}_{i+1}$.
- α_i is measured about $\hat{X}_i$ according to the right-hand principle.
- The $frame\ \{i\}$ is completed by forming $\hat{Y}_i$ with the right-hand rule.

Fig.4.12 shows the parameter and link-frame assignments for the robot leg. $Frame\ \{0\}$ is attached to the base of the robot leg (body of the robot or $link\ 0$). $Frame\ \{0\}$ never moves and can therefore be seen as the reference frame. $Frame\ \{0\}$ is also chosen to coincide with $frame\ \{1\}$ with $\hat{Z}_0$ along $axis\ 1$. This results in $a_0 = 0$, $\alpha_0 = 0$ and $d_1 = 0$, since $joint\ 1$ is revolute. For $frame\ \{4\}$, $\hat{X}_4$ is chosen to align with $\hat{X}_3$ so that $\theta_4 = 0$. The origin O_4, of $frame\ \{4\}$ is chosen where $d_4 = 0$.

Table 4.1 provides a summary of the link parameter values of the PhantomX® hexapod robot leg:

Table 4. 1: Link Parameter Values.

i	α_{i-1} [°]	a_{i-1} [m]	d_i [m]	θ_i [°]
1	0	0	0	θ_1
2	90	0.0520	0	θ_2
3	0	0.0662	0	θ_3
4	0	0.1389	0	0

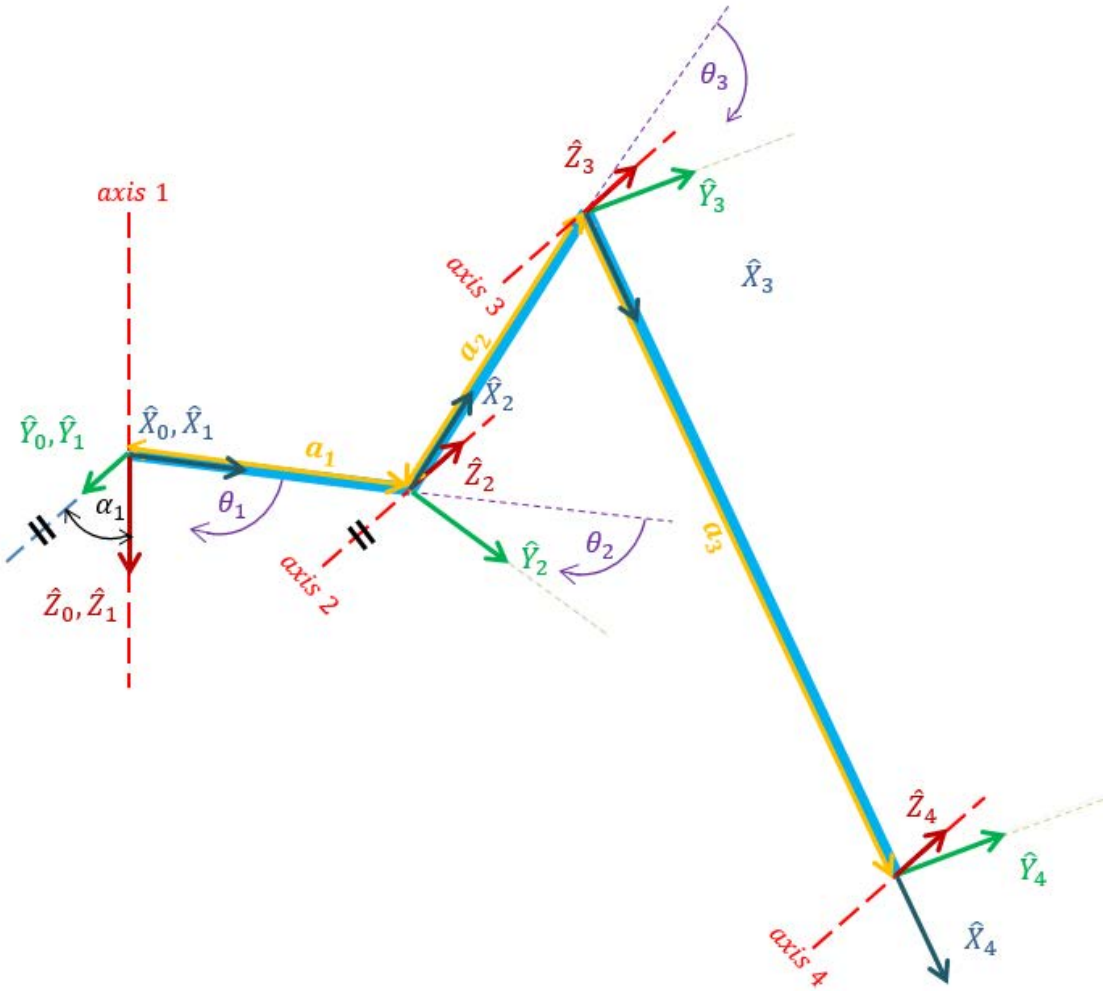

Figure 4. 12: Parameter and link-frame assignment from the robot Leg.

4.4.2 Derivation of the link transformations

With the implementation of a frame for each link, we have divided the kinematic problem into four subproblems. These subproblems represent the transformations between the neighbouring frames, namely ${}^{0}_{1}\boldsymbol{T}$, ${}^{1}_{2}\boldsymbol{T}$, ${}^{2}_{3}\boldsymbol{T}$ and ${}^{3}_{4}\boldsymbol{T}$. By using the four link parameters defined, one can further divide each subproblem into four. This can be used to derive a general transformation that describes the relationships between neighbouring frames:

Let ${}^{i-1}_{i}\boldsymbol{T}$ represent the transformation that defines $frame\,\{i\}$ relative to $frame\,\{i-1\}$. This transformation will always be a function of the four link parameters defined with one of them being a variable and the other three fixed in value. The transformation that transform ${}^{i}\boldsymbol{P}$, a point defined in $frame\,\{i\}$ to ${}^{i-1}\boldsymbol{P}$, the same point described in $frame\,\{i-1\}$ can be represented as

$$\begin{bmatrix} {}^{i-1}\boldsymbol{P} \\ 1 \end{bmatrix} = {}^{i-1}_{i}\boldsymbol{T} \begin{bmatrix} {}^{i}\boldsymbol{P} \\ 1 \end{bmatrix}. \quad (4.9)$$

In order to include the four parameters, one can define three intermediate frames for each link, $\{J\}$, $\{K\}$ and $\{L\}$. Let $frame\ \{J\}$ differ from $frame\ \{i-1\}$ by a rotation representing the $link\ twist\ \alpha_{i-1}$. Let $frame\ \{K\}$ differ from $frame\ \{J\}$ by a translation representing the $link\ length\ a_{i-1}$. Let $frame\ \{L\}$ differ from $frame\ \{K\}$ by a rotation representing the $joint\ angle\ \theta_i$. Lastly, let $frame\ \{i\}$ differ from $frame\ \{L\}$ by a translation representing the $link\ offset\ d_i$. Fig. 4.13 shows an example of the intermediate frames between $frame\ \{i-1\}$ and $me\ \{i\}$.

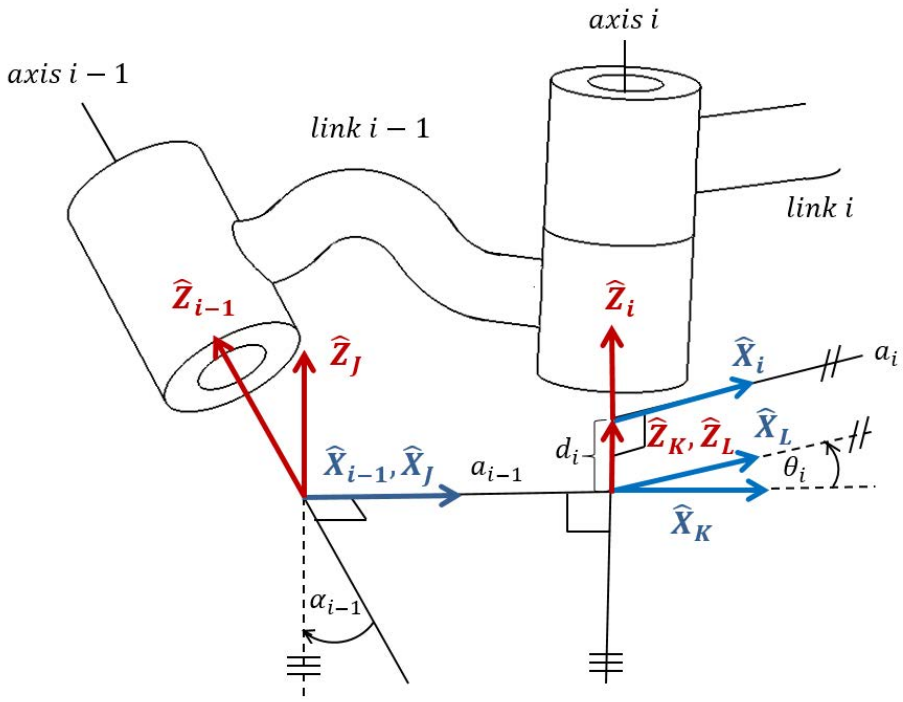

Figure 4. 13: Location of intermediate frames {J}, {K} and {L}.

Equation (4.9) can now be rewritten as

$$\begin{bmatrix} {}^{i-1}\boldsymbol{P} \\ 1 \end{bmatrix} = {}^{i-1}_{J}\boldsymbol{T}\ {}^{J}_{K}\boldsymbol{T}\ {}^{K}_{L}\boldsymbol{T}\ {}^{L}_{i}\boldsymbol{T} \begin{bmatrix} {}^{i}\boldsymbol{P} \\ 1 \end{bmatrix}, \tag{4. 10}$$

therefore

$${}^{i-1}_{i}\boldsymbol{T} = {}^{i-1}_{J}\boldsymbol{T}\ {}^{J}_{K}\boldsymbol{T}\ {}^{K}_{L}\boldsymbol{T}\ {}^{L}_{i}\boldsymbol{T}. \tag{4. 11}$$

The following notation is used to describe the rotations and translations possible in a transformation [72]:

Let $\boldsymbol{R}_K(\theta)$ be the rotational operator that performs a rotation of θ degrees about the axis with a direction defined by $\widehat{\boldsymbol{K}}$. The matrix for this operator is constructed as a homogeneous transform with a position vector containing zero's

$$\boldsymbol{R}_K(\theta) = \begin{bmatrix} [\boldsymbol{C}_K(\theta)] & \begin{matrix} 0 \\ 0 \\ 0 \end{matrix} \\ \begin{matrix} 0 & 0 & 0 \end{matrix} & 1 \end{bmatrix}, \tag{4. 12}$$

where $[\boldsymbol{C}_K]$ is the standard 3×3 rotation matrix used to rotate a vector around the axis determined by $\widehat{\boldsymbol{K}}$.

Let $\boldsymbol{D}_{\boldsymbol{G}}(G)$ represent a translation along the vector direction defined by $\boldsymbol{G}$ with a signed magnitude of G. The matrix for this operator is a homogeneous transform with the following form:

$$\boldsymbol{D}_{\boldsymbol{G}}(G) = \begin{bmatrix} 1 & 0 & 0 & G_x \\ 0 & 1 & 0 & G_y \\ 0 & 0 & 1 & G_z \\ 0 & 0 & 0 & 1 \end{bmatrix}, \tag{4. 13}$$

where, $G = \sqrt{G_x^2 + G_y^2 + G_z^2}$. G_x, G_y and G_z are the components of the translation vector $\boldsymbol{G}$.

Equation (4.11) can be simplified by considering each of the transformations individually. The transformation ${}^{i-1}_{J}\boldsymbol{T}$ is a rotation of angle α_{i-1} about the $\widehat{\boldsymbol{X}}$ axis and can therefore be reduced to $\boldsymbol{R}_X(\alpha_{i-1})$. The transformation ${}^{J}_{K}\boldsymbol{T}$ is a translation of length a_{i-1} along the $\widehat{\boldsymbol{X}}$ axis and can therefore be reduced to $\boldsymbol{D}_X(a_{i-1})$. The transformation ${}^{K}_{L}\boldsymbol{T}$ is a rotation about the $\widehat{\boldsymbol{Z}}$ axis by an angle of θ_i and can therefore be reduced to $\boldsymbol{R}_Z(\theta_i)$. Lastly, ${}^{L}_{i}\boldsymbol{T}$ is a translation along the $\widehat{\boldsymbol{Z}}$ axis of magnitude d_i and can therefore be reduced to $\boldsymbol{D}_Z(d_i)$. Equation (4.11) can now be written as

$${}^{i-1}_{i}\boldsymbol{T} = \boldsymbol{R}_X(\alpha_{i-1})\, \boldsymbol{D}_X(a_{i-1})\, \boldsymbol{R}_Z(\theta_i)\, \boldsymbol{D}_Z(d_i). \tag{4. 14}$$

By expanding (4.14), the general form for the transformation between neighbouring links is given by

$${}^{i-1}_{i}\boldsymbol{T} = \begin{bmatrix} \cos(\theta_i) & -\sin(\theta_i) & 0 & a_{i-1} \\ \sin(\theta_i)\cos(\alpha_{i-1}) & \cos(\theta_i)\cos(\alpha_{i-1}) & -\sin(\alpha_{i-1}) & -\sin(\alpha_{i-1})\, d_i \\ \sin(\theta_i)\sin(\alpha_{i-1}) & \cos(\theta_i)\sin(\alpha_{i-1}) & \cos(\alpha_{i-1}) & \cos(\alpha_{i-1})\, d_i \\ 0 & 0 & 0 & 1 \end{bmatrix}. \tag{4. 15}$$

The PhantomX® hexapod robot leg kinematic model can now be derived using

$$\begin{bmatrix} {}^{0}\boldsymbol{P} \\ 1 \end{bmatrix} = {}^{0}_{1}\boldsymbol{T}\, {}^{1}_{2}\boldsymbol{T}\, {}^{2}_{3}\boldsymbol{T}\, {}^{3}_{4}\boldsymbol{T} \begin{bmatrix} {}^{4}\boldsymbol{P} \\ 1 \end{bmatrix}. \tag{4. 16}$$

Using link parameters as described in Table 4.1 together with (4.15), the respective transformation matrices are given as follows

$$ {}^{0}_{1}\boldsymbol{T} = \begin{bmatrix} \cos(\theta_1) & -\sin(\theta_1) & 0 & 0 \\ \sin(\theta_1) & \cos(\theta_1) & 0 & 0 \\ 0 & 0 & 1 & 0 \\ 0 & 0 & 0 & 1 \end{bmatrix}, \tag{4. 17} $$

$$ {}^{1}_{2}\boldsymbol{T} = \begin{bmatrix} \cos(\theta_2) & -\sin(\theta_2) & 0 & 0.052 \\ 0 & 0 & -1 & 0 \\ \sin(\theta_2) & \cos(\theta_2) & 0 & 0 \\ 0 & 0 & 0 & 1 \end{bmatrix}, \tag{4. 18} $$

$$ {}^{2}_{3}\boldsymbol{T} = \begin{bmatrix} \cos(\theta_3) & -\sin(\theta_3) & 0 & 0.066221 \\ \sin(\theta_3) & \cos(\theta_3) & 0 & 0 \\ 0 & 0 & 1 & 0 \\ 0 & 0 & 0 & 1 \end{bmatrix}, \tag{4. 19} $$

$$ {}^{3}_{4}\boldsymbol{T} = \begin{bmatrix} 1 & 0 & 0 & 0.138964 \\ 0 & 1 & 0 & 0 \\ 0 & 0 & 1 & 0 \\ 0 & 0 & 0 & 1 \end{bmatrix}. \tag{4. 20} $$

Let ${}^{4}\boldsymbol{P}$ be located on the origin of $frame\ \{4\}$, then

$$ {}^{4}\boldsymbol{P} = \begin{bmatrix} 0 \\ 0 \\ 0 \end{bmatrix}. \tag{4. 21} $$

By substituting (4.17)-(4.20) into (4.16), it is possible to calculate ${}^{0}\boldsymbol{P}$, the foot position of the leg described from the origin of the leg, as

$$ {}^{0}\boldsymbol{P} = \begin{bmatrix} {}^{0}P_x \\ {}^{0}P_y \\ {}^{0}P_z \end{bmatrix} = \tag{4. 22} $$

$$ \begin{bmatrix} a_1\cos(\theta_1) + a_2\cos(\theta_1)\cos(\theta_2) + a_3\cos(\theta_1)\cos(\theta_2)\cos(\theta_3) - a_3\cos(\theta_1)\sin(\theta_2)\sin(\theta_3) \\ a_1\sin(\theta_1) + a_2\cos(\theta_2)\sin(\theta_1) - a_3\sin(\theta_1)\sin(\theta_2)\sin(\theta_3) + a_3\cos(\theta_2)\cos(\theta_3)\sin(\theta_1) \\ a_2\sin(\theta_2) + a_3\cos(\theta_2)\sin(\theta_3) + a_3\cos(\theta_3)\sin(\theta_2) \end{bmatrix}, $$

where, $a_1 = 0.0520$ m, $a_2 = 0.0662$ m and $a_3 = 0.1389$ m.

4.5 Kinematic model for hexapod robot

By translating the kinematic model derived for the robot leg into the body coordinate frame, the kinematic model for the entire hexapod robot can be derived.

4.5.1 Body coordinate frame

The body coordinate frame $\boldsymbol{B}$ for the robot is chosen to align with the position of the inertial sensor's internal coordinate frame. Fig. 4.14 shows the location of the body coordinate frame on the robot

body as well as the measurements defining the relationship between the body coordinate frame and the origin of each leg.

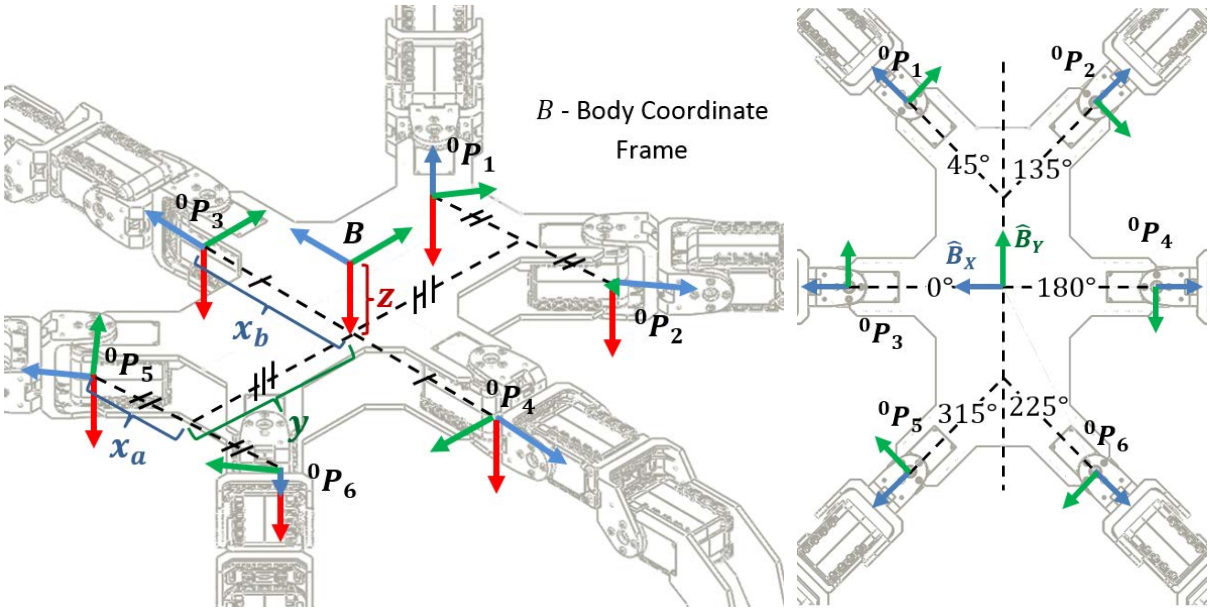

Figure 4. 14: Relationship between the body coordinate frame and origin of legs.

By considering Fig. 4.14, the kinematic model of a single leg can be transformed into the robot kinematic model.

4.5.2 Robot kinematic model

Let ${}^0\boldsymbol{P}_i$, represent the foot position of leg i as seen from the origin of the leg i. That means, ${}^0\boldsymbol{P}_i$ is the result given by the leg kinematic model for leg i. From Fig. 4.14 it is clear that for each leg, the leg kinematic model will have to undergo a rotation about the Z-axis ($\boldsymbol{C}_Z(\beta_i)$), as well as translations in all axes (p_x, p_y, p_z). This transformation, needed to describe the foot position of leg i in terms of the body coordinate frame, is represented by

$$\begin{bmatrix} {}^B\boldsymbol{P}_i \\ 1 \end{bmatrix} = \begin{bmatrix} \begin{bmatrix} \boldsymbol{C}_Z(\beta_i) \end{bmatrix} & \begin{bmatrix} p_x \\ p_y \\ p_z \end{bmatrix} \\ \begin{bmatrix} 0 & 0 & 0 \end{bmatrix} & 1 \end{bmatrix} \begin{bmatrix} {}^0\boldsymbol{P}_i \\ 1 \end{bmatrix}. \quad (4.\ 23)$$

Table 4.2 provides the parameter values used in (4.23) to derive the robot kinematic model.

Table 4. 2: Measurements used to derive the robot kinematic model.

i	β [°]	p_x [m] ($x_a = 0.0605$ $x_b = 0.1005$)	p_y [m] ($y = 0.1206$)	p_z [m] ($z = 0.0265$)
1	45	x_a	y	z
2	135	$-x_a$	y	z
3	0	x_b	0	z
4	180	$-x_b$	0	z
5	315	x_a	$-y$	z
6	225	$-x_a$	$-y$	z

By substituting the translation values as given in Table 4.2 into (4.23), one can derive the kinematic model of the robot in order to determine the foot positions with respect to the body coordinate frame. For better readability the robot's kinematic equations, $\boldsymbol{kin}_i(\boldsymbol{\theta})$, are given separately for each leg i. Here, $\boldsymbol{\theta} = [\theta_1, \theta_2, \theta_3]$ as defined in (4.22). Furthermore, the symbols as defined in Table 4.2 and the measurement quantities as defined in (4.22) are used.

Leg one:

$$\boldsymbol{kin}_1(\boldsymbol{\theta}) = [{}^B\boldsymbol{P}_1] = \begin{bmatrix} x_a + \frac{(2^{0.5} \times {}^0\boldsymbol{P}_{x_1})}{2} - \frac{(2^{0.5} \times {}^0\boldsymbol{P}_{y_1})}{2} \\ y + \frac{(2^{0.5} \times {}^0\boldsymbol{P}_{x_1})}{2} + \frac{(2^{0.5} \times {}^0\boldsymbol{P}_{y_1})}{2} \\ {}^0\boldsymbol{P}_{z_1} + z \end{bmatrix}. \quad (4.24)$$

Leg two:

$$\boldsymbol{kin}_2(\boldsymbol{\theta}) = [{}^B\boldsymbol{P}_2] = \begin{bmatrix} -x_a - \frac{(2^{0.5} \times {}^0\boldsymbol{P}_{x_2})}{2} - \frac{(2^{0.5} \times {}^0\boldsymbol{P}_{y_2})}{2} \\ y + \frac{(2^{0.5} \times {}^0\boldsymbol{P}_{x_2})}{2} + \frac{(2^{0.5} \times {}^0\boldsymbol{P}_{y_2})}{2} \\ {}^0\boldsymbol{P}_{z_2} + z \end{bmatrix}. \quad (4.25)$$

Leg three:

$$\boldsymbol{kin}_3(\boldsymbol{\theta}) = [{}^B\boldsymbol{P}_3] = \begin{bmatrix} {}^0\boldsymbol{P}_{x_3} + x_b \\ {}^0\boldsymbol{P}_{y_3} \\ {}^0\boldsymbol{P}_{z_3} + z \end{bmatrix}. \quad (4.26)$$

Leg four:

$$\boldsymbol{kin}_4(\boldsymbol{\theta}) = [{}^B\boldsymbol{P}_4] = \begin{bmatrix} -{}^0\boldsymbol{P}_{x_4} - x_b \\ -{}^0\boldsymbol{P}_{y_4} \\ {}^0\boldsymbol{P}_{z_4} + z \end{bmatrix}. \quad (4.\ 27)$$

Leg five:

$$\boldsymbol{kin}_5(\boldsymbol{\theta}) = [{}^B\boldsymbol{P}_5] = \begin{bmatrix} x_a + \frac{(2^{0.5} \times {}^0\boldsymbol{P}_{x_5})}{2} + \frac{(2^{0.5} \times {}^0\boldsymbol{P}_{y_5})}{2} \\ -y - \frac{(2^{0.5} \times {}^0\boldsymbol{P}_{x_5})}{2} + \frac{(2^{0.5} \times {}^0\boldsymbol{P}_{y_5})}{2} \\ {}^0\boldsymbol{P}_{z_5} + z \end{bmatrix}. \quad (4.\ 28)$$

Leg six:

$$\boldsymbol{kin}_6(\boldsymbol{\theta}) = [{}^B\boldsymbol{P}_6] = \begin{bmatrix} -x_a - \frac{(2^{0.5} \times {}^0\boldsymbol{P}_{x_6})}{2} + \frac{(2^{0.5} \times {}^0\boldsymbol{P}_{y_6})}{2} \\ -y - \frac{(2^{0.5} \times {}^0\boldsymbol{P}_{x_6})}{2} - \frac{(2^{0.5} \times {}^0\boldsymbol{P}_{y_6})}{2} \\ {}^0\boldsymbol{P}_6 + z \end{bmatrix}. \quad (4.\ 29)$$

4.6 Kinematic measurement model

The kinematic model $\boldsymbol{kin}_i(\boldsymbol{\theta})$ for leg i of the robot computes the location of each foot with respect to the body coordinate frame. However, for the state estimation of the robot, errors have to be taken into account that might affect the accuracy of the kinematic model. These can include erroneous calibration of the position sensors and errors in the kinematic model such as inaccuracies in measurements of the rigid bodies. $\boldsymbol{s}_i$ is defined as a vector pointing from the body coordinate frame to the contact point of foot i. For the errors affecting the kinematic model, following Bloesch et al.[2], the discrete Gaussian noise terms $\boldsymbol{n}_{s,i}$ is added in the model:

$$\boldsymbol{s}_i = \boldsymbol{kin}_i(\boldsymbol{\theta}) + \boldsymbol{n}_{s,i}\,. \quad (4.\ 30)$$

Let $\boldsymbol{R}_s$ be the covariance matrix for the noise $\boldsymbol{n}_{s,i}$.

4.7 Conclusion

In this chapter the kinematic model for the robot platform was derived. Background information regarding descriptions and specific operators used in this study was firstly discussed. Important

information about the robot platform was also given. This included the servo motor ID locations that are referenced throughout this study. A photo of the final robot platform was also provided along with a list of the components integrated onto the original PhantomX® platform.

The derivation of the robot kinematic model was done in a two-step process. Firstly, a model was derived for a leg of the robot. Here, link parameters were derived and frames were affixed to these links. The derivation of the link transformations were also completed. Secondly, the leg kinematic model was used to derive the final robot kinematic model. This was done by translating the leg kinematic model into the body coordinate frame for each leg.

This chapter concluded with a discussion regarding the kinematic measurement model. The sensory devices chosen for this study to be integrated onto the robot platform will now be discussed. For each of the sensory devices chosen, a measurement model will be derived. These measurement models along with the kinematic measurement model derived in this chapter will be used for the state estimation of the robot.

Chapter 5: Sensory system

"Remember that all models are wrong; the practical question is how wrong do they have to be to not be useful."

~ George Edward Pelham Box

5.1 Introduction

In this chapter the sensory system developed for this study is discussed. The sensory devices chosen for this study are firstly discussed. Some information regarding the implementation of the sensory measurements are also given. The method followed to acquire the sensor data is then discussed. The chapter concludes with the derivation of the measurement models to describe the noise processes of the sensor measurements. Standard deviation quantities are also assigned to the noise processes.

5.2 Sensory devices

This section discusses the specific sensory devices chosen for the proprioceptive sensory system used in this study. These sensory devices were chosen to comply with the requirements as set out in Chapter 3.

5.2.1 Joint position Sensors

The PhantomX® [51] hexapod robot platform used in this study makes use of AX-12A Dynamixel servo motors [77] with resistive potentiometers that provide joint position feedback. The joint position feedback provide the angular positions for all the joints as needed by the kinematic model for the robot. The AX-12A allows 0-300° of movement with a control and feedback range of 0-1023 bits.

An advantage specifically related to the Dynamixel servo design is that the potentiometer is placed on the output shaft and not directly after the motor, i.e. before the gears. This means that any play amongst the gear teeth that has a direct influence on the final movement is considered in the feedback readings [71].

Research conducted by Tira-Thompson [78] shows that the Dynamixel AX-12A servo's position feedback regarding a target position is very accurate (0.36°) when under no load. As the load on the servo increases the deflection from the target position increases. (Note that the position feedback regarding the real shaft position is not influenced by added load on the servo.) According to research

conducted by Tira-Thompson [78] one can assume that the AX-12A provides position feedback within 0.5° of accuracy. By making use of the servo motor's position feedback, extra joint position sensors are not needed.

5.2.1.1 Implementation of the kinematic model

The robot kinematic model derived in Chapter 4 determines the foot position of leg i with respect to the body coordinate system, given the joint angles θ_1, θ_2 and $\theta_3$of the leg. These joint angles have to be provided by position sensor feedback from the Dynamixel® servo motors installed on the robot platform. However, there exist some differences between the angle references of the kinematic model and the angle feedback given by the servo motors. In order for the kinematic model to provide the correct foot positions, these differences have to be taken into account and corrected by performing certain angle translations. This section will discuss the specific differences as well as the angle translations performed.

Servo angle feedback

The first angle translation that needs to be performed is due to the difference between the angle feedback of the servos and the angle reference used in the kinematic model. Fig. 5.1 shows how the Dynamixel® [77] servos of the robot provide angle feedback.

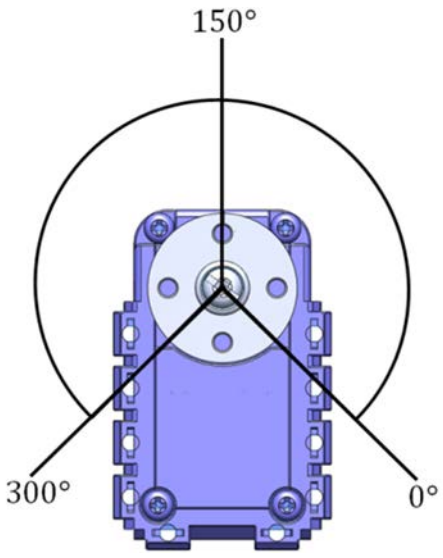

Figure 5. 1: Angle feedback of a Dynamixel AX12 servo.

By comparing the reference used in the kinematic model to the reference used by the servo motor, it was found that the $0°$ reference of the kinematic model is at the $150°$ point of the measured servo angle feedback, θ_{servo} . Therefore, depending on the mounting of the specific servo, it is required to subtract $150°$ from the angle feedback or the angle feedback has to be subtracted from $150°$. The

translated servo position feedback, $\theta_{translated}$, is the result of this translation for the specific servo motors:

For the servo motors with the following ID numbers: 1, 2, 4, 6, 7, 8, 10, 12, 13, 14, 16 and 18

$$\theta_{translated} = 150° - \theta_{servo}. \quad (5.1)$$

For the servo motors with the following ID numbers: 3, 5, 9, 11, 15 and 17

$$\theta_{translated} = \theta_{servo} - 150°. \quad (5.2)$$

Leg structure

Each rigid body of the leg consists of a servo motor that is connected to one or more brackets. By examining the femur and tibia of the robot leg, it is found that the servo motor for each does not align with the mathematical link allocation given for the kinematic model. This is made clear in Fig. 5.2. There exists a $13.09°$ difference between the servo motor of the femur and $link\ 2$ and a $45.36°$ difference between the servo motor in the tibia and $link\ 3$.

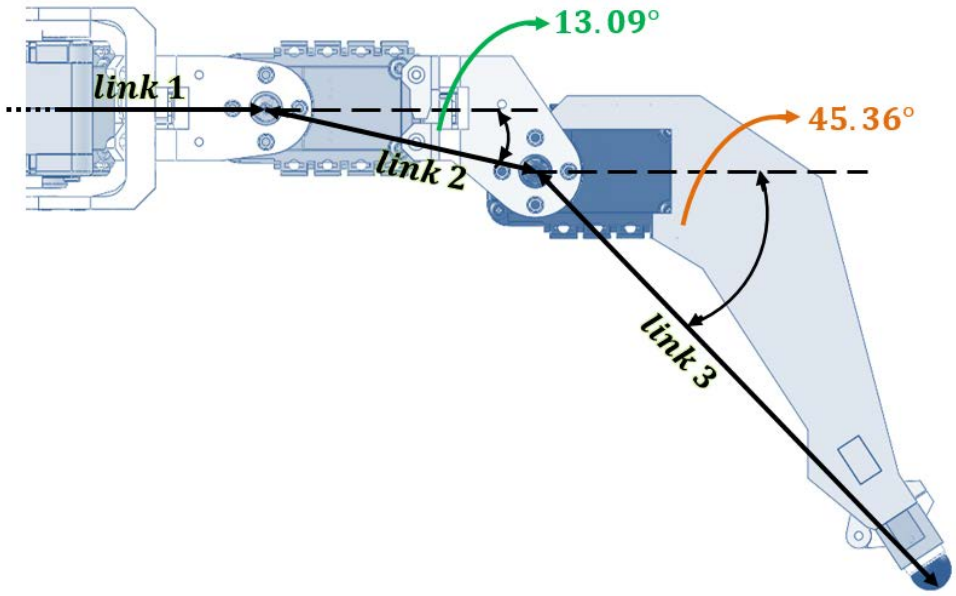

Figure 5. 2: Relationship between the leg structure and link location.

The differences between the leg structure and the mathematical model used in the kinematic model can be eliminated by the following translations:

For the servo motors with the following ID numbers: 3, 4, 9, 10, 15 and 16

$$\theta = \theta_{translated} + 13.09°. \quad (5.3)$$

For the servo motors with the following ID numbers: 5, 6, 11, 12, 17 and 18

$$\theta = \theta_{translated} + 45.36° - 13.09°. \quad (5.4)$$

The combination of (5.1)-(5.4) defines the total degree translations needed in order to transform the servo motor angle feedback to comply with the joint angles needed by the kinematic model:

For the servo motors with the following ID numbers: 1, 2, 7, 8, 13 and 14

$$\theta_1 = 150° - \theta_{servo}. \quad (5.5)$$

For the servo motors with the following ID numbers: 3, 9 and 15

$$\theta_2 = \theta_{servo} - 136.91°. \quad (5.6)$$

For the servo motors with the following ID numbers: 4, 10 and 16

$$\theta_2 = 163.09° - \theta_{servo}. \quad (5.7)$$

For the servo motors with the following ID numbers: 5, 11 and 17

$$\theta_3 = \theta_{servo} - 117.73°. \quad (5.8)$$

For the servo motors with the following ID numbers: 6, 12 and 18

$$\theta_2 = 182.27° - \theta_{servo}. \quad (5.9)$$

5.2.2 MicroStrain 3DM-GX3-25

The MicroStrain 3DM-GX3-25 miniature attitude heading reference system (AHRS) was chosen for this study. It is a low cost, high-performance inertial sensor that can be applied in a wide range of applications (e.g., inertial aiding of GPS, unmanned vehicle navigation, platform stabilization, robotic control, personal tracking, etc.) [79]. The device utilises MEMS sensor technology and integrates a triaxial accelerometer, a triaxial gyroscope, a triaxial magnetometer, five temperature sensors as well as an on-board processor. The device weighs 18 grams and is $44\ \text{mm} \times 24\ \text{mm} \times 11\ \text{mm}$ in size. Fig. 5.3 shows a picture of the 3DM-GX3-25 sensor device.

Figure 5. 3: MicroStrain 3DM-GX3-25 inertial sensor [79].

The 3DM-GX3-25 offers the following fully calibrated measurements for an operating temperature of $-40\ ^{\circ}\mathrm{C}$ to $70\ ^{\circ}\mathrm{C}$: acceleration, angular rate, magnetic field, delta-theta and delta-velocity vectors, Euler angles, rotation matrix and quaternion. It provides an attitude heading range of $360\ ^{\circ}/\mathrm{s}$ about all three axes with an accelerometer range of ± 5 g and a gyroscope range of $\pm\ 300\ ^{\circ}/\mathrm{s}$. The sensor supports an USB 2.0 or RS232 interface and has a micro-DB9 connector. Its data output rate is up to 1000 Hz with baud rate options of 115200 bps to 921600 bps. The sensor can be supplied with a direct current supply of $+3.2$ V to $+16$ V and consumes 80 mA@ 5V with USB. (The data sheet for this device can be found in Appendix B.)

The measured acceleration quantity given by the IMU, $\boldsymbol{f_{IMU}}$, is scaled into the physical unit of g-force acceleration g, where $1\ \mathrm{g} = g = 9.80665\ \mathrm{m/s^2}$. The proper acceleration $\boldsymbol{f}$ is therefore related to the measured acceleration as follows

$$\boldsymbol{f} = g\ \times\ \boldsymbol{f_{IMU}}. \tag{5. 10}$$

The measured gravitational acceleration varies from the standard $9.80665\ \mathrm{m/s^2}$ depending on the geographical location where the sensor is used. The following formula is used to determine the local gravitational acceleration [80]:

$$g_l = 9.780318\ (1 + 0.0053024 \sin^2(L) - 0.0000058 \sin^2(2L)) - 3.086 \times 10^{-6} h, \tag{5. 11}$$

where, g_l is the locally measured acceleration of gravity $[\mathrm{m/s^2}]$, L is the latitude $[^{\circ}]$ and h is the altitude $[\mathrm{m}]$ above sea level for the specific location. In order for (5.10) to provide the correct proper acceleration, the locally measured gravitational acceleration needs to be deducted from the measured acceleration, and replaced with the standard value of $9.80665\ \mathrm{m/s^2}$. By using the rotation matrix $\boldsymbol{C_{IMU}}$ provided by the IMU, one can redefine (5.10) as:

$$\boldsymbol{f} = (\boldsymbol{f_{IMU}} \times g) - (\boldsymbol{C_{IMU}} \times \boldsymbol{g_l})\ +\ (\boldsymbol{C_{IMU}} \times \boldsymbol{g})\ , \tag{5. 12}$$

where $\boldsymbol{g}$ is the standard gravity vector

$$\boldsymbol{g} = \begin{bmatrix} 0 \\ 0 \\ -g \end{bmatrix}, \tag{5. 13}$$

and $\boldsymbol{g_l}$ is the local measured gravity vector

$$\boldsymbol{g_l} = \begin{bmatrix} 0 \\ 0 \\ -g_l \end{bmatrix}. \tag{5. 14}$$

For the state estimation of the robot the IMU is used to provide the proper acceleration and the angular rate $\boldsymbol{\omega}$ of the robot's main body. The relationship between the proper acceleration and the absolute acceleration $\boldsymbol{a}$ is given by

$$\boldsymbol{f} = \boldsymbol{C}(\boldsymbol{a} - \boldsymbol{g}). \tag{5. 15}$$

The rotation matrix $\boldsymbol{C}$ is responsible for the rotation of coordinates represented in the inertial coordinate frame $\boldsymbol{I}$ into the body coordinate frame $\boldsymbol{B}$.

5.2.3 Force Sensors

With regard to the state estimation for this study, Bloesch et al. [2] stated that they experienced a $10\ \%$ drift in the estimated travelled distance of their robot which can be a result of fault-prone contact detection. The foot contact detection will be used in the state estimation of the robot to define the value of a specific noise parameter defined for a certain foothold (Chapter 6). The foot contact state for any given leg with a known robot pose can be estimated by the robot's kinematic model. Due to the limited control of the robot platform at this stage of development, detecting the feet contact states through the kinematic model will only be viable when the robot navigates on an even surface.

In order to minimise drift in our estimation and to provide a basis for future work, it was decided to include force sensors on the robot platform to provide the foot contact information needed. The force sensors are integrated into the hexapod's feet. A201 type FlexiForce sensors [73], distributed by Tekscan, were chosen for this study [73]. These sensors are ultra-thin, light in weight and flexible. The FlexiForce sensor is a force sensing resistor, decreasing in resistance value as a force is being applied to the sensing area. They can easily be included in a number of standard electronic circuit designs and used as an analogue input, as needed by software. The specific model integrated onto the robot can measure 0 to 100 N and has a response time smaller than 5 ms. Fig. 5.4 shows a picture of the A201 sensor.

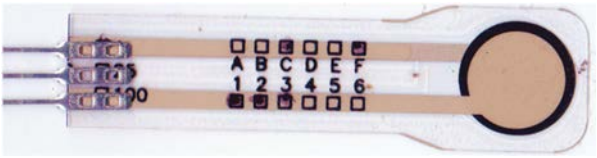

Figure 5. 4: A201 FlexiForce sensor.

For this study the FlexiForce sensors will only be used as on-off devices indicating if the feet are in contact with the ground or not. Each sensor was therefore integrated into a comparator circuit making use of an operational amplifier to produce a high analogue voltage output when the foot has no ground contact and a $0\ \mathrm{V}$ analogue output when the foot has ground contact. See Appendix B for physical information on the sensors as well as the electronic circuit used to integrate the sensors onto the platform.

5.3 Sensory system data acquisition

This section discusses the data acquisition of the IMU, joint position sensors and the force sensors. With regards to this study, the purpose of the sensory system is to provide the necessary measurements needed for state estimation. For the state estimation of the robot, the following sensory data needed to be collected: The position feedback from all 18 servo motors, ground contact status from the force sensors, and acceleration, angular rate, time stamp and quaternion measurements from the IMU.

5.3.1 Data Acquisition Frequency

Data acquisition frequency refers to the rate at which the data from the sensors is captured by the sensory system. A sensor acquisition frequency of $20\ \mathrm{Hz}$ was chosen experimentally. This is because the movement of the robot became intermittent when servo position feedback was requested at higher frequencies. It is important to note that this limitation is brought on by the restrictions in the current control of the robot and can be improved with the development of the robot control in future work.

For successful state estimation of the robot, a single leg movement should be shown in the sensor data. Therefore, the sensor data acquisition speed should be faster than the robot moving a leg to a new position and each contact position should be recorded. In order to validate that a data acquisition speed of $20\ \mathrm{Hz}$ is fast enough for state estimation of the robot, the robot was filmed with a high speed camera to show the distance travelled by the robot at full speed every $50\ \mathrm{ms}$. Fig. 5.5 illustrates four frames captured by the high speed camera at $50\ \mathrm{ms}$ intervals.

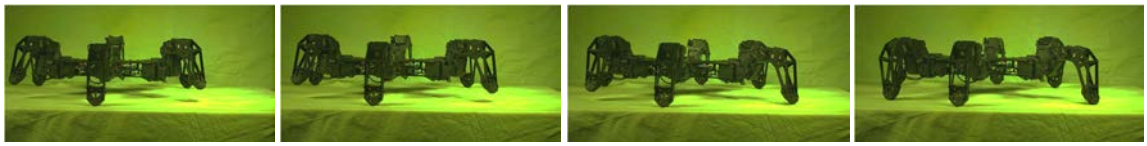

Figure 5. 5: Robot Platform Captured by High Speed Camera (left photo = first frame).

From the high speed camera test, it was found that when the robot is walking at its fastest speed, it takes seven frames, resulting in 0.35 s, to move a leg from one position to the next. One can therefore conclude that a data acquisition speed of 20 Hz is fast enough for the state estimation of the robot.

5.3.2 Data Acquisition Process

The need for a device that can capture and process all the sensor data was identified. A single board computer known as a UDOO [75] was integrated onto the robot platform to perform this task. UDOO is a mini PC with an ARM i.MX6 Freescale processor providing you with a choice between Linux and Android as operating system. It also has an Arduino DUE ARM making it fully Arduino compatible and multiple I/O pins for sensors [75]. For this study, Linux was used as an operating system and the data acquisition process was implemented with an executable program coded in the Python IDE.

The control of the robot platform is out of the scope of this study. Currently the robot platform is controlled with inputs from a remote controller that communicates with firmware uploaded onto the ArbotiX-M Robocontroller board integrated in the robot platform. Consequently the servo motors are controlled from the ArbotiX-M Robocontroller. Therefore, the position feedback was requested within the control firmware of the robot. Modifications was made to the firmware in order to send out the servo positions every 50 ms. The servo position measurements were then communicated to the UDOO through a software serial communication procedure. The specific firmware code modifications are discussed in Appendix A.

The analogue outputs indicating the ground contact status of each foot were directly connected to the UDOO's I/O pins. The status of the I/O pins of the UDOO can be accessed by reading the value of each specific pin in a register of the operating system. The IMU sensor was directly connected to the UDOO through a USB interface. The IMU was configured to send out its internal time stamp and acceleration, angular rate and quaternion measurements at 1000 Hz.

The architecture of the executable program that handled the data acquisition of the sensors is shown in Fig. 5.6. After the program was launched it waited for a *start recording* demand. This demand is controlled by an input created by a physical push button integrated onto the robot. The push button sends out an analogue value to an I/O pin on the UDOO. As soon as a high voltage value was recorded

in the specific I/O pin registry, the program initialised the serial port for the IMU communication and the software serial port to the ArbotiX-M Robocontroller. A text file was then created to store the sensor data.

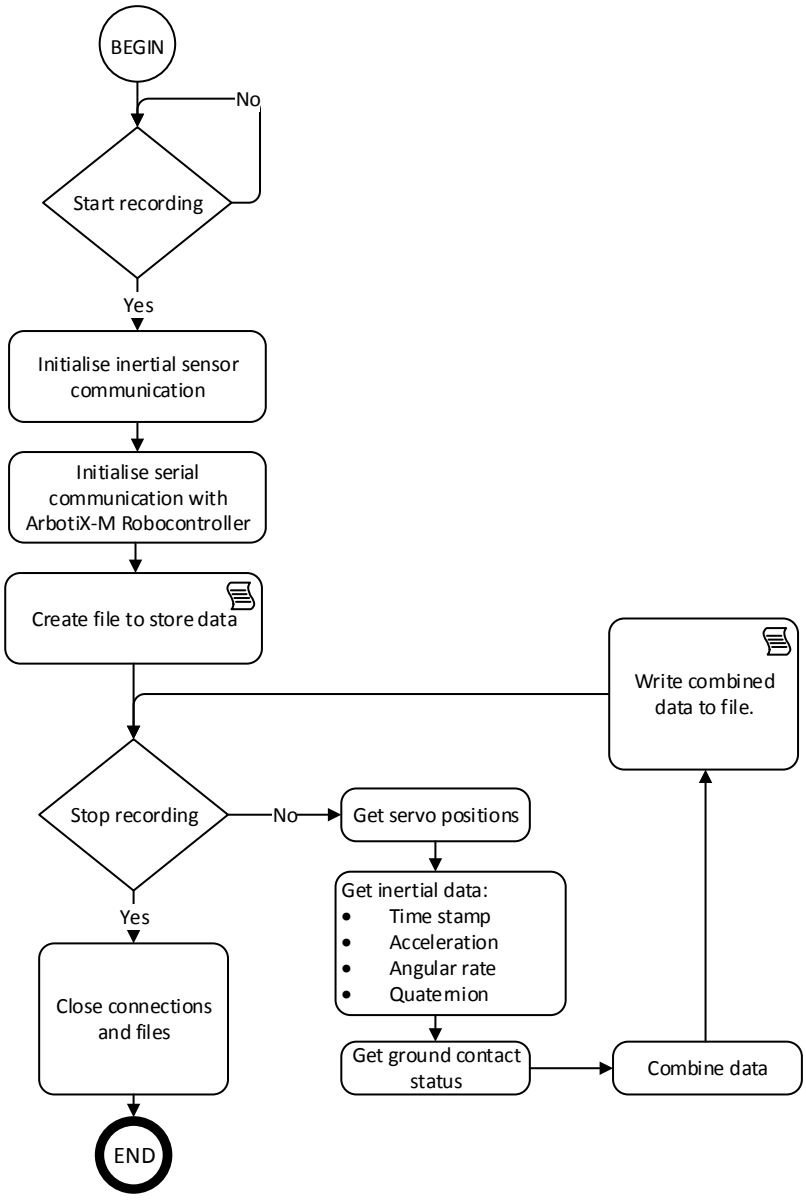

Figure 5. 6: Data acquisition program architecture.

After the text file was created the program entered a loop where the sensor data was recorded until the push button on the robot was triggered again. Inside the loop, the current servo positions were first read from the software serial port that communicates with the ArbotiX-M Robocontroller. As soon as a servo position data package was received, the latest inertial measurements were recorded from the inertial sensor. The ground contact status was then requested and also recorded. Because the IMU measurements are sent to the UDOO at $1000\,\mathrm{Hz}$ compared to the servo position

measurements' 20 Hz, an assumption can be made that all the recorded sensor data can be classified under the time stamp provided by the IMU. All of the sensor data was then combined in an array and saved to the text file for every loop.

The handling of errors induced in the sensor measurements are addressed in the state estimation approach by using measurement models derived for the IMU measurements and the joint position measurements. Since the force sensors are only implemented to provide on-off feedback and the response time of the sensors are much smaller than the data collecting frequency (20 Hz), the noise models of the force sensor will not be derived.

5.4 Measurement models

In this section measurement models are derived for the sensor measurements and standard deviation quantities are assigned to the noise processes affecting the sensors' measurements. Analogue quantities measured by sensors are subject to random noise effects. In order to produce an accurate estimate of the robot pose, knowledge about the sensor noise is required. By modelling the noise for a sensor as a stochastic process, it is possible to characterise their probabilistic behaviour.

As a simplification, all random noise affecting sensor measurements will be modelled as continuous white Gaussian noise or discrete Gaussian noise processes. This simplification is based on the central limit theorem [81]. Let $\mathbf{x}_i$ be n independent random variables (not necessarily of Gaussian type), with their summation

$$\mathbf{x} = \sum_{i=1}^{n} \mathbf{x}_i = \mathbf{x}_1 + \mathbf{x}_2 + \cdots + \mathbf{x}_n \,, \tag{5. 16}$$

a random variable with mean

$$\eta = \eta_1 + \eta_2 + \cdots + \eta_n \,, \tag{5. 17}$$

and variance

$$\sigma^2 = \sigma_1^2 + \sigma_2^2 + \cdots + \sigma_n^2 \,. \tag{5. 18}$$

The central limit theorem states the following [81]:

1) As n increases, the distribution of $\mathbf{x}$, $F(x)$, approaches a normal distribution with the same mean and variance:

$$F(x) \cong G\left(\frac{x-\eta}{\sigma}\right), \tag{5. 19}$$

where, $G(\cdot)$ represents a Gaussian distribution with mean,η, and standard deviation, σ.

2) If $\mathbf{x_i}$ are continuous random variables, the density of $\mathbf{x}$, $f(x)$, approaches a normal (Gaussian) density (Fig. 5.7):

$$f(x) \cong \frac{1}{\sigma\sqrt{2\pi}} e^{-(x-\eta)^2/2\sigma^2} \tag{5. 20}$$

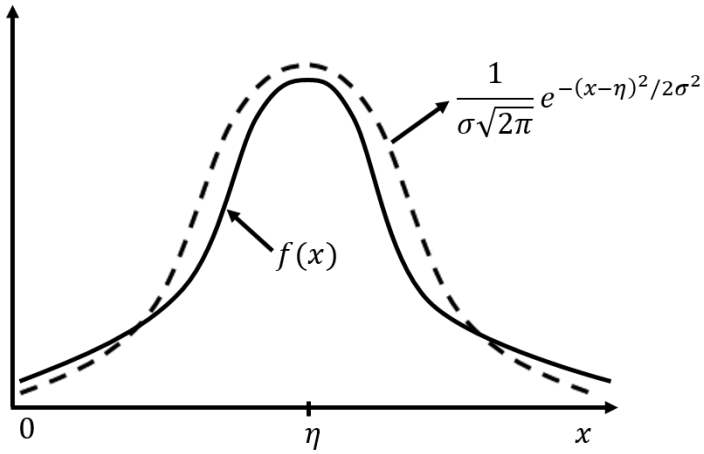

Figure 5. 7: Density function [81].

Since many noise variables are comprised of a sum of underlying random sources, the assumption that a variable has a Gaussian noise distribution is often valid. The assumption that the noises of the sensors in the robot are Gaussian noise, is seen as a trade-off between simplicity and accuracy. This simplification can be handled in the state estimation of the robot by increasing the corresponding covariance matrices. For each of the measurements provided by the sensory devices a corresponding measurement model will now be derived [2].

5.4.1 Joint position measurement model

For the measurement model of the joint position sensors, an assumption is made that the joint position measurement vector, $\tilde{\boldsymbol{\theta}}$, of the joint angles vector, $\boldsymbol{\theta}$, is affected by discrete Gaussian noise, $\boldsymbol{n}_\theta$:

$$\tilde{\boldsymbol{\theta}} = \boldsymbol{\theta} + \boldsymbol{n}_\theta. \tag{5. 21}$$

One can then define the covariance matrix, $\boldsymbol{R}_\theta$, for the noise process, $\boldsymbol{n}_\theta$, that is expressed in the body coordinate frame.

As mentioned, research conducted by Tira-Thompson [78] indicates a position feedback accuracy of 0.5°. The standard deviation of the noise process, $\boldsymbol{n_\theta}$, can now be defined as

$$\boldsymbol{\sigma_{n_\theta}} = 0.0087 \text{ rad}\,. \tag{5. 22}$$

5.4.2 IMU measurement model

For the state estimation of the robot, a model for the IMU is introduced. IMUs are prone to a number of different systematic and random errors. Systematic errors are caused by axis misalignment in manufacturing and scale factors. The 3DM-GX3-25 is factory calibrated for these systematic errors. All of the quantities provided by the device are temperature compensated and aligned mathematically to an orthogonal coordinate system. The angular rate is corrected to third order for g-sensitivity and scale factor non-linearity.

The probabilistic behaviour of the random noise influencing the IMU needs to be characterised. By modelling each noise source as a stochastic process, the following continuous stochastic models are introduced:

$$\tilde{\boldsymbol{f}} = \boldsymbol{f} + \boldsymbol{b}_f + \boldsymbol{w}_f\,, \tag{5. 23}$$

$$\dot{\boldsymbol{b}}_f = \boldsymbol{w}_{bf}\,, \tag{5. 24}$$

$$\tilde{\boldsymbol{\omega}} = \boldsymbol{\omega} + \boldsymbol{b}_\omega + \boldsymbol{w}_\omega\,, \tag{5. 25}$$

$$\dot{\boldsymbol{b}}_\omega = \boldsymbol{w}_{b\omega}. \tag{5. 26}$$

The measured acceleration $\tilde{\boldsymbol{f}}$ is affected by additive white Gaussian noise process $\boldsymbol{w}_f$ and bias term $\boldsymbol{b}_f$. The measured angular rate $\tilde{\boldsymbol{\omega}}$ is affected by additive white Gaussian noise process $\boldsymbol{w}_\omega$ and bias term $\boldsymbol{b}_\omega$. The derivatives of the bias terms, which are modelled as Brownian motions [2], are represented by $\boldsymbol{w}_{bf}$ and $\boldsymbol{w}_{b\omega}$, corresponding white Gaussian noise processes. $\boldsymbol{Q}_f$ and $\boldsymbol{Q}_{bf}$ are defined as the covariance parameters for the corresponding noise terms $\boldsymbol{w_f}$ and $\boldsymbol{w_{bf}}$ with corresponding variance parameters $\boldsymbol{\sigma}^2_{w_f}$ and $\boldsymbol{\sigma}^2_{w_{bf}}$. $\boldsymbol{Q_\omega}$ and $\boldsymbol{Q}_{b\omega}$ are defined as the covariance parameters for the corresponding noise terms $\boldsymbol{w}_\omega$ and $\boldsymbol{w}_{b\omega}$ with corresponding variance parameters $\boldsymbol{\sigma}^2_{w_\omega}$ and $\boldsymbol{\sigma}^2_{w_{b\omega}}$.

For the state estimation, as a simplification, one can assume that each covariance parameter is a diagonal matrix with identical diagonal entries:

$$\boldsymbol{Q}_f = \begin{bmatrix} \sigma_{w_f}^2 & 0 & 0 \\ 0 & \sigma_{w_f}^2 & 0 \\ 0 & 0 & \sigma_{w_f}^2 \end{bmatrix}, \tag{5. 27}$$

$$\boldsymbol{Q}_{bf} = \begin{bmatrix} \sigma_{w_{bf}}^2 & 0 & 0 \\ 0 & \sigma_{w_{bf}}^2 & 0 \\ 0 & 0 & \sigma_{w_{bf}}^2 \end{bmatrix}, \tag{5. 28}$$

$$\boldsymbol{Q}_{\omega} = \begin{bmatrix} \sigma_{w_{\omega}}^2 & 0 & 0 \\ 0 & \sigma_{w_{\omega}}^2 & 0 \\ 0 & 0 & \sigma_{w_{\omega}}^2 \end{bmatrix}, \tag{5. 29}$$

$$\boldsymbol{Q}_{b\omega} = \begin{bmatrix} \sigma_{w_{b\omega}}^2 & 0 & 0 \\ 0 & \sigma_{w_{b\omega}}^2 & 0 \\ 0 & 0 & \sigma_{w_{b\omega}}^2 \end{bmatrix}. \tag{5. 30}$$

MicroStrain provides a calibration certificate with each provided 3DM-GX3-25 IMU. The certificate confirms that the sensor meets the published specifications as provided on the sensor datasheet with regard to the noise parameters. By using these provided noise density specifications, the root power spectral density (PSD) of the additive white Gaussian noise parameters, w_f and w_ω, can now be defined as

$$w_f = 80\ \mu\text{g}/\sqrt{\text{Hz}} = 0.00078\ \text{m/s}^2/\sqrt{\text{Hz}}, \tag{5. 31}$$

$$w_\omega = 0.03\ °/\text{s}/\sqrt{\text{Hz}}\ = 0.00052\ \text{rad/s}/\sqrt{\text{Hz}}\,. \tag{5. 32}$$

The bias errors for the acceleration and the angular rate can each be divided into two parameters [68]. The first parameter is known as the initial bias $b_{initial}$ (also turn-on or fixed bias). The initial bias contains what is left of the residual bias after calibration and an uncertainty that differs for each start-up of the device. This parameter is therefore not a constant, but it can be assumed to be within a certain range. The second parameter is known as the in-run bias b_{in_run}. This parameter varies over short periods while the device is in use and depends on the sensitivity of the sensor with regards to temperature changes. The in-run bias is used to compute the standard deviation quantities.

Let the bias parameters for the IMU be defined as

$$b = b_{initial} + b_{in\_run}\,. \tag{5. 33}$$

From the specifications of the 3DM-GX3-25 as set out by MicroStrain, quantities can be given to the bias parameters [79]:

$$b_f = 2\ \text{mg} + 0.04\ \text{mg} = 2.04\ \text{mg} = 2.0005566\ \times 10^{-2}\ \text{m/s}^2, \tag{5. 34}$$

$$b_\omega = 0.25\,^\circ/\mathrm{s} \;+\; 0.005\,^\circ/\mathrm{s} \;=\; 0.255\,^\circ/\mathrm{s} \;= 4.450589593 \times 10^{-3}\ \mathrm{rad/s}. \quad (5.\ 35)$$

From [3], quantities can be provided for the continuous-time standard deviations of the bias noise processes, so that

$$\sigma_{w_{bf}} = 0.0001\ \mathrm{m/s^3}/\sqrt{\mathrm{Hz}}, \quad (5.\ 36)$$

$$\sigma_{w_{bf}} = 0.000618\ \mathrm{rad/s^2}/\sqrt{\mathrm{Hz}}. \quad (5.\ 37)$$

5.5 Conclusion

This chapter discussed the proprioceptive sensory system developed for the robot platform in order to perform the state estimation. The specific sensory devices chosen were firstly each discussed along with important implementation information. In order to acquire joint position feedback of the robot legs, the potentiometers in the Dynamixel servo motors were chosen. These servo motors are already integrated in the PhantomX hexapod robot. Differences between the servo motor feedback and assumptions made in the derived kinematic model of the robot were discussed. In order for the kinematic model to be implemented, some translations regarding the joint-angle feedback was necessary. These translations are brought on by the leg structure of the robot as well as the reference points of the position feedback from the servo motors. These translations need to be performed before the angle variables are used as an input to the kinematic model.

In order to acquire acceleration and angular rate feedback of the robot body, the 3DM-GX3-25 inertial sensor supplied by MicroStrain was chosen. The 3DM-GX3-25 IMU offers fully calibrated acceleration, angular rate, magnetic field, delta-theta and delta-velocity vectors, Euler angles, rotation matrix and quaternion measurements. This device was chosen because for its low-cost, it has very high performance ratings. Calculations needed to acquire the proper acceleration measurement for the robot in a specific geographical location were also discussed. Furthermore, the relationship between the absolute acceleration and the proper acceleration was provided.

The method followed for the sensor data acquisition was then discussed. Here, the data acquisition frequency was provided and validated. The data acquisition process was then discussed where the architecture of executable software program that was developed to obtain the sensors data measurements were provided. In order to handle errors induced in the sensor measurements, measurement models for the sensory devices were derived. These measurement models will be used in the state estimation approach. Standard deviation quantities were also assigned to the noise

processes defined in the measurement models. Using the information provided in Chapters 4 and 5, the state estimation approach can now be discussed and the state estimation equations can be derived.

Chapter 6: State estimation

> "I have been aware from the outset (end of January 1959, the birthdate of the second paper in the citation) that the deep analysis of something which is now called Kalman filtering were of major importance. But even with this immodesty I did not quite anticipate all the reactions to this work."
>
> *~ Rudolf E. Kálmán*

6.1 Introduction

This chapter discusses the state estimation done for the hexapod platform. The state estimation for the hexapod was derived using an estimation framework presented by Bloesch et al. [2] for legged robots, and also used by Rotella et al. [3]. The sources used for the state estimation framework does not include full details of the related derivations. Therefore, the derivations in this chapter will assist in providing the less visible details. Also, the framework is used to develop a state estimation methodology for specifically a hexapod robot.

The state estimation methodology developed fuses the leg kinematics (using the joint position sensors as input), as derived in chapter 4, with measurements from the IMU on the robot platform. The leg kinematics represents the relative pose measurements from the centre of the main body to each foot contact point. Without any assumptions about the terrain, the filter is designed to estimate the full 6 DOF state of the hexapod's main body and the ground geometry of where the robot is walking.

This chapter starts with background information including a discussion of the Kalman filter and the EKF. Thereafter, the states are defined, followed by the derivation of the prediction and measurement models. The prediction step is then discussed, where the continuous time differential equations are discretised and linearised in order to derive the discrete linearised noise covariance matrix, and the discrete process noise covariance matrix. Lastly, the update step of the EKF is discussed, where the measurement residual is formulated, the foot position measurement model is linearised, and the measurement Jacobian and noise matrices are derived.

6.2 Background

This section builds on the EKF information provided in Chapter 3 to discuss the EKF operation and provide the EKF equations.

6.2.1 The Extended Kalman filter

In 1960, R.E. Kalman published a paper providing a recursive solution to the linear optimal filtering problem [82]. For a state vector, $\boldsymbol{x}$, the Kalman filter provides a state estimate that is the expected value of the state computed from previous measurements together with a corresponding covariance matrix, $\boldsymbol{\mathcal{P}}$. The uncertainty regarding the estimate is specified within the covariance matrix. The Kalman filter operation can be explained in a two-step process, the *prediction step* and the *update step*. The prediction step produces the *a priori* state estimate, $\hat{\boldsymbol{x}}_k^-$, and a covariance matrix, $\boldsymbol{\mathcal{P}}_k^-$, using the expected value and the estimation error covariance of the state. The update step produces the *a posteriori* state estimate, $\hat{\boldsymbol{x}}_k^+$, and covariance matrix, $\boldsymbol{\mathcal{P}}_k^+$, by using a measurement to update the expected value and covariance of the state.

The main limitation of state estimation using the standard Kalman filter, is that it's only applicable in linear systems. Unfortunately, as in many engineering systems, the system presented in this study is nonlinear. Therefore, an extension of the standard Kalman filter for nonlinear systems, known as the *Extended Kalman filter* (EKF) will be used. The EKF is chosen due to its simplicity and low computation costs with respect to alternative solutions such as the Unscented Kalman filter and the Particle filter [3].

The operation of the EKF will now follow [3]. For a given nonlinear, continuous-time system, the system state and measurement systems can be described by the following general equations,

$$\dot{\boldsymbol{x}} = \boldsymbol{f}(\boldsymbol{x}, \boldsymbol{w}), \tag{6. 1}$$

$$\boldsymbol{y} = \boldsymbol{h}(\boldsymbol{x}, \boldsymbol{n}), \tag{6. 2}$$

with the *prediction* model being the nonlinear function $\boldsymbol{f}(\cdot)$, and the *measurement* model being the nonlinear function $\boldsymbol{h}(\cdot)$. Firstly, the EKF discretises the models, where,

$$\hat{\boldsymbol{x}}_k^- = \boldsymbol{f}(\hat{\boldsymbol{x}}_{k-1}^+), \tag{6. 3}$$

is the *a priori* state estimate or state prediction and,

$$\hat{\boldsymbol{y}}_k = \boldsymbol{h}(\hat{\boldsymbol{x}}_k^-), \tag{6. 4}$$

is the predicted measurement for time step k. Secondly, using a first-order Taylor series expansion, the prediction, (6.1), and measurement, (6.2), models are linearised around the *a priori* state estimate. The linearisation produces the prediction Jacobian,

$$\boldsymbol{F}_k = \left.\frac{\partial \boldsymbol{f}}{\partial \boldsymbol{x}}\right|_{\hat{\boldsymbol{x}}_k^-}, \tag{6. 5}$$

and the measurement Jacobian,

$$\boldsymbol{H}_k = \left.\frac{\partial \boldsymbol{h}}{\partial \boldsymbol{x}}\right|_{\hat{\boldsymbol{x}}_k^-}. \tag{6. 6}$$

In order to complete the prediction step, the *a priori* covariance is computed with the standard Kalman filter equation, using (6.5):

$$\boldsymbol{\mathcal{P}}_k^- = \boldsymbol{F}_k \boldsymbol{\mathcal{P}}_{k-1}^+ \boldsymbol{F}_k^T + \boldsymbol{Q}_k, \tag{6. 7}$$

where, $\boldsymbol{Q}_k$, is defined as the discrete process noise covariance.

The update step is completed using the standard Kalman filter equations. The predicted measurement, $\hat{\boldsymbol{y}}_k$, and actual measurement, $\boldsymbol{y}_k$, together with the *a priori* covariance, $\boldsymbol{\mathcal{P}}_k^-$, are used to update the state estimate and covariance matrix. The residual covariance is calculated with

$$\boldsymbol{S}_k = \boldsymbol{H}_k \boldsymbol{\mathcal{P}}_k^- \boldsymbol{H}_k^T + \boldsymbol{R}_k, \tag{6. 8}$$

where $\boldsymbol{R}_k$, is the discrete measurement noise covariance. The Kalman gain is given by

$$\boldsymbol{K}_k = \boldsymbol{\mathcal{P}}_k^- \boldsymbol{H}_k^T \boldsymbol{S}_k^{-1}. \tag{6. 9}$$

The *a posteriori* state estimate is given by

$$\hat{\boldsymbol{x}}_k^+ = \hat{\boldsymbol{x}}_k^- + \boldsymbol{K}_k(\boldsymbol{y}_k - \hat{\boldsymbol{y}}_k). \tag{6. 10}$$

Finally, the *a posteriori* covariance is calculated as

$$\boldsymbol{\mathcal{P}}_k^+ = (\mathbb{I} - \boldsymbol{K}_k \boldsymbol{H}_k)\boldsymbol{\mathcal{P}}_k^-, \tag{6. 11}$$

where, $\mathbb{I}$ is the identity matrix. With the general process of the EKF now explained, the state estimation for the hexapod platform can now be computed.

6.3 State definition of Extended Kalman filter

This section discusses the state vector definition for the filter used to do the state estimation of the hexapod robot. The following state vector for the hexapod robot platform was derived from the general state vector defined for a legged robot as set out by Bloesch et al. [2]:

$$\boldsymbol{x} \coloneqq \begin{pmatrix} \boldsymbol{r} & \boldsymbol{v} & \boldsymbol{q} & \boldsymbol{p}_1 & \boldsymbol{p}_2 & \boldsymbol{p}_3 & \boldsymbol{p}_4 & \boldsymbol{p}_5 & \boldsymbol{p}_6 & \boldsymbol{b}_f & \boldsymbol{b}_\omega \end{pmatrix}. \tag{6. 12}$$

In (6.1) $\boldsymbol{r}$, with $\boldsymbol{r} \in \mathbb{R}^3$, represents the position, and $\boldsymbol{v}$, with $\boldsymbol{v} \in \mathbb{R}^3$, the velocity of the centre of the body of the hexapod, expressed in the inertial coordinate frame $\boldsymbol{I}$. The kinematics of the legs of the hexapod are considered with the inclusion of the absolute foot contact point positions, $\boldsymbol{p}_i$, of the six feet expressed in the inertial coordinate frame $\boldsymbol{I}$, where $\boldsymbol{p}_i \in \mathbb{R}^3, i \in \{1, \dots, 6\}$. With regard to the IMU, $\boldsymbol{b}_f$, with $\boldsymbol{b}_f \in \mathbb{R}^3$, represents the accelerometer bias and $\boldsymbol{b}_\omega$, with $\boldsymbol{b}_\omega \in \mathbb{R}^3$, represents the gyroscope bias. Both are expressed in the body coordinate frame $\boldsymbol{B}$. The rotation from the inertial coordinate frame $\boldsymbol{I}$ into the body coordinate frame $\boldsymbol{B}$, is represented by the quaternion $\boldsymbol{q}$, with $\boldsymbol{q} \in \mathbb{R}^4$. Where,

$$\boldsymbol{q} = q_0 + q_1 i + q_2 j + q_3 k\,. \tag{6. 13}$$

The quaternion may be represented as a vector,

$$\boldsymbol{q} = [q_1 \quad q_2 \quad q_3 \quad q_0]^T. \tag{6. 14}$$

There exist two different conventions for using quaternions, therefore it is important to take note of the placement of the scalar part of the quaternion, q_0, in the vector defined in (6.14). This configuration will be used for all the quaternion calculations in this study.

Given the quaternion $\boldsymbol{q}$, the corresponding rotational matrix $\boldsymbol{C}$ can be determined with the following standard equation [83]:

$$\boldsymbol{C} = \begin{bmatrix} q_0^2 + q_1^2 - q_2^2 - q_3^2 & 2q_1q_2 + 2q_0q_3 & 2q_1q_3 - 2q_0q_2 \\ 2q_1q_2 - 2q_0q_3 & q_0^2 - q_1^2 + q_2^2 - q_3^2 & 2q_2q_3 + 2q_0q_1 \\ 2q_1q_3 + 2q_0q_2 & 2q_2q_3 - 2q_0q_1 & q_0^2 - q_1^2 - q_2^2 + q_3^2 \end{bmatrix}. \tag{6. 15}$$

The uncertainties of the estimated state vector, (6.12), of the EKF derived are represented with the covariance matrix, $\boldsymbol{\mathcal{P}}$, with a corresponding state error vector for the hexapod platform:

$$\boldsymbol{\delta x} := \left(\boldsymbol{\delta r} \quad \boldsymbol{\delta v} \quad \boldsymbol{\delta \phi} \quad \boldsymbol{\delta p}_1 \quad \boldsymbol{\delta p}_2 \quad \boldsymbol{\delta p}_3 \quad \boldsymbol{\delta p}_4 \quad \boldsymbol{\delta p}_5 \quad \boldsymbol{\delta p}_6 \quad \boldsymbol{\delta b}_f \quad \boldsymbol{\delta b}_\omega\right), \tag{6. 16}$$

$$\boldsymbol{\mathcal{P}} := Cov(\boldsymbol{\delta x}). \tag{6. 17}$$

It is important to notice that the error of the orientation is represented by $\boldsymbol{\delta \phi}$, a 3D rotation vector. This is due to the covariance term being represented by a 3-dimensional covariance matrix since $\boldsymbol{q}$ processes 3 degrees of freedom. The relationship between the estimate of the orientation quaternion, $\hat{\boldsymbol{q}}$, and the error quaternion, $\boldsymbol{\delta q}$, is defined by

$$\boldsymbol{q} = \boldsymbol{\delta q} \otimes \hat{\boldsymbol{q}}\,. \tag{6. 18}$$

In (6.18), $\otimes$ is the quaternion multiplication operator. Quaternion multiplication is not commutative. For two quaternions $\boldsymbol{a}$ and $\boldsymbol{b}$ defined as in (6.13) and (6.14), the multiplication between them is defined by

$$\begin{aligned}\boldsymbol{a}\otimes\boldsymbol{b} &= (a_0b_0 - a_1b_1 - a_2b_2 - a_3b_3) + (a_0b_1 + a_1b_0 - a_2b_3 + a_3b_2)i \\ &\quad + (a_0b_2 + a_1b_3 + a_2b_0 - a_3b_1)j + (a_0b_3 - a_1b_2 + a_2b_1 + a_3b_0)k \\ &= \begin{bmatrix} a_0b_1 + a_1b_0 - a_2b_3 + a_3b_2 \\ a_0b_2 + a_1b_3 + a_2b_0 - a_3b_1 \\ a_0b_3 - a_1b_2 + a_2b_1 + a_3b_0 \\ a_0b_0 - a_1b_1 - a_2b_2 - a_3b_3 \end{bmatrix} \\ &= Q(\boldsymbol{a})\boldsymbol{b},\end{aligned} \tag{6. 19}$$

where $Q(\cdot)$ maps a quaternion to its corresponding quaternion matrix [2], [83]:

$$Q(\boldsymbol{q}) = \begin{bmatrix} q_0\boldsymbol{I}_3 + \boldsymbol{q}_{1:3}^{\times} & \boldsymbol{q}_{1:3} \\ -\boldsymbol{q}_{1:3}^{T} & q_0 \end{bmatrix} = \begin{bmatrix} q_0 & q_3 & -q_2 & q_1 \\ -q_3 & q_0 & q_1 & q_2 \\ q_2 & -q_1 & q_0 & q_3 \\ -q_1 & -q_2 & -q_3 & q_0 \end{bmatrix}. \tag{6. 20}$$

The superscript $(\cdot)^{\times}$, is used to represent the skew-symmetric matrix obtained from a vector. If $\boldsymbol{i} = [i_x \quad i_y \quad i_z]^T$, then

$$\boldsymbol{i}^{\times} = \begin{bmatrix} 0 & -i_z & i_y \\ i_z & 0 & -i_x \\ -i_y & i_x & 0 \end{bmatrix}. \tag{6. 21}$$

In order for quaternions to be valid rotations, they need a quadratic norm constraint. In the presented filter this is achieved with the use of the rotation vector. The relationship between the quaternion error $\boldsymbol{\delta q}$ and the error rotation vector $\boldsymbol{\delta\phi}$ is given by

$$\boldsymbol{\delta q} = exp(\boldsymbol{\delta\phi}), \tag{6. 22}$$

where $exp(\cdot)$, is the quaternion exponential map that maps a rotation vector to a quaternion [83]:

$$exp(\boldsymbol{i}) = \begin{bmatrix} sin\left(\frac{1}{2}\|\boldsymbol{i}\|\right)\frac{\boldsymbol{i}}{\|\boldsymbol{i}\|} \\ cos\left(\frac{1}{2}\|\boldsymbol{i}\|\right) \end{bmatrix}. \tag{6. 23}$$

By using the state definition, the prediction model can now be derived.

6.4 Filter prediction model

This section discusses the prediction model needed by the filter in order to propagate the state from time step t_k to t_{k+1}. In order to do this, a set of continuous time differential equations need to be formulated for the specific state definition that will be used. Each of these equations will now be discussed separately.

Centre of body position

The rate of change in displacement with respect to time is defined as velocity, therefore the derivative of position is velocity. Using the symbols as defined in the state vector definition, the continuous time differential equation for the centre of the robot's body can be formulated as [2]:

$$\dot{\boldsymbol{r}} = \boldsymbol{v}. \tag{6. 24}$$

Centre of body velocity

The rate of change in velocity with respect to time is defined as absolute acceleration, therefore the derivative of velocity is absolute acceleration, $\boldsymbol{a}$. The continuous time differential equation for the velocity of the centre of the robot's body can be formulated as [2]:

$$\dot{\boldsymbol{v}} = \boldsymbol{a}. \tag{6. 25}$$

By using the IMU measurement for proper acceleration, $\tilde{\boldsymbol{f}}$, as defined by (5.23) and taking into consideration the relationship between the proper acceleration and the absolute acceleration as defined in (5.15), (6.25) can be rewritten as:

$$\dot{\boldsymbol{v}} = \boldsymbol{C}^T\boldsymbol{f} + \boldsymbol{g} = \boldsymbol{C}^T\left(\tilde{\boldsymbol{f}} - \boldsymbol{b}_f - \boldsymbol{w}_f\right) + \boldsymbol{g}, \tag{6. 26}$$

where $\boldsymbol{g}$ is the standard gravity vector as defined in Chapter 5.

Quaternion

The rate of change of a quaternion can be described by the relationship of the body coordinate frame, $\boldsymbol{B}$, moving with respect to the inertial coordinate frame, $\boldsymbol{I}$ [84]. The derivative is computed by the limit equation,

$${}^{B(t)}_{I}\dot{\bar{\boldsymbol{q}}}(t) = \lim_{\Delta t \to 0} \frac{1}{\Delta t}\left({}^{B(t+\Delta t)}_{I}\bar{\boldsymbol{q}} - {}^{B(t)}_{I}\bar{\boldsymbol{q}}\right). \tag{6. 27}$$

Expressing the quaternion ${}^{B(t+\Delta t)}_{I}\bar{\boldsymbol{q}}$, as a product of two quaternions, yields

$$ {}^{B(t+\Delta t)}_{I}\overline{\boldsymbol{q}} = {}^{B(t+\Delta t)}_{B(t)}\overline{\boldsymbol{q}} \otimes {}^{B(t)}_{I}\overline{\boldsymbol{q}}, \tag{6. 28} $$

where the quaternion ${}^{B(t+\Delta t)}_{B(t)}\overline{\boldsymbol{q}}$ describes the rotation of the body coordinate frame between time step t, and time step $t + \Delta t$. By describing ${}^{B(t+\Delta t)}_{B(t)}\overline{\boldsymbol{q}}$ in terms of a rotation angle, θ, and a axis of rotation, $\widehat{\boldsymbol{K}}$, yields

$$ {}^{B(t+\Delta t)}_{B(t)}\overline{\boldsymbol{q}} = \begin{bmatrix} \widehat{\boldsymbol{K}} sin\left(\frac{\theta}{2}\right) \\ cos\left(\frac{\theta}{2}\right) \end{bmatrix}. \tag{6. 29} $$

In the limit, as $\Delta t \to 0$, the angle of rotation can be defined as infinitesimal. Therefore, (6.29) can be approximated as

$$ {}^{B(t+\Delta t)}_{B(t)}\overline{\boldsymbol{q}} = \begin{bmatrix} \widehat{\boldsymbol{K}} sin\left(\frac{\theta}{2}\right) \\ cos\left(\frac{\theta}{2}\right) \end{bmatrix} \approx \begin{bmatrix} \widehat{\boldsymbol{K}} \cdot \left(\frac{\theta}{2}\right) \\ 1 \end{bmatrix} = \begin{bmatrix} \frac{1}{2} \cdot \boldsymbol{\delta\theta} \\ 1 \end{bmatrix}, \tag{6. 30} $$

where $\boldsymbol{\delta\theta}$ is a vector with the magnitude of the angle of the rotation and the direction of the axis of the rotation. Using this vector, the rotational velocity or angular rate, $\boldsymbol{\omega} = [\omega_x \quad \omega_y \quad \omega_z]^T$, can be defined as

$$ \boldsymbol{\omega} = \lim_{\Delta t \to 0} \frac{\boldsymbol{\delta\theta}}{\Delta t}. \tag{6. 31} $$

The derivative of the quaternion can now be derived as follows

$$ \begin{aligned} {}^{B(t)}_{I}\dot{\overline{\boldsymbol{q}}}(t) &= \lim_{\Delta t \to 0} \frac{1}{\Delta t} \left({}^{B(t+\Delta t)}_{I}\overline{\boldsymbol{q}} - {}^{B(t)}_{I}\overline{\boldsymbol{q}} \right), \\ &= \lim_{\Delta t \to 0} \frac{1}{\Delta t} \left({}^{B(t+\Delta t)}_{B(t)}\overline{\boldsymbol{q}} \otimes {}^{B(t)}_{I}\overline{\boldsymbol{q}} - \boldsymbol{q}_{\mathbb{I}} \otimes {}^{B(t)}_{I}\overline{\boldsymbol{q}} \right), \\ &\approx \lim_{\Delta t \to 0} \frac{1}{\Delta t} \left(\begin{bmatrix} \frac{1}{2} \cdot \boldsymbol{\delta\theta} \\ 1 \end{bmatrix} - \begin{bmatrix} 0 \\ 1 \end{bmatrix} \right) \otimes {}^{B(t)}_{I}\overline{\boldsymbol{q}}, \\ &= \frac{1}{2} \begin{bmatrix} \boldsymbol{\omega} \\ 0 \end{bmatrix} \otimes {}^{B(t)}_{I}\overline{\boldsymbol{q}}. \end{aligned} \tag{6. 32} $$

Therefore, the continuous time differential equation for the quaternion is defined as

$$ \dot{\boldsymbol{q}} = \frac{1}{2} \begin{bmatrix} \boldsymbol{\omega} \\ 0 \end{bmatrix} \otimes \boldsymbol{q} = \frac{1}{2} \, Q\left(\begin{bmatrix} \boldsymbol{\omega} \\ 0 \end{bmatrix} \right) \boldsymbol{q}, \tag{6. 33} $$

or [2],

$$\dot{\boldsymbol{q}} = \frac{1}{2}\,\boldsymbol{\Omega}(\boldsymbol{\omega})\boldsymbol{q}, \tag{6. 34}$$

where $\boldsymbol{\Omega}(\cdot)$ maps a vector to a 4×4 matrix when the product of a vector and a quaternion has to be calculated :

$$\boldsymbol{\Omega}(\boldsymbol{\omega}) = \begin{bmatrix} -\boldsymbol{\omega}^{\times} & \boldsymbol{\omega} \\ -\boldsymbol{\omega}^{T} & 0 \end{bmatrix} = \begin{bmatrix} 0 & \omega_z & -\omega_y & \omega_x \\ -\omega_z & 0 & \omega_x & \omega_y \\ \omega_y & -\omega_x & 0 & \omega_z \\ -\omega_x & -\omega_y & -\omega_z & 0 \end{bmatrix}. \tag{6. 35}$$

By taking into consideration the measurement model derived in (5.25) for the angular rate measured by the IMU, (6.34) can be rewritten as the continuous time differential equation for the state defined quaternion:

$$\dot{\boldsymbol{q}} = \frac{1}{2}\,\boldsymbol{\Omega}(\tilde{\boldsymbol{\omega}} - \boldsymbol{b}_{\omega} - \boldsymbol{w}_{\boldsymbol{\omega}})\boldsymbol{q}. \tag{6. 36}$$

Foot positions

For the foot positions, an assumption is made that they stay stationary. However, for the hexapod in order to handle a certain amount of foot slippage, a white noise term $\boldsymbol{w}_{p,i}$ with covariance parameter $\boldsymbol{Q}_{p,i}$ for $i \in \{1, \dots, 6\}$, is added to the absolute foot positions [2]:

$$\boldsymbol{Q}_{p,i} = \begin{bmatrix} w_{p,i,x} & 0 & 0 \\ 0 & w_{p,i,y} & 0 \\ 0 & 0 & w_{p,i,z} \end{bmatrix}. \tag{6. 37}$$

In order to turn the magnitude of this noise term in different directions relative to the hexapod's orientation, the noise term is described in the body coordinate frame $\boldsymbol{B}$. The continuous time differential equation for the foot positions can now be defined as:

$$\dot{\boldsymbol{p}}_i = \boldsymbol{C}^{T}\boldsymbol{w}_{p,i} \qquad \forall i \in \{1, \dots, 6\}. \tag{6. 38}$$

In order to handle intermittent contacts of the feet when stepping, the noise parameter of a certain foothold needs to be set to infinity when the specific foot has no ground contact. This is done to insure the old foothold position is dropped from the estimation process. The filter is therefore able to relocate and reset the corresponding position estimate when it regains ground contact.

IMU bias derivatives

The accelerometer and gyroscope bias terms, $\boldsymbol{b}_f$ and $\boldsymbol{b}_{\omega}$, and their corresponding derivatives that are represented by white Gaussian noise processes, were defined in Chapter 5. For convenience the continuous time differential acceleration and angular rate equations are given again as

$$\dot{\boldsymbol{b}}_f = \boldsymbol{w}_{bf}, \tag{6. 39}$$

$$\dot{\boldsymbol{b}}_\omega = \boldsymbol{w}_{b\omega}. \tag{6. 40}$$

Process noise vector

By combining all the noise terms as defined in Chapter 4, 5 and 6, the process noise vector for the state can now be defined as

$$\boldsymbol{w} = [\boldsymbol{0} \quad \boldsymbol{w}_f \quad \boldsymbol{w}_\omega \quad \boldsymbol{w}_{p,1} \quad \boldsymbol{w}_{p,2} \quad \boldsymbol{w}_{p,3} \quad \boldsymbol{w}_{p,4} \quad \boldsymbol{w}_{p,5} \quad \boldsymbol{w}_{p,6} \quad \boldsymbol{w}_{bf} \quad \boldsymbol{w}_{b\omega}]^T. \tag{6. 41}$$

6.5 Filter measurement model

This section discusses the filter measurement model needed by the update step of the EKF. This includes the foot position measurement model and the noise measurement model. Based on the derived kinematic measurement model, (4.30), and using the terms as specified in the joint position measurement model, (5.21), a transformed measurement quantity is introduced for each leg i [2]:

$$\tilde{\boldsymbol{s}}_i := \boldsymbol{kin}_i(\tilde{\boldsymbol{\theta}}) \tag{6. 42}$$

$$\approx \boldsymbol{kin}_i(\boldsymbol{\theta}) + \boldsymbol{J}_{kin,i}\boldsymbol{n}_\theta \tag{6. 43}$$

$$\approx \boldsymbol{s}_i - \boldsymbol{n}_{s,i} + \boldsymbol{J}_{kin,i}\boldsymbol{n}_\theta\,, \tag{6. 44}$$

where,

$$\boldsymbol{J}_{kin,i} := \frac{\partial \boldsymbol{kin}_i(\boldsymbol{\theta})}{\partial \boldsymbol{\theta}_i} \qquad i \in \{1, \dots, 6\}, \tag{6. 45}$$

is the Jacobian for leg i of the kinematics with respect to the joint angles. From (6.44), a new measurement noise quantity, $\boldsymbol{n}_i$, is defined that includes the linearised noise effect from the joint position sensors as well as the noise from the foothold positions:

$$\boldsymbol{n}_i = -\boldsymbol{n}_{s,i} + \boldsymbol{J}_{kin,i}\boldsymbol{n}_\theta. \tag{6. 46}$$

The covariance matrix $\boldsymbol{R}_i$ is defined for the measurement noise quantity $\boldsymbol{n}_i$:

$$\boldsymbol{R}_i = \boldsymbol{R}_s + \boldsymbol{J}_{kin,i}\boldsymbol{R}_\theta\boldsymbol{J}_{kin,i}^T. \tag{6. 47}$$

The measurement $\tilde{\boldsymbol{s}}_i$ defining the position of the contact of foot i with respect to the body coordinate frame $\boldsymbol{B}$, can also be expressed as the absolute position of the foot contact $\boldsymbol{p}_i$ minus the absolute

position of the centre of the hexapod robot $\boldsymbol{r}$ rotated into the body coordinate frame $\boldsymbol{B}$. This expression of $\tilde{\boldsymbol{s}}_i$ is formulated as:

$$\tilde{\boldsymbol{s}}_{\boldsymbol{i}} = \boldsymbol{C}(\boldsymbol{p}_i - \boldsymbol{r}) + \boldsymbol{n}_i. \tag{6. 48}$$

We are now able to perform the state estimation for the nonlinear system defined by linearising, at each time step, the models derived around the current state estimate and applying the standard Kalman filter equations.

6.6 Extended Kalman filter equations

This section discusses the Extended Kalman filter equations. Firstly, the filter convention is stated. Secondly, the prediction step is discussed, where the continuous time differential equations are discretised and linearised, the error dynamic matrix and the noise covariance matrix are derived, and the filter prediction equations are formulated. Thirdly, the update step is discussed, where the measurement residual is formulated, the foot position measurement model is linearised, the measurement Jacobian and noise matrices are derived, and the filter update equations are formulated.

6.6.1 Filtering convention

The following standard filtering convention is used for the Extended Kalman filter:

- The current time step is indicated with the subscript k, and the next time step is indicated with the subscript $k + 1$.
- At time step k, $\hat{\boldsymbol{x}}_k^-$ represents the *a priori* state estimate.
- At time step k, $\hat{\boldsymbol{x}}_k^+$ represents the *a posteriori* state estimate

6.6.2 Prediction step

In the prediction step, the EKF produces the *a priori* estimates by propagating the expected value of the state as well as the error covariance. For the discretisation and the linearisation of the prediction and measurement models, Bloesch et al. [2] introduce the following auxiliary quantity:

$$\boldsymbol{\Gamma}_n \coloneqq \sum_{i=0}^{\infty} \frac{\Delta t^{i+n}}{(i+n)!}\, \boldsymbol{\omega}^{\times i}. \tag{6. 49}$$

For $n = 0$, it yields

$$\mathbf{\Gamma}_0 \coloneqq \sum_{i=0}^{\infty} \frac{(\Delta t\boldsymbol{\omega}^{\times})^i}{i!} = \mathbb{I}_3 + (\Delta t\boldsymbol{\omega}^{\times}) + \frac{(\Delta t\boldsymbol{\omega}^{\times})^2}{2!} + \frac{(\Delta t\boldsymbol{\omega}^{\times})^3}{3!} + \cdots, \tag{6. 50}$$

where,

$$\Delta t\boldsymbol{\omega}^{\times} = \begin{bmatrix} 0 & -\Delta t\omega_z & \Delta t\omega_y \\ \Delta t\omega_z & 0 & -\Delta t\omega_x \\ -\Delta t\omega_y & \Delta t\omega_x & 0 \end{bmatrix}, \tag{6. 51}$$

is a skew-symmetric matrix. Let the rotation angle, θ, about a fixed axis be specified as

$$\theta = \sqrt{\left((\Delta t\omega_x)^2 + \left(\Delta t\omega_y\right)^2 + (\Delta t\omega_z)^2\right)}. \tag{6. 52}$$

Then we have the well-known Rodrigues' formula [85]:

$$\exp(\Delta t\boldsymbol{\omega}^{\times}) = \mathbb{I}_{3\times 3} + \frac{sin\theta}{\theta}(\Delta t\boldsymbol{\omega}^{\times}) + \frac{1 - cos\theta}{\theta^2}(\Delta t\boldsymbol{\omega}^{\times})^2. \tag{6. 53}$$

Therefore,

$$\mathbf{\Gamma}_0 \coloneqq \exp(\Delta t\boldsymbol{\omega}^{\times}), \tag{6. 54}$$

and represents the incremental rotation matrix when an arbitrary coordinate frame with a rotation rate of $-\boldsymbol{\omega}$ is rotated for Δt seconds.

Given a quaternion, $\boldsymbol{q}$, its corresponding rotational matrix, $\boldsymbol{C}$, can be determined with (6.15). Rewriting (6.15) by isolating the scalar and vector components of the quaternion, results in

$$\boldsymbol{C} = [2q_0^2 - 1]\mathbb{I} - 2q_0\boldsymbol{q}_{1:3}^{\times} + 2\boldsymbol{q}_{1:3}\boldsymbol{q}_{1:3}^{T}. \tag{6. 55}$$

Equation (6.55) can be seen as equivalent to Rodrigues' rotational formula when we evaluate it using the quaternion exponential map

$$exp(\boldsymbol{\omega}) = \begin{bmatrix} sin\left(\frac{1}{2}\|\boldsymbol{\omega}\|\right)\frac{\boldsymbol{\omega}}{\|\boldsymbol{\omega}\|} \\ cos\left(\frac{1}{2}\|\boldsymbol{\omega}\|\right) \end{bmatrix}. \tag{6. 56}$$

In (6.56), a quaternion is represented as a rotation of $\|\boldsymbol{\omega}\|$ about an axis $\boldsymbol{\omega}/\|\boldsymbol{\omega}\|$. By defining $\boldsymbol{\delta\phi}$, from the state error vector as an infinitesimal rotation, we can rewrite (6.22) as

$$\boldsymbol{\delta q} = exp(\boldsymbol{\delta\phi}) \approx \begin{bmatrix} \frac{1}{2}\boldsymbol{\delta\phi} \\ 1 \end{bmatrix}, \tag{6. 57}$$

a first-order approximation of an incremental quaternion. Substituting (6.57) into (6.55), the first-order approximation for the rotation matrix, $\boldsymbol{C}_{\delta q}$, is defined as

$$\boldsymbol{C}_{\delta q} \approx \mathbb{I} - \boldsymbol{\delta\phi}^{\times}. \tag{6.58}$$

The first-order approximation of the exponential map for specifically rotation matrices, can therefore also be formulated as

$$exp(\boldsymbol{\delta\phi}^{\times}) = \sum_{i=0}^{\infty} \frac{(-\boldsymbol{\delta\phi}^{\times})^{i}}{i!} \approx \mathbb{I} - \boldsymbol{\delta\phi}^{\times}. \tag{6.59}$$

6.6.2.1 Discretised prediction equations

In this section we transform the continuous time differential equations derived in the prediction model into their discrete difference counterparts. The discretisation is done with the assumption of zero-order hold for the measured quantities from the IMU, $\tilde{\boldsymbol{f}}_k$ and $\tilde{\boldsymbol{\omega}}_k$. The effect of the incremental rotation is also neglected. For the position of the centre of the robot, (6.24)-(6.26) can be used to produce the following equation:

$$\ddot{\boldsymbol{r}} = \boldsymbol{a} = \boldsymbol{C}^{T}\boldsymbol{f} + \boldsymbol{g} = \boldsymbol{C}^{T}\left(\tilde{\boldsymbol{f}} - \boldsymbol{b}_f - \boldsymbol{w}_f\right) + \boldsymbol{g}. \tag{6.60}$$

We can discretise (6.60) to derive the following discrete difference equation for the position of the centre of the robot:

$$\hat{\boldsymbol{r}}_{k+1}^{-} = \hat{\boldsymbol{r}}_k^{+} + \Delta t\hat{\boldsymbol{v}}_k^{+} + \frac{\Delta t^2}{2}\hat{\boldsymbol{a}}_k^{+} = \hat{\boldsymbol{r}}_k^{+} + \Delta t\hat{\boldsymbol{v}}_k^{+} + \frac{\Delta t^2}{2}\left(\hat{\boldsymbol{C}}_k^{+T}\hat{\boldsymbol{f}}_k + \boldsymbol{g}\right). \tag{6.61}$$

This second-order discretisation for the position of the centre of the body is used to incorporate the IMU acceleration. In (6.61), $\hat{\boldsymbol{f}}_k$, represent the expected value of the measured acceleration and is calculated as

$$\hat{\boldsymbol{f}}_k = \tilde{\boldsymbol{f}}_k - \hat{\boldsymbol{b}}_{f,k}^{+}. \tag{6.62}$$

Equation (6.26) is discretised to produce the following discrete difference equation for the velocity of the centre of the robot:

$$\hat{\boldsymbol{v}}_{k+1}^{-} = \hat{\boldsymbol{v}}_k^{+} + \Delta t\hat{\boldsymbol{a}}_k = \hat{\boldsymbol{v}}_k^{+} + \Delta t\left(\hat{\boldsymbol{C}}_k^{+T}\hat{\boldsymbol{f}}_k + \boldsymbol{g}\right). \tag{6.63}$$

Let $\Delta t\hat{\boldsymbol{\omega}}_k$ represent the integral of the IMU body coordinate frame angular rate measurement between two subsequent time steps, then the discrete time difference equation for the quaternion can be given by

$$\hat{\boldsymbol{q}}_{k+1}^{-} = exp(\Delta t \hat{\boldsymbol{\omega}}_k) \otimes \hat{\boldsymbol{q}}_k^{+}, \tag{6. 64}$$

where $exp(\cdot)$ is the map as defined in (6.23), and, $\hat{\boldsymbol{\omega}}_k$, denotes the expected value of the measured angular rate, calculated as

$$\hat{\boldsymbol{\omega}}_k = \tilde{\boldsymbol{\omega}}_k - \hat{\boldsymbol{b}}_{\omega,k}^{+}. \tag{6. 65}$$

An assumption is made that the foot positions of the robot stay the same from one time step to the next while the feet has ground contact. Therefore, the discrete time difference equation for the feet positions of the hexapod can be defined as:

$$\hat{\boldsymbol{p}}_{i,k+1}^{-} = \hat{\boldsymbol{p}}_{i,k}^{+} \qquad \forall i \in \{1, \dots, 6\}. \tag{6. 66}$$

The discrete difference acceleration bias is given by

$$\hat{\boldsymbol{b}}_{f,k+1}^{-} = \hat{\boldsymbol{b}}_{f,k}^{+}, \tag{6. 67}$$

and the discrete difference angular rate bias is given by

$$\hat{\boldsymbol{b}}_{\omega,k+1}^{-} = \hat{\boldsymbol{b}}_{\omega,k}^{+}. \tag{6. 68}$$

6.6.2.2 Linear differential equations

In order to propagate the state estimate covariance matrix through the state dynamics, linearisation of the prediction model equations is needed. The linearised equations will describe the error dynamics and are derived analytically by expanding the filter states about their expected values with the use of first-order Taylor series approximations.

Centre of body position

For the linearisation of the continuous time differential position equation, (6.24), we let

$$\boldsymbol{r} = \bar{\boldsymbol{r}} + \boldsymbol{\delta r}, \tag{6. 69}$$

and

$$\boldsymbol{v} = \bar{\boldsymbol{v}} + \boldsymbol{\delta v}. \tag{6. 70}$$

Substituting (6.69) and (6.70) into (6.24), gives

$$\dot{\boldsymbol{r}} = \frac{d}{dt}[\bar{\boldsymbol{r}} + \boldsymbol{\delta r}] = \bar{\boldsymbol{v}} + \boldsymbol{\delta v}. \tag{6. 71}$$

From (6.71), it follows that

$$\dot{\bar{\boldsymbol{r}}} + \dot{\boldsymbol{\delta r}} = \bar{\boldsymbol{v}} + \boldsymbol{\delta v}. \tag{6. 72}$$

By evaluating (6.72) in the context of (6.24), we know that

$$\dot{\bar{\boldsymbol{r}}} = \bar{\boldsymbol{v}}, \tag{6. 73}$$

therefore,

$$\dot{\boldsymbol{\delta r}} = \boldsymbol{\delta v} \tag{6. 74}$$

Centre of body velocity

For the linearisation of the continuous time differential velocity equation, (6.26), we make use of (6.70) and let

$$\boldsymbol{b}_f \approx \bar{\boldsymbol{b}}_f + \boldsymbol{\delta b}_f. \tag{6. 75}$$

Using the first-order approximation derived in (6.58), the matrix form of the first order expansion of $\boldsymbol{q}$ about a nominal quaternion, $\bar{\boldsymbol{q}}$ is given as

$$\boldsymbol{C}_{\delta q \otimes \bar{q}} = \boldsymbol{C}_{\delta q}\boldsymbol{C}_{\bar{q}} = [\mathbb{I} - \boldsymbol{\delta\phi}^{\times}]\bar{\boldsymbol{C}}\,, \tag{6. 76}$$

where $\boldsymbol{C}_{\delta q \otimes \bar{q}}$, is the rotation matrix for a quaternion determined by the quaternion multiplication $\boldsymbol{\delta q} \otimes \bar{\boldsymbol{q}}$, $\boldsymbol{C}_{\delta q}$, is the rotation matrix for $\boldsymbol{\delta q}$, and $\boldsymbol{C}_{\bar{q}} = \bar{\boldsymbol{C}}$, is the rotation matrix for $\bar{\boldsymbol{q}}$.

Equation (6.26) can now be rewritten as

$$\dot{\boldsymbol{v}} = \frac{d}{dt}\,[\bar{\boldsymbol{v}} + \boldsymbol{\delta v}] = \bar{\boldsymbol{C}}^T[\mathbb{I} + \boldsymbol{\delta\phi}^{\times}]\big[\tilde{\boldsymbol{f}} - \big(\bar{\boldsymbol{b}}_f + \boldsymbol{\delta b}_f\big) - \boldsymbol{w}_f\big] + \boldsymbol{g}. \tag{6. 77}$$

As in [86], we define

$$\bar{\boldsymbol{f}} = \tilde{\boldsymbol{f}} - \bar{\boldsymbol{b}}_f, \tag{6. 78}$$

as the “large-signal” and

$$\boldsymbol{\delta f} = -\boldsymbol{\delta b}_f - \boldsymbol{w}_f \tag{6. 79}$$

as the “small-signal” accelerations. Substituting (6.78) and (6.79) into (6.77), yields

$$\dot{\bar{\boldsymbol{v}}} + \dot{\boldsymbol{\delta v}} = \bar{\boldsymbol{C}}^T[\mathbb{I} + \boldsymbol{\delta\phi}^{\times}]\big[\bar{\boldsymbol{f}} + \boldsymbol{\delta f}\big] + \boldsymbol{g}, \tag{6. 80}$$

$$\dot{\bar{\boldsymbol{v}}} + \dot{\boldsymbol{\delta v}} = \bar{\boldsymbol{C}}^T\bar{\boldsymbol{f}} + \bar{\boldsymbol{C}}^T\boldsymbol{\delta f} + \bar{\boldsymbol{C}}^T\boldsymbol{\delta\phi}^{\times}\bar{\boldsymbol{f}} + \bar{\boldsymbol{C}}^T\boldsymbol{\delta\phi}^{\times}\boldsymbol{\delta f} + \boldsymbol{g}. \tag{6. 81}$$

By evaluating (6.81) in the context of (6.26), we know that

$$\dot{\bar{\boldsymbol{v}}} = \bar{\boldsymbol{C}}^T \bar{\boldsymbol{f}} + \boldsymbol{g}, \tag{6. 82}$$

therefore,

$$\dot{\boldsymbol{\delta v}} = \bar{\boldsymbol{C}}^T \boldsymbol{\delta f} + \bar{\boldsymbol{C}}^T \boldsymbol{\delta\phi}^{\times} \bar{\boldsymbol{f}} + \bar{\boldsymbol{C}}^T \boldsymbol{\delta\phi}^{\times} \boldsymbol{\delta f}. \tag{6. 83}$$

$\bar{\boldsymbol{C}}^T \boldsymbol{\delta\phi}^{\times} \boldsymbol{\delta f}$, is the product of two small vectors and can therefore be neglected, resulting in

$$\dot{\boldsymbol{\delta v}} = \bar{\boldsymbol{C}}^T \boldsymbol{\delta f} + \bar{\boldsymbol{C}}^T \boldsymbol{\delta\phi}^{\times} \bar{\boldsymbol{f}}. \tag{6. 84}$$

Substituting (6.79) into (6.84), results in the linear differential velocity equation given by Bloesch et al.[2]:

$$\dot{\boldsymbol{\delta v}} = -\boldsymbol{C}^T \boldsymbol{f}^{\times} \boldsymbol{\delta\phi} - \boldsymbol{C}^T \boldsymbol{\delta b}_f - \boldsymbol{C}^T \boldsymbol{w}_f \tag{6. 85}$$

Quaternion

For the linearisation of the continuous time differential quaternion equation, (6.36), we make use of (6.18) to define a deviation $\boldsymbol{\delta q}$ from the expected value $\bar{\boldsymbol{q}}$ of the pose $\boldsymbol{q}$ by

$$\boldsymbol{q} = \boldsymbol{\delta q} \otimes \bar{\boldsymbol{q}}\,. \tag{6. 86}$$

Letting,

$$\boldsymbol{b}_{\omega} \approx \bar{\boldsymbol{b}}_{\omega} + \boldsymbol{\delta b}_{\omega} \tag{6. 87}$$

Equation (6.36) can be rewritten as [84]

$$\dot{\boldsymbol{q}} = \frac{d}{dt}[\boldsymbol{\delta q} \otimes \bar{\boldsymbol{q}}] = \frac{1}{2}\begin{bmatrix} \tilde{\boldsymbol{\omega}} - (\bar{\boldsymbol{b}}_{\omega} + \boldsymbol{\delta b}_{\omega}) - \boldsymbol{w}_{\omega} \\ 0 \end{bmatrix} \otimes \boldsymbol{q}, \tag{6. 88}$$

$$\frac{1}{2}\begin{bmatrix} \tilde{\boldsymbol{\omega}} - (\bar{\boldsymbol{b}}_{\omega} + \boldsymbol{\delta b}_{\omega}) - \boldsymbol{w}_{\omega} \\ 0 \end{bmatrix} \otimes \boldsymbol{q} = \dot{\boldsymbol{\delta q}} \otimes \bar{\boldsymbol{q}} + \boldsymbol{\delta q} \otimes \dot{\bar{\boldsymbol{q}}}. \tag{6. 89}$$

It is know that

$$\dot{\boldsymbol{q}} = \frac{1}{2}\begin{bmatrix} \tilde{\boldsymbol{\omega}} - \bar{\boldsymbol{b}}_{\omega} \\ 0 \end{bmatrix} \otimes \boldsymbol{q}. \tag{6. 90}$$

Substituting (6.90) into (6.89) ,yields

$$\frac{1}{2}\begin{bmatrix} \tilde{\boldsymbol{\omega}} - (\bar{\boldsymbol{b}}_{\omega} + \boldsymbol{\delta b}_{\omega}) - \boldsymbol{w}_{\omega} \\ 0 \end{bmatrix} \otimes \boldsymbol{q} = \dot{\boldsymbol{\delta q}} \otimes \bar{\boldsymbol{q}} + \boldsymbol{\delta q} \otimes \left[\frac{1}{2}\begin{bmatrix} \tilde{\boldsymbol{\omega}} - \bar{\boldsymbol{b}}_{\omega} \\ 0 \end{bmatrix} \otimes \bar{\boldsymbol{q}}\right]. \tag{6. 91}$$

Rearranging (6.86) leads to

$$\boldsymbol{\delta q} = \boldsymbol{q} \otimes \bar{\boldsymbol{q}}^{-1}\,. \tag{6. 92}$$

Simplifying (6.91), by multiplying with $\bar{\boldsymbol{q}}^{-1}$ throughout the equation and using (6.92), yields

$$\frac{1}{2}\begin{bmatrix}\tilde{\boldsymbol{\omega}} - (\bar{\boldsymbol{b}}_\omega + \boldsymbol{\delta b}_\omega) - \boldsymbol{w}_\omega \\ 0\end{bmatrix} \otimes \boldsymbol{\delta q} = \dot{\boldsymbol{\delta q}} + \boldsymbol{\delta q} \otimes \left[\frac{1}{2}\begin{bmatrix}\tilde{\boldsymbol{\omega}} - \bar{\boldsymbol{b}}_\omega \\ 0\end{bmatrix}\right], \tag{6. 93}$$

where solving (6.93) for $\dot{\boldsymbol{\delta q}}$ gives

$$\dot{\boldsymbol{\delta q}} = \frac{1}{2}\begin{bmatrix}\tilde{\boldsymbol{\omega}} - (\bar{\boldsymbol{b}}_\omega + \boldsymbol{\delta b}_\omega) - \boldsymbol{w}_\omega \\ 0\end{bmatrix} \otimes \boldsymbol{\delta q} - \boldsymbol{\delta q} \otimes \left[\frac{1}{2}\begin{bmatrix}\tilde{\boldsymbol{\omega}} - \bar{\boldsymbol{b}}_\omega \\ 0\end{bmatrix}\right], \tag{6. 94}$$

By splitting the first quaternion term on the right into two pure quaternions, such that

$$\frac{1}{2}\begin{bmatrix}\tilde{\boldsymbol{\omega}} - (\bar{\boldsymbol{b}}_\omega + \boldsymbol{\delta b}_\omega) - \boldsymbol{w}_\omega \\ 0\end{bmatrix} \otimes \boldsymbol{\delta q} = \frac{1}{2}\begin{bmatrix}\tilde{\boldsymbol{\omega}} - \bar{\boldsymbol{b}}_\omega \\ 0\end{bmatrix} \otimes \boldsymbol{\delta q} + \frac{1}{2}\begin{bmatrix}-\boldsymbol{\delta b}_\omega - \boldsymbol{w}_\omega \\ 0\end{bmatrix} \otimes \boldsymbol{\delta q}, \tag{6. 95}$$

we can rewrite (6.94) as

$$\dot{\boldsymbol{\delta q}} = \frac{1}{2}\begin{bmatrix}\tilde{\boldsymbol{\omega}} - \bar{\boldsymbol{b}}_\omega \\ 0\end{bmatrix} \otimes \boldsymbol{\delta q} - \boldsymbol{\delta q} \otimes \left[\frac{1}{2}\begin{bmatrix}\tilde{\boldsymbol{\omega}} - \bar{\boldsymbol{b}}_\omega \\ 0\end{bmatrix}\right] + \frac{1}{2}\begin{bmatrix}-\boldsymbol{\delta b}_\omega - \boldsymbol{w}_\omega \\ 0\end{bmatrix} \otimes \boldsymbol{\delta q}. \tag{6. 96}$$

Let the quaternion $\boldsymbol{\delta q}$ correspond to the small rotation $\boldsymbol{\delta\phi}$, so that we write

$$\boldsymbol{\delta q} \approx \begin{bmatrix}\frac{1}{2}\boldsymbol{\delta\phi} \\ 1\end{bmatrix}, \tag{6. 97}$$

and thus

$$\dot{\boldsymbol{\delta q}} \approx \begin{bmatrix}\frac{1}{2}\dot{\boldsymbol{\delta\phi}} \\ 0\end{bmatrix}. \tag{6. 98}$$

Using (6.97) and (6.98) we can rewrite (6.96) as

$$\begin{bmatrix}\frac{1}{2}\dot{\boldsymbol{\delta\phi}} \\ 0\end{bmatrix} = \tag{6. 99}$$

$$\frac{1}{2}\begin{bmatrix}\tilde{\boldsymbol{\omega}} - \bar{\boldsymbol{b}}_\omega \\ 0\end{bmatrix} \otimes \begin{bmatrix}\frac{1}{2}\boldsymbol{\delta\phi} \\ 1\end{bmatrix} - \begin{bmatrix}\frac{1}{2}\boldsymbol{\delta\phi} \\ 1\end{bmatrix} \otimes \left[\frac{1}{2}\begin{bmatrix}\tilde{\boldsymbol{\omega}} - \bar{\boldsymbol{b}}_\omega \\ 0\end{bmatrix}\right] + \frac{1}{2}\begin{bmatrix}-\boldsymbol{\delta b}_\omega - \boldsymbol{w}_\omega \\ 0\end{bmatrix} \otimes \begin{bmatrix}\frac{1}{2}\boldsymbol{\delta\phi} \\ 1\end{bmatrix}.$$

Let

$$\hat{\boldsymbol{\omega}} = \tilde{\boldsymbol{\omega}} - \bar{\boldsymbol{b}}_\omega. \tag{6. 100}$$

Writing the quaternion products in (6.99) as matrix-vector products as defined in (6.20), yields

$$\begin{bmatrix}\frac{1}{2}\dot{\boldsymbol{\delta\phi}}\\0\end{bmatrix}=\frac{1}{2}\left[\begin{bmatrix}-\hat{\boldsymbol{\omega}}^{\times} & \hat{\boldsymbol{\omega}}\\-\hat{\boldsymbol{\omega}}^{T} & 0\end{bmatrix}-\begin{bmatrix}\hat{\boldsymbol{\omega}}^{\times} & \hat{\boldsymbol{\omega}}\\-\hat{\boldsymbol{\omega}}^{T} & 0\end{bmatrix}\right]\begin{bmatrix}\frac{1}{2}\boldsymbol{\delta\phi}\\1\end{bmatrix}-\frac{1}{2}\begin{bmatrix}\boldsymbol{\delta b}_{\omega}+\boldsymbol{w}_{\omega}\\0\end{bmatrix}\otimes\begin{bmatrix}\frac{1}{2}\boldsymbol{\delta\phi}\\1\end{bmatrix}, \tag{6.101}$$

$$=\frac{1}{2}\begin{bmatrix}-2\hat{\boldsymbol{\omega}}^{\times} & \mathbf{0}_{3\times1}\\\mathbf{0}_{1\times3} & 0\end{bmatrix}\begin{bmatrix}\frac{1}{2}\boldsymbol{\delta\phi}\\1\end{bmatrix}-\frac{1}{2}\begin{bmatrix}\boldsymbol{\delta b}_{\omega}+\boldsymbol{w}_{\omega}\\0\end{bmatrix}\otimes\begin{bmatrix}\frac{1}{2}\boldsymbol{\delta\phi}\\1\end{bmatrix}, \tag{6.102}$$

$$=\frac{1}{2}\begin{bmatrix}-2\hat{\boldsymbol{\omega}}^{\times} & \mathbf{0}_{3\times1}\\\mathbf{0}_{1\times3} & 0\end{bmatrix}\begin{bmatrix}\frac{1}{2}\boldsymbol{\delta\phi}\\1\end{bmatrix}-\frac{1}{2}\begin{bmatrix}-[\boldsymbol{\delta b}_{\omega}+\boldsymbol{w}_{\omega}]^{\times} & \boldsymbol{\delta b}_{\omega}+\boldsymbol{w}_{\omega}\\-[\boldsymbol{\delta b}_{\omega}+\boldsymbol{w}_{\omega}]^{T} & 0\end{bmatrix}\begin{bmatrix}\frac{1}{2}\boldsymbol{\delta\phi}\\1\end{bmatrix}, \tag{6.103}$$

$$=\frac{1}{2}\begin{bmatrix}-2\hat{\boldsymbol{\omega}}^{\times} & \mathbf{0}_{3\times1}\\\mathbf{0}_{1\times3} & 0\end{bmatrix}\begin{bmatrix}\frac{1}{2}\boldsymbol{\delta\phi}\\1\end{bmatrix}-\frac{1}{2}\begin{bmatrix}\boldsymbol{\delta b}_{\omega}+\boldsymbol{w}_{\omega}\\0\end{bmatrix}. \tag{6.104}$$

To produce (6.104), the products of deviations as well as products of noise with deviations were neglected as they are small quantities. Multiplying out (6.104), produces the following two equations:

$$\frac{1}{2}\dot{\boldsymbol{\delta\phi}}=-\frac{1}{2}\boldsymbol{\omega}^{\times}\boldsymbol{\delta\phi}-\frac{1}{2}[\boldsymbol{\delta b}_{\omega}+\boldsymbol{w}_{\omega}], \tag{6.105}$$

$$0=0, \tag{6.106}$$

where (6.105) results in the linear differential equation corresponding to Bloesch et al.[2]:

$$\dot{\boldsymbol{\delta\phi}}=-\boldsymbol{\omega}^{\times}\boldsymbol{\delta\phi}-\boldsymbol{\delta b}_{\omega}-\boldsymbol{w}_{\omega}. \tag{6.107}$$

Foot Position

For the linearisation of the continuous time differential foot position equation, (6.38), let

$$\boldsymbol{p}\approx\overline{\boldsymbol{p}}+\boldsymbol{\delta p}. \tag{6.108}$$

Rewriting the matrix form of the first order expansion of $\boldsymbol{q}$ about a nominal quaternion, $\overline{\boldsymbol{q}}$ is given in (6.76), for $\boldsymbol{C}^{T}$ yields

$$\boldsymbol{C}^{T}\approx\overline{\boldsymbol{C}}^{T}[\mathbb{I}+\boldsymbol{\delta\phi}^{\times}]. \tag{6.109}$$

Equation (6.38) can now be written as

$$\dot{\boldsymbol{p}}=\frac{d}{dt}[\overline{\boldsymbol{p}}+\boldsymbol{\delta p}]=\overline{\boldsymbol{C}}^{T}[\mathbb{I}+\boldsymbol{\delta\phi}^{\times}]\boldsymbol{w}_{p}, \tag{6.110}$$

and simplified to

$$\dot{\overline{\boldsymbol{p}}}+\dot{\boldsymbol{\delta p}}=\overline{\boldsymbol{C}}^{T}\boldsymbol{w}_{p}+\overline{\boldsymbol{C}}^{T}\boldsymbol{\delta\phi}^{\times}\boldsymbol{w}_{p}. \tag{6.111}$$

It is known that

$$\dot{\bar{\boldsymbol{p}}} = E[\dot{\boldsymbol{p}}] = E\left[\boldsymbol{C}^T \boldsymbol{w}_p\right] = E\left[\boldsymbol{w}_p\right] = 0, \tag{6. 112}$$

since $\boldsymbol{w}_p$ is zero-mean and $\boldsymbol{C}$ doesn't change the statistics of $\boldsymbol{w}_p$. Where, $E[X]$, is the expected value for X. Neglecting the term, $\overline{\boldsymbol{C}}^T \boldsymbol{\delta\phi}^{\times} \boldsymbol{w}_p$, in (6.111) since it is the cross product of a state deviation and a noise vector resulting in a very small quantity, the linear differential equation for the foot position is

$$\dot{\boldsymbol{\delta p}}_i = \boldsymbol{C}^T \boldsymbol{w}_{p,i} \qquad \forall i \in \{1, \dots, 6\}, \tag{6. 113}$$

corresponding to Bloesch et al.[2].

Accelerometer bias

For the linearisation of the continuous time differential accelerometer bias equation, (6.40), we let

$$\boldsymbol{b}_f \approx \bar{\boldsymbol{b}}_f + \boldsymbol{\delta b}_f, \tag{6. 114}$$

and rewrite (6.40) as

$$\dot{\boldsymbol{b}}_f = \frac{d}{dt}\left[\bar{\boldsymbol{b}}_f + \boldsymbol{\delta b}_f\right] = \boldsymbol{w}_{bf}. \tag{6. 115}$$

From (6.115), it follows that

$$\dot{\bar{\boldsymbol{b}}}_f + \dot{\boldsymbol{\delta b}}_f = \boldsymbol{w}_{bf}. \tag{6. 116}$$

Because $\boldsymbol{w}_{bf}$ is zero mean,

$$\dot{\bar{\boldsymbol{b}}}_f = E\left[\dot{\boldsymbol{b}}_f\right] = E\left[\boldsymbol{w}_{bf}\right] = 0, \tag{6. 117}$$

and therefore

$$\dot{\boldsymbol{\delta b}}_f = \boldsymbol{w}_{bf} \tag{6. 118}$$

Gyroscope bias

For the linearisation of the continuous time differential gyroscope bias equation, (6.42), we let

$$\boldsymbol{b}_\omega \approx \bar{\boldsymbol{b}}_\omega + \boldsymbol{\delta b}_\omega. \tag{6. 119}$$

By substituting (6.119) into (6.42), it follows that

$$\dot{\boldsymbol{b}}_\omega = \frac{d}{dt}\left[\bar{\boldsymbol{b}}_\omega + \boldsymbol{\delta b}_\omega\right] = \boldsymbol{w}_{b\omega}. \tag{6. 120}$$

From (6.120), it follows that

$$\dot{\bar{\boldsymbol{b}}}_{\omega} + \dot{\boldsymbol{\delta b}}_{\omega} = \boldsymbol{w}_{b\omega}. \tag{6. 121}$$

We know that

$$\dot{\bar{\boldsymbol{b}}}_{\omega} = E\left[\dot{\boldsymbol{b}}_{\omega}\right] = E[\boldsymbol{w}_{b\omega}] = 0, \tag{6. 122}$$

Since $\boldsymbol{w}_{b\omega}$ is zero mean, and therefore

$$\dot{\boldsymbol{\delta b}}_{\omega} = \boldsymbol{w}_{b\omega} \tag{6. 123}$$

6.6.2.3 Continuous, linear model

By using the state error vector, $\boldsymbol{\delta x}$, and the process noise vector, $\boldsymbol{w}$, the linearised system as defined by the linearised differential equations can now be written in state-space form as

$$\dot{\boldsymbol{\delta x}} = \boldsymbol{F}_c \boldsymbol{\delta x} + \boldsymbol{L}_c \boldsymbol{w}, \tag{6. 124}$$

where,

$$\boldsymbol{F}_c = \begin{bmatrix} 0 & \mathbb{I} & 0 & 0 & 0 & 0 & 0 & 0 & 0 & 0 & 0 \\ 0 & 0 & -\boldsymbol{C}^T\hat{\boldsymbol{f}}^{\times} & 0 & 0 & 0 & 0 & 0 & 0 & -\boldsymbol{C}^T & 0 \\ 0 & 0 & -\boldsymbol{\omega}^{\times} & 0 & 0 & 0 & 0 & 0 & 0 & 0 & -\mathbb{I} \\ 0 & 0 & 0 & 0 & 0 & 0 & 0 & 0 & 0 & 0 & 0 \\ 0 & 0 & 0 & 0 & 0 & 0 & 0 & 0 & 0 & 0 & 0 \\ 0 & 0 & 0 & 0 & 0 & 0 & 0 & 0 & 0 & 0 & 0 \\ 0 & 0 & 0 & 0 & 0 & 0 & 0 & 0 & 0 & 0 & 0 \\ 0 & 0 & 0 & 0 & 0 & 0 & 0 & 0 & 0 & 0 & 0 \\ 0 & 0 & 0 & 0 & 0 & 0 & 0 & 0 & 0 & 0 & 0 \\ 0 & 0 & 0 & 0 & 0 & 0 & 0 & 0 & 0 & 0 & 0 \\ 0 & 0 & 0 & 0 & 0 & 0 & 0 & 0 & 0 & 0 & 0 \end{bmatrix}, \tag{6. 125}$$

is prediction Jacobian or continuous linearised error dynamics matrix, as defined in (6.5) and,

$$\boldsymbol{L}_c = \begin{bmatrix} 0 & 0 & 0 & 0 & 0 & 0 & 0 & 0 & 0 & 0 & 0 \\ 0 & -\boldsymbol{C}^T & 0 & 0 & 0 & 0 & 0 & 0 & 0 & 0 & 0 \\ 0 & 0 & -\mathbb{I} & 0 & 0 & 0 & 0 & 0 & 0 & 0 & 0 \\ 0 & 0 & 0 & \boldsymbol{C}^T & 0 & 0 & 0 & 0 & 0 & 0 & 0 \\ 0 & 0 & 0 & 0 & \boldsymbol{C}^T & 0 & 0 & 0 & 0 & 0 & 0 \\ 0 & 0 & 0 & 0 & 0 & \boldsymbol{C}^T & 0 & 0 & 0 & 0 & 0 \\ 0 & 0 & 0 & 0 & 0 & 0 & \boldsymbol{C}^T & 0 & 0 & 0 & 0 \\ 0 & 0 & 0 & 0 & 0 & 0 & 0 & \boldsymbol{C}^T & 0 & 0 & 0 \\ 0 & 0 & 0 & 0 & 0 & 0 & 0 & 0 & \boldsymbol{C}^T & 0 & 0 \\ 0 & 0 & 0 & 0 & 0 & 0 & 0 & 0 & 0 & \mathbb{I} & 0 \\ 0 & 0 & 0 & 0 & 0 & 0 & 0 & 0 & 0 & 0 & \mathbb{I} \end{bmatrix}, \tag{6. 126}$$

is the noise Jacobian.

The continuous process noise covariance matrix can now be formulated as

$$\boldsymbol{Q}_c = E[\boldsymbol{w}\boldsymbol{w}^T] = \begin{bmatrix} 0 & 0 & 0 & 0 & 0 & 0 & 0 & 0 & 0 & 0 & 0 \\ 0 & \boldsymbol{Q}_f & 0 & 0 & 0 & 0 & 0 & 0 & 0 & 0 & 0 \\ 0 & 0 & \boldsymbol{Q}_\omega & 0 & 0 & 0 & 0 & 0 & 0 & 0 & 0 \\ 0 & 0 & 0 & \boldsymbol{Q}_{p,1} & 0 & 0 & 0 & 0 & 0 & 0 & 0 \\ 0 & 0 & 0 & 0 & \boldsymbol{Q}_{p,2} & 0 & 0 & 0 & 0 & 0 & 0 \\ 0 & 0 & 0 & 0 & 0 & \boldsymbol{Q}_{p,3} & 0 & 0 & 0 & 0 & 0 \\ 0 & 0 & 0 & 0 & 0 & 0 & \boldsymbol{Q}_{p,4} & 0 & 0 & 0 & 0 \\ 0 & 0 & 0 & 0 & 0 & 0 & 0 & \boldsymbol{Q}_{p,5} & 0 & 0 & 0 \\ 0 & 0 & 0 & 0 & 0 & 0 & 0 & 0 & \boldsymbol{Q}_{p,6} & 0 & 0 \\ 0 & 0 & 0 & 0 & 0 & 0 & 0 & 0 & 0 & \boldsymbol{Q}_{bf} & 0 \\ 0 & 0 & 0 & 0 & 0 & 0 & 0 & 0 & 0 & 0 & \boldsymbol{Q}_{b\omega} \end{bmatrix}, \quad (6.127)$$

where, $E[\boldsymbol{w}\boldsymbol{w}^T]$, is the expected value for $\boldsymbol{w}\boldsymbol{w}^T$.

6.6.2.4 Discrete, linear model

The discrete linear model is derived using a first-order discretisation as presented in [3]. In contrast to [2], this method simplifies the implementation of the filter and doesn't affect the filter performance in any significant way [3]. The discrete linearised error dynamics matrix can be calculated by assuming a zero-order hold over the time interval $\Delta t = t_{k+1} - t_k$, as follows

$$\boldsymbol{F}_k = e^{\boldsymbol{F}_c \Delta t}. \quad (6.128)$$

Equation (6.128) can be reduced to first-order to yield

$$\boldsymbol{F}_k \approx \mathbb{I} + \boldsymbol{F}_c \Delta t. \quad (6.129)$$

The discrete linearised error dynamics matrix can now be formulated as

$$\boldsymbol{F}_k = \begin{bmatrix} \mathbb{I} & \Delta t\mathbb{I} & 0 & 0 & 0 & 0 & 0 & 0 & 0 & 0 & 0 \\ 0 & \mathbb{I} & -\Delta t\widehat{\boldsymbol{C}}_k^{+T}\widehat{\boldsymbol{f}}_k^{\times} & 0 & 0 & 0 & 0 & 0 & 0 & -\Delta t\widehat{\boldsymbol{C}}_k^{+T} & 0 \\ 0 & 0 & \mathbb{I} - \Delta t\boldsymbol{\omega}^{\times} & 0 & 0 & 0 & 0 & 0 & 0 & 0 & -\mathbb{I}\Delta t \\ 0 & 0 & 0 & \mathbb{I} & 0 & 0 & 0 & 0 & 0 & 0 & 0 \\ 0 & 0 & 0 & 0 & \mathbb{I} & 0 & 0 & 0 & 0 & 0 & 0 \\ 0 & 0 & 0 & 0 & 0 & \mathbb{I} & 0 & 0 & 0 & 0 & 0 \\ 0 & 0 & 0 & 0 & 0 & 0 & \mathbb{I} & 0 & 0 & 0 & 0 \\ 0 & 0 & 0 & 0 & 0 & 0 & 0 & \mathbb{I} & 0 & 0 & 0 \\ 0 & 0 & 0 & 0 & 0 & 0 & 0 & 0 & \mathbb{I} & 0 & 0 \\ 0 & 0 & 0 & 0 & 0 & 0 & 0 & 0 & 0 & \mathbb{I} & 0 \\ 0 & 0 & 0 & 0 & 0 & 0 & 0 & 0 & 0 & 0 & \mathbb{I} \end{bmatrix}. \quad (6.130)$$

The discrete process noise covariance matrix can be calculated by assuming a zero-order hold over the time interval $\Delta t = t_{k+1} - t_k$, as follows

$$\boldsymbol{Q}_{k-1} = \int_{t_{k-1}}^{t_k} e^{\boldsymbol{F}_c(t_k-\tau)} \boldsymbol{L}_c \boldsymbol{Q}_c \boldsymbol{L}_c^T e^{\boldsymbol{F}_c^T(t_k-\tau)}\, d\tau\,. \tag{6.131}$$

Equation (6.131) can be reduced to first-order to yield

$$\boldsymbol{Q}_k \approx \Delta t \boldsymbol{F}_k \boldsymbol{L}_c \boldsymbol{Q}_c \boldsymbol{L}_c^T \boldsymbol{F}_k^T. \tag{6.132}$$

6.6.2.5 Extended Kalman filter prediction equations

The EKF states the prediction equations that follow in this section. The predicted or *a priori* state estimate is given by

$$\hat{\boldsymbol{x}}_k^- \coloneqq \boldsymbol{F}_k \hat{\boldsymbol{x}}_k^+. \tag{6.133}$$

The predicted or *a priori* state estimate of the covariance matrix is given by

$$\boldsymbol{\mathcal{P}}_{k+1}^- = \boldsymbol{F}_k \boldsymbol{\mathcal{P}}_k^+ \boldsymbol{F}_k^T + \boldsymbol{Q}_k. \tag{6.134}$$

6.6.3 Update step

In the update step, the EKF produces the *a posteriori* estimates by using a measurement to update the expected value of the state as well as the covariance of the state.

6.6.3.1 Measurement residual

The measurement residual can now be defined as the difference between actual measurements of the foot positions and their predicted values. The actual measurements are located in the body coordinate frame, $\boldsymbol{B}$. Therefore, the predicted values are calculated as the predicted foot positions minus the predicted centre of body position, transformed from the inertial coordinate frame, $\boldsymbol{I}$, into the body coordinate frame, $\boldsymbol{B}$, with the predicted rotation matrix. The measurement residual can now be formulated as,

$$\boldsymbol{y}_k \coloneqq \begin{pmatrix} \tilde{\boldsymbol{s}}_{1,k} - \hat{\boldsymbol{C}}_k^- (\hat{\boldsymbol{p}}_{1,k}^- - \hat{\boldsymbol{r}}_k^-) \\ \tilde{\boldsymbol{s}}_{2,k} - \hat{\boldsymbol{C}}_k^- (\hat{\boldsymbol{p}}_{2,k}^- - \hat{\boldsymbol{r}}_k^-) \\ \tilde{\boldsymbol{s}}_{3,k} - \hat{\boldsymbol{C}}_k^- (\hat{\boldsymbol{p}}_{3,k}^- - \hat{\boldsymbol{r}}_k^-) \\ \tilde{\boldsymbol{s}}_{4,k} - \hat{\boldsymbol{C}}_k^- (\hat{\boldsymbol{p}}_{4,k}^- - \hat{\boldsymbol{r}}_k^-) \\ \tilde{\boldsymbol{s}}_{5,k} - \hat{\boldsymbol{C}}_k^- (\hat{\boldsymbol{p}}_{5,k}^- - \hat{\boldsymbol{r}}_k^-) \\ \tilde{\boldsymbol{s}}_{6,k} - \hat{\boldsymbol{C}}_k^- (\hat{\boldsymbol{p}}_{6,k}^- - \hat{\boldsymbol{r}}_k^-) \end{pmatrix}. \tag{6.135}$$

6.6.3.2 Linearisation of foot position measurement model

For the linearisation of the relative foot position measurement model, (6.48), let

$$\boldsymbol{s}_i \approx \bar{\boldsymbol{s}}_i + \boldsymbol{\delta s}_i, \tag{6.136}$$

and from (6.58),

$$\boldsymbol{C} \approx [\mathbb{I} - \boldsymbol{\delta\phi}^{\times}]\overline{\boldsymbol{C}}\,. \tag{6.137}$$

Substituting (6.136), (6.137), (6.63) and (6.106) into (6.48), yields

$$\boldsymbol{s}_i = \bar{\boldsymbol{s}}_i + \boldsymbol{\delta s}_i = [\mathbb{I} - \boldsymbol{\delta\phi}^{\times}]\overline{\boldsymbol{C}}\,[(\bar{\boldsymbol{p}} + \boldsymbol{\delta p}) - (\bar{\boldsymbol{r}} + \boldsymbol{\delta r})\,] + \boldsymbol{n}_i. \tag{6.138}$$

Expanding (6.138), gives

$$\bar{\boldsymbol{s}}_i + \boldsymbol{\delta s}_i = \overline{\boldsymbol{C}}\,(\bar{\boldsymbol{p}} - \bar{\boldsymbol{r}}) + \overline{\boldsymbol{C}}\,(\boldsymbol{\delta p} - \boldsymbol{\delta r}) - \boldsymbol{\delta\phi}^{\times}\big(\overline{\boldsymbol{C}}(\bar{\boldsymbol{p}} - \bar{\boldsymbol{r}})\big) - \boldsymbol{\delta\phi}^{\times}\big(\overline{\boldsymbol{C}}(\boldsymbol{\delta p} - \boldsymbol{\delta r})\big) + \boldsymbol{n}_i. \tag{6.139}$$

From (6.48) we can formulate that

$$\bar{\boldsymbol{s}}_{\boldsymbol{i}} = \overline{\boldsymbol{C}}(\bar{\boldsymbol{p}} - \bar{\boldsymbol{r}}) + \boldsymbol{n}_i. \tag{6.140}$$

Rewriting (6.139) by recognising (6.140), yields

$$\boldsymbol{\delta s}_i = \overline{\boldsymbol{C}}\,(\boldsymbol{\delta p} - \boldsymbol{\delta r}) - \boldsymbol{\delta\phi}^{\times}\big(\overline{\boldsymbol{C}}(\bar{\boldsymbol{p}} - \bar{\boldsymbol{r}})\big) - \boldsymbol{\delta\phi}^{\times}\big(\overline{\boldsymbol{C}}(\boldsymbol{\delta p} - \boldsymbol{\delta r})\big). \tag{6.141}$$

The term, $\boldsymbol{\delta\phi}^{\times}\big(\overline{\boldsymbol{C}}(\boldsymbol{\delta p} - \boldsymbol{\delta r})\big)$, in (6.141) can be neglected due to it being a cross product of state deviations. The final linearised equation at time step k can therefore be formulated as

$$\boldsymbol{\delta s}_{i,k} = \boldsymbol{s}_{i,k} - \widehat{\boldsymbol{C}}_k^-\,(\hat{\boldsymbol{p}}_{1,k}^- - \hat{\boldsymbol{r}}_k^-) \approx -\widehat{\boldsymbol{C}}_k^-\boldsymbol{\delta r}_k^- + \widehat{\boldsymbol{C}}_k^-\boldsymbol{\delta p}_{i,k}^- + \Big(\widehat{\boldsymbol{C}}_k^-(\boldsymbol{p}_{i,k}^- - \boldsymbol{r}_k^-)\Big)^{\times}\boldsymbol{\delta\phi}_k^-, \tag{6.142}$$

corresponding to Bloesch et al.[2].

6.6.3.3 Measurement Jacobian

By substituting the linearised foot position measurement model, (6.142), into the measurement residual, $\boldsymbol{y}_k$, the measurement Jacobian, as defined in (6.6) can now be derived and formulated as

$$\boldsymbol{H}_k = \frac{\partial \boldsymbol{y}_k}{\partial \hat{\boldsymbol{x}}_k} \tag{6.143}$$

$$= \begin{bmatrix} -\widehat{\boldsymbol{C}}_k^- & \boldsymbol{0} & \Big(\widehat{\boldsymbol{C}}_k^-(\boldsymbol{p}_{1,k}^- - \boldsymbol{r}_k^-)\Big)^{\times} & \widehat{\boldsymbol{C}}_k^- & \boldsymbol{0} & \boldsymbol{0} & \boldsymbol{0} & \boldsymbol{0} & \boldsymbol{0} & \boldsymbol{0} & \boldsymbol{0} \\ -\widehat{\boldsymbol{C}}_k^- & \boldsymbol{0} & \Big(\widehat{\boldsymbol{C}}_k^-(\boldsymbol{p}_{2,k}^- - \boldsymbol{r}_k^-)\Big)^{\times} & \boldsymbol{0} & \widehat{\boldsymbol{C}}_k^- & \boldsymbol{0} & \boldsymbol{0} & \boldsymbol{0} & \boldsymbol{0} & \boldsymbol{0} & \boldsymbol{0} \\ -\widehat{\boldsymbol{C}}_k^- & \boldsymbol{0} & \Big(\widehat{\boldsymbol{C}}_k^-(\boldsymbol{p}_{3,k}^- - \boldsymbol{r}_k^-)\Big)^{\times} & \boldsymbol{0} & \boldsymbol{0} & \widehat{\boldsymbol{C}}_k^- & \boldsymbol{0} & \boldsymbol{0} & \boldsymbol{0} & \boldsymbol{0} & \boldsymbol{0} \\ -\widehat{\boldsymbol{C}}_k^- & \boldsymbol{0} & \Big(\widehat{\boldsymbol{C}}_k^-(\boldsymbol{p}_{4,k}^- - \boldsymbol{r}_k^-)\Big)^{\times} & \boldsymbol{0} & \boldsymbol{0} & \boldsymbol{0} & \widehat{\boldsymbol{C}}_k^- & \boldsymbol{0} & \boldsymbol{0} & \boldsymbol{0} & \boldsymbol{0} \\ -\widehat{\boldsymbol{C}}_k^- & \boldsymbol{0} & \Big(\widehat{\boldsymbol{C}}_k^-(\boldsymbol{p}_{5,k}^- - \boldsymbol{r}_k^-)\Big)^{\times} & \boldsymbol{0} & \boldsymbol{0} & \boldsymbol{0} & \boldsymbol{0} & \widehat{\boldsymbol{C}}_k^- & \boldsymbol{0} & \boldsymbol{0} & \boldsymbol{0} \\ -\widehat{\boldsymbol{C}}_k^- & \boldsymbol{0} & \Big(\widehat{\boldsymbol{C}}_k^-(\boldsymbol{p}_{6,k}^- - \boldsymbol{r}_k^-)\Big)^{\times} & \boldsymbol{0} & \boldsymbol{0} & \boldsymbol{0} & \boldsymbol{0} & \boldsymbol{0} & \widehat{\boldsymbol{C}}_k^- & \boldsymbol{0} & \boldsymbol{0} \end{bmatrix}.$$

6.6.3.4 Measurement noise matrix

The total measurement noise matrix is formed by stacking the all of the single measurement noise matrices, as defined in (6.47), from $i = 1$, to $i = 6$, as a diagonal matrix:

$$\boldsymbol{R}_k = \begin{bmatrix} \boldsymbol{R}_{1,k} & 0 & 0 & 0 & 0 & 0 \\ 0 & \boldsymbol{R}_{2,k} & 0 & 0 & 0 & 0 \\ 0 & 0 & \boldsymbol{R}_{3,k} & 0 & 0 & 0 \\ 0 & 0 & 0 & \boldsymbol{R}_{4,k} & 0 & 0 \\ 0 & 0 & 0 & 0 & \boldsymbol{R}_{5,k} & 0 \\ 0 & 0 & 0 & 0 & 0 & \boldsymbol{R}_{6,k} \end{bmatrix}. \tag{6.144}$$

6.6.3.5 Extended Kalman filter update equations

The Extended Kalman filter states the update equations that follow in this section. These standard equations were formulated in the background of this chapter but are given here again, referencing the specific equations needed to calculate the update step, as derived throughout this chapter.

By using the *a priori* state estimate covariance matrix as defined in (6.134) together with the measurement Jacobian, (6.143), and the measurement noise matrix, (6.144), the residual covariance is calculated as,

$$\boldsymbol{S}_k \coloneqq \boldsymbol{H}_k \boldsymbol{\mathcal{P}}_k^- \boldsymbol{H}_k^T + \boldsymbol{R}_k. \tag{6.145}$$

Combining the *a priori* state estimate, (6.134), with the measurement Jacobian, (6.143), and the residual covariance, (6.145), the Kalman gain is calculated as,

$$\boldsymbol{K}_k \coloneqq \boldsymbol{\mathcal{P}}_k^- \boldsymbol{H}_k^T \boldsymbol{S}_k^{-1}. \tag{6.146}$$

The resulting correction vector is defined as the product of the Kalman gain, (6.146), and the measurement residual, (6.135), and formulated as,

$$\Delta \boldsymbol{x}_k \coloneqq \boldsymbol{K}_k \boldsymbol{y}_k, \tag{6.147}$$

where the update or *a posteriori* state estimate is updated using $\Delta \boldsymbol{x}_k$:

$$\hat{\boldsymbol{x}}_k^+ \coloneqq \hat{\boldsymbol{x}}_k^- + \Delta \boldsymbol{x}_k \tag{6.148}$$

Note that an extra calculation is needed for the orientation state because the extracted rotational correction, $\Delta \boldsymbol{\phi}_k$, is of three dimensions, in contrast to the quaternion, that is of four dimensions. The rotation correction is applied to correct the predicted quaternion, therefore:

$$\hat{\boldsymbol{q}}_k^+ = \exp(\Delta \boldsymbol{\phi}_k) \otimes \hat{\boldsymbol{q}}_k^-. \tag{6.149}$$

Finally, the update *a posteriori* estimate of the state covariance matrix is given by

$$\boldsymbol{\mathcal{P}}_k^+ \coloneqq (\mathbb{I} - \boldsymbol{K}_k \boldsymbol{H}_k)\boldsymbol{\mathcal{P}}_k^-. \tag{6. 150}$$

6.7 Conclusion

This chapter discussed the state estimation approach used in this study. The state estimation for the hexapod robot platform was derived using the framework presented by Bloesch et al. [2]. It uses an EKF to estimate the full state of a robot body by fusing the robot kinematics with an IMU. The chapter started by providing background information about the EKF. Here, the operation of the EKF was discussed and the general EKF equations were provided.

Thereafter, the state definition for the EKF was derived. The state vector consists of the position, velocity and the corresponding quaternion of the centre of the robot body, the contact points of the six feet with the ground, and the acceleration and angular rate bias values. The corresponding state error vector was also defined. Next, the prediction model needed by the filter to propagate the state from one time step to the next, was derived. Here, the set of continuous time differential equations for the state was derived. By using the kinematic measurement model, derived in Chapter 4, as well as the joint position measurement model, derived in Chapter 5, the filter measurement model was derived. The filter measurement model is used in the update step of the EKF.

The chapter concluded by discussing the state estimation's EKF equations. The filtering convention was firstly provided followed by the EKF prediction and update steps. For the prediction step, the continuous time differential equations derived in the filter prediction model, were discretised. Here, a zero-order hold was assumed with regards to the IMU measurement quantities and the effect of the incremental rotation was neglected. Next, the continuous time differential equations were linearised in order to propagate the state estimate covariance matrix through the state dynamics. The linearised differential equations described the error dynamics. In contrast to [2], the linearised error dynamic matrix and the discrete process noise covariance matrix were derived using a zero-order hold on the noise terms as presented by [3]. This simplifies the filter implementation. The prediction step discussion concluded with the formulation of the *a priori* state estimate and *a priori* covariance state estimate matrix equations.

For the update step, the measurement residual was first formulated as the difference between the actual foot position measurements and their predicted values. Hereafter, the linearised foot position measurement model was derived and used to calculate the measurement Jacobian. The measurement noise matrices, as defined in the filter measurement model, were stacked diagonally to derive the total measurement noise matrix. Finally, the update equations were discussed. Here, the

measurement residual, the measurement Jacobian and the measurement noise matrices together with the *a priori* covariance were used to produce the *a posteriori* estimates. The implementation of the equations derived in this chapter will be discussed in Chapter 7 together with the state estimation results.

Chapter 7: Implementation and results

"An algorithm must be seen to be believed."

~ Donald Ervin Knuth

7.1 Introduction

This chapter discusses the implementation of the kinematic model and the state estimation as well as the results of the state estimation. The verification of the kinematic model is firstly discussed. Thereafter, the state estimation implementation is discussed where, the program architecture is given, the quantities of the noise parameters for the EKF are derived, and the initialization of the EKF are discussed. The chapter concludes by presenting and discussing the state estimation results obtained from multiple experiments.

7.2 Kinematic model and verification

This section discusses the verification of the kinematic model derived in Chapter 4. The kinematic model equations were implemented in Matlab® as a function that was used by the EKF. In order to verify the kinematic model results, it had to be compared to reliable reference measurements. However, measurement information about the robot platform is not supplied by the manufacturers. Therefore, measurements were taken from the physical platform. CAD models were created of all the parts of the robot platform and used to build an assembly in SolidWorks®. Fig. 7.1 shows the robot assembly.

In SolidWorks, specific angles were assigned to the robot joints of the assembly and the foot positions were then measured. These measurements were taken expressed in the body coordinate frame as defined in Chapter 4. The same joint angles were used as input for the kinematic model. Multiple tests were conducted with the robot assembly resembling possible walking poses. The Y-axis and Z-axis measurements showed no errors in the millimetre range using the leg kinematic model. A maximum error of $2\,\mathrm{mm}$ in the X-axis measurement of the leg kinematic model was found. This error is distributed in all axes in the robot kinematic model.

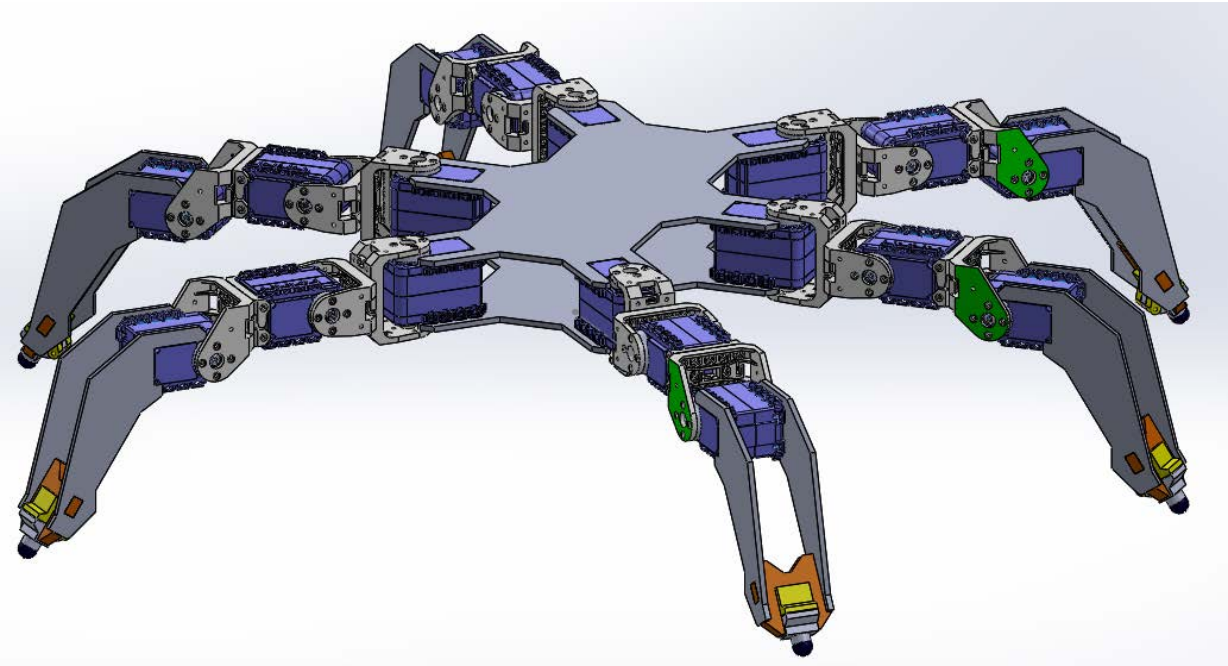

Figure 7. 1: Robot platform assembly model.

The mentioned error in the X-axis of the leg kinematic model is caused by the round foot end. This is because the length of *link 3*, representing the tibia of each leg, is defined as the measurement between *joint 3* and the contact point of the foot with the ground. (As defined in Chapter 4.) Therefore, depending on where the foot end makes contact with the ground, the real length of *link 3* changes and no longer corresponds to the assigned length in the kinematic model. This error is however almost unnoticeable and included in the kinematic measurement model of the state estimation, verifying the kinematic model derived.

7.3 State estimation implementation

7.3.1 Program architecture

This section discusses the implementation of the state estimation as derived in Chapter 6. The EKF equations were implemented in Matlab®. Fig. 7.2 shows the architecture diagram for the main part of the code. In Fig 7.2, each function is enclosed in a different coloured block. Corresponding coloured arrows indicate how the output of a specific function is used as input in another function. The Matlab® code with a detailed discussion about all the functions used to implement the state estimation, can be found in Appendix A.

The code begins by extracting all of the measured data that were captured by the platform into Matlab®. The sensor data acquisition was discussed in detail in Chapter 5. Hereafter, the initialisation

needed by the EKF is performed. This consists of declaring all the noise parameters, an initial state vector and an initial covariance matrix. The quantities assigned to the noise parameters are derived and discussed in section 7.3.2. The initial state vector and covariance matrix is needed to start the EKF loop. The derivation of the initial state vector and the initial covariance matrix are discussed in section 7.3.3.

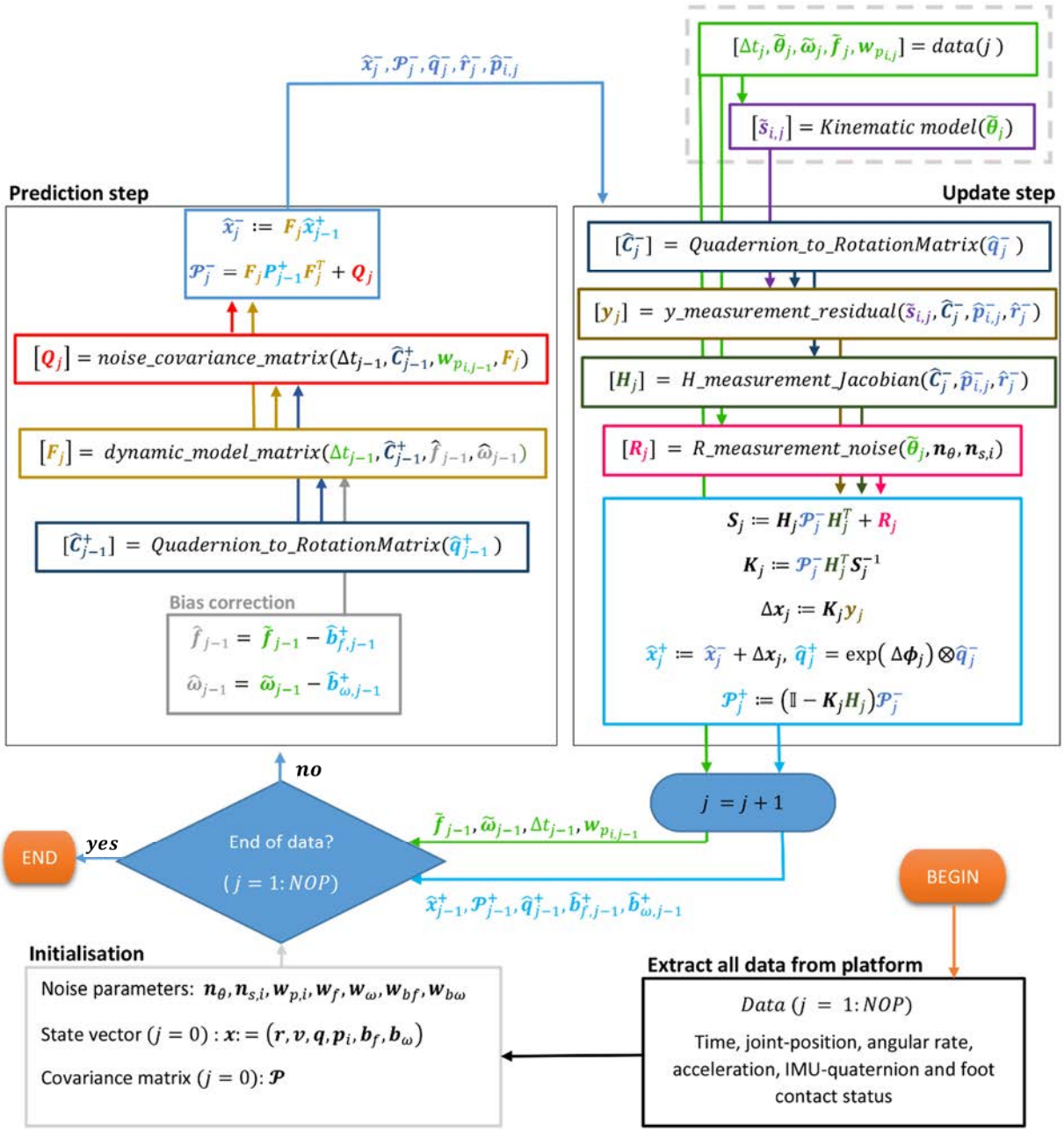

Figure 7. 2: State estimation program architecture diagram.

After the initialisation, the EKF loop is entered for data point one, (time step one), until the end of the data is reached. The end of the data is identified as the *number of points* (NOP) captured by the data acquisition process. The EKF loop starts with the prediction step. First the IMU bias values are corrected as derived in (6.62) and (6.65).

Next the *a posteriori* quaternion estimate is converted to a rotation matrix with the function *"Quadernion_to_RotationMatrix"* that implements (6.15). The dynamic model matrix is then calculated with the function *"dynamic_model_matrix"* that implements (6.130). Using the dynamic model matrix and the *a posteriori* rotation matrix, the function *"noise_covariance_matrix"* calculates the noise covariance matrix as defined in (6.132). The dynamic model matrix is then used to update the *a priori* state estimate as defined in (6.133). The noise covariance matrix together with the dynamic model matrix is used to update the *a priori* covariance matrix as defined in (6.134). This concludes the prediction step.

In the update step, the *a priori* quaternion estimate is firstly converted to a rotation matrix with the *"Quadernion_to_RotationMatrix"* function. Thereafter, the measurement residual is calculated using the measured foot positions and the *a priori* estimated foot positions with the function *"y_measurement_residual"* implementing (6.135). The measured foot positions are calculated with the *"Kinematic_model"* function implementing the kinematic model derived in Chapter 4. The measurement Jacobian is then calculated with the *"H_measurement_Jacobian"* function implementing (6.143). The total measurement noise matrix is computed using the defined noise parameters with the function *"R_measurement_noise"* implementing (6.47) and (6.144). The update step is completed with the calculation of the *a posteriori* state estimate and covariance using (6.145)-(6.150). The EKF loop is then repeated for all the data points.

When using (6.149) a drift was noticed in the estimation that resulted in inaccurate position estimation. A modified method was used to convert the rotational correction vector to a quaternion correction [83]. Here, the rotation vector was interpreted as Euler angles, $\mathbf{u_\phi} = [\phi \quad \theta \quad \psi]^T$, where, ϕ, represents the pitch, θ, represents the roll and, ψ, represents the yaw. The following equation was used to calculate the quaternion correction:

$$\boldsymbol{q} = \begin{bmatrix} \cos\left(\frac{\phi}{2}\right)\cos\left(\frac{\psi}{2}\right)\sin\left(\frac{\theta}{2}\right) - \sin\left(\frac{\phi}{2}\right)\cos\left(\frac{\theta}{2}\right)\sin\left(\frac{\psi}{2}\right) \\ \cos\left(\frac{\phi}{2}\right)\sin\left(\frac{\theta}{2}\right)\sin\left(\frac{\psi}{2}\right) - \cos\left(\frac{\theta}{2}\right)\cos\left(\frac{\psi}{2}\right)\sin\left(\frac{\phi}{2}\right) \\ \cos\left(\frac{\phi}{2}\right)\cos\left(\frac{\theta}{2}\right)\sin\left(\frac{\psi}{2}\right) + \sin\left(\frac{\phi}{2}\right)\cos\left(\frac{\psi}{2}\right)\sin\left(\frac{\theta}{2}\right) \\ \cos\left(\frac{\phi}{2}\right)\cos\left(\frac{\theta}{2}\right)\cos\left(\frac{\psi}{2}\right) + \sin\left(\frac{\phi}{2}\right)\sin\left(\frac{\theta}{2}\right)\sin\left(\frac{\psi}{2}\right) \end{bmatrix}. \quad (7.1)$$

This quaternion correction value was then used to correct the predicted quaternion.

7.3.2 Noise parameters

This section discusses the values assigned to the noise processes in the EKF. Initial standard deviations for the noise parameters were derived first. Thereafter, the noise parameters were empirically tuned to a point where the EKF presented the best state estimation results.

The discrete standard deviations of the additive white Gaussian noise processes, $\boldsymbol{w}_f$ and $\boldsymbol{w}_\omega$, affecting the IMU measurement quantities, were obtained by dividing the root PSD values (provided in Chapter 5) by the root of the sampling time [87],

$$\sigma_{\boldsymbol{w}_f d} = \frac{0.00078}{\sqrt{\Delta t}}\ \mathrm{m/s^2}, \quad (7.2)$$

$$\sigma_{\boldsymbol{w}_\omega d} = \frac{0.000523}{\sqrt{\Delta t}}\ \mathrm{rad/s}. \quad (7.3)$$

The initial variance quantities for covariance matrices, $\boldsymbol{Q}_f$ and $\boldsymbol{Q}_\omega$, where then obtained by squaring the standard deviations as defined in (7.2) and (7.3). For $\Delta t = 0.05$ s, these variance quantities are given as

$$\sigma^2_{\boldsymbol{w}_f d} = 1.231 \times 10^{-5}, \quad (7.4)$$

$$\sigma^2_{\boldsymbol{w}_\omega d} = 5.483 \times 10^{-6}. \quad (7.5)$$

For covariance parameters, $\boldsymbol{Q}_{bf}$ and $\boldsymbol{Q}_{b\omega}$, the initial discrete standard deviations of the white Gaussian noise processes, $\boldsymbol{w}_{bf}$ and $\boldsymbol{w}_{b\omega}$, were derived by multiplying the continuous-time standard deviations defined in Chapter 5 by the square of the sampling time [87],

$$\sigma_{\boldsymbol{w}_{bfd}} = 0.0001\sqrt{\Delta t}\ \mathrm{m/s^2}, \quad (7.6)$$

$$\sigma_{\boldsymbol{w}_{b\omega d}} = 0.000618\sqrt{\Delta t} \text{ rad/s.} \quad (7.7)$$

The initial variance quantities for covariance matrices, $\boldsymbol{Q}_{bf}$ and $\boldsymbol{Q}_{b\omega}$, were then obtained by squaring the standard deviations as defined in (7.6) and (7.7). For $\Delta t = 0.05$ s, these variance quantities are given as

$$\sigma^2_{\boldsymbol{w}_{fd}} = 5 \times 10^{-10}\,, \quad (7.8)$$

$$\sigma^2_{\boldsymbol{w}_{\omega d}} = 1.9097 \times 10^{-8}\,. \quad (7.9)$$

For covariance matrix, $\boldsymbol{R}_\theta$, the initial standard deviation of the discrete Gaussian noise process, $\boldsymbol{n}_\theta$, representing the error in the joint position feedback were defined as given in Chapter 5:

$$\sigma_{\boldsymbol{n}_\theta} = 0.0087 \text{ rad.} \quad (7.10)$$

From (7.9) the initial variance quantity as used in the EKF were calculated as

$$\sigma^2_{\boldsymbol{n}_\theta} = 0.0087^2\,. \quad (7.11)$$

For the kinematic measurement model, as defined in Chapter 4, the additive discrete Gaussian noise term, $\boldsymbol{n}_{s,i}$, representing the error in the kinematic model, can be defined using the kinematic model validation test results. Let the maximum error in any axis direction of the kinematic model be defined as the standard deviation of $\boldsymbol{n}_{s,i}$,

$$\sigma_{\boldsymbol{n}_{s,i}} = 0.002 \text{ m.} \quad (7.12)$$

The variance quantity used as the initial value of the covariance parameter, $\boldsymbol{R}_{s,i}$, was then calculated as

$$\sigma^2_{\boldsymbol{n}_{s,i}} = 0.000004\,. \quad (7.13)$$

For the covariance parameter, $\boldsymbol{Q}_{p,i}$, as defined in Chapter 6, the standard deviation of the white noise process, $\boldsymbol{w}_{p,i}$, allowing a certain amount of foot slippage, were defined as

$$\sigma_{\boldsymbol{w}_{p,i}} = \frac{7.071 \times 10^{-5}}{\sqrt{\Delta t}} \text{ m,} \quad (7.14)$$

so that for $\Delta t = 0.05$ s, the initial variance is calculated as

$$\sigma^2_{\boldsymbol{w}_{p,i}} = 1 \times 10^{-7}\,. \tag{7. 15}$$

In order to compensate for inaccuracies and assumptions in the filter model, the initial noise parameters were empirically tuned until the state estimation showed the best results. Table 7.1 summarises the final standard deviation noise parameter values used in the EKF.

Table 7. 1: Final standard deviation values of the noise parameters.

Noise parameter	Standard deviation (discrete)
$\boldsymbol{n}_\theta$	$\sigma_{\boldsymbol{n}_\theta} = 0.2$ rad
$\boldsymbol{n}_{s,i}$	$\sigma_{\boldsymbol{n}_{s,i}} = 0.002$ m
$\boldsymbol{w}_f$	$\sigma_{\boldsymbol{w}_f} = \frac{0.234}{\sqrt{\Delta t}}$ m/s^2
$\boldsymbol{w}_\omega$	$\sigma_{\boldsymbol{w}_\omega} = \frac{0.157}{\sqrt{\Delta t}}$ rad/s
$\boldsymbol{w}_{bf}$	$\sigma_{\boldsymbol{w}_{bf}} = 0.03\sqrt{\Delta t}$ m/s^2
$\boldsymbol{w}_{b\omega}$	$\sigma_{\boldsymbol{w}_{b\omega}} = 0.184\sqrt{\Delta t}$ rad/s
$\boldsymbol{w}_{p,i}$	$\sigma_{\boldsymbol{w}_{p,i}} = \frac{7.071 \times 10^{-5}}{\sqrt{\Delta t}}$ m

The variances of the noise parameters were obtained by squaring the standard deviation values as given in Table 7.1. The standard deviations of the noise parameters $\boldsymbol{n}_{s,i}$ and $\boldsymbol{w}_{p,i}$, remained the same as initially assigned. The standard deviation of the joint position noise parameter, $\boldsymbol{n}_\theta$, and all the IMU noise parameters, $\boldsymbol{w}_f, \boldsymbol{w}_\omega, \boldsymbol{w}_{bf}$ and $\boldsymbol{w}_{b\omega}$, increased.

The joint position measurement feedback were scaled from a 10 bit feedback value to an 8 bit feedback value. This decreased the joint position feedback accuracy and can account for the increased noise parameter value. Since the IMU used in this study is a low-cost MEMS device, the increase of the IMU noise parameters were expected. Another notable source that can account for the increased IMU noise parameters is the vibration of the robot. Vibration directly influences the accuracy of inertial devices, therefore the use of low-cost IMUs on devices prone to vibration is not recommended.

7.3.3 Initialisation

This section discusses the initial values assigned to the state vector and covariance matrix. These initial values are needed to start the EKF loop and can influence the settling time of the filter. Since any navigation period of the robot will start with the robot motionless, sensor data was recorded for a period of time with the robot at stand still. This data was then used to run the EKF with random initial values. The results of this test showed that the filter settled at specific values for the *a posteriori* state estimation. These settled values were assigned as the initial values for the robot's state.

For the position of the centre of the body expressed in the inertial coordinate frame, $\boldsymbol{r} = [1,1,1.9]^T$. For the velocity of the centre of the body expressed in the inertial coordinate frame, $\boldsymbol{v} = [0,0,0]^T$. For the quaternion representing the orientation of the centre of the body expressed in the inertial coordinate frame, $\boldsymbol{q} = [0,0,0,1]^T$. Expressed in the body coordinate frame, the acceleration bias, $\boldsymbol{b}_f = [0,0,0]^T$, and the angular rate bias, $\boldsymbol{b}_\omega = [0,0,0]^T$. Even though the robot will begin its navigation motionless, the robot's foot positions can differ. Therefore, the first foot positions as calculated by the kinematic model was used. The kinematic model output is however expressed in the body coordinate frame. In order to express the foot positions in the inertial coordinate frame, the initial centre of body position values were added to the kinematic model results to produce the initial foot position values, $\boldsymbol{p}_i = \boldsymbol{s}_i + \boldsymbol{r}$. For simplicity, the initial covariance matrix were defined as, $\boldsymbol{\mathcal{P}} = 0.0001 \times [\mathbb{I}]_{33\times33}$.

7.4 State estimation results

7.4.1 Test description

A series of experiments were performed using the hexapod platform. During these experiments, the sensor data for the state estimation were collected as discussed in Chapter 5, and ground truth measurements were independently collected by a Vicon motion capture system. The collected sensor data were used as input for the EKF code implemented in Matlab® to provide the estimation. For all of the experiments conducted, the comparison between the estimation and the ground truth measurements was investigated to validate the state estimation approach implemented in this study. Background on the Vicon system and the use of it as well as the current control of the robot will now be discussed.

7.4.1.1 Vicon system

The Vicon system is a motion capturing system that tracks rigid bodies in 3D space [4]. The specific system used in this study consists of twelve cameras. Through a software interface and two I/O machines, these cameras tracked reflective markers that were placed on the robot platform. Fig 7.3 shows the robot platform used in this study with the markers placed on it.

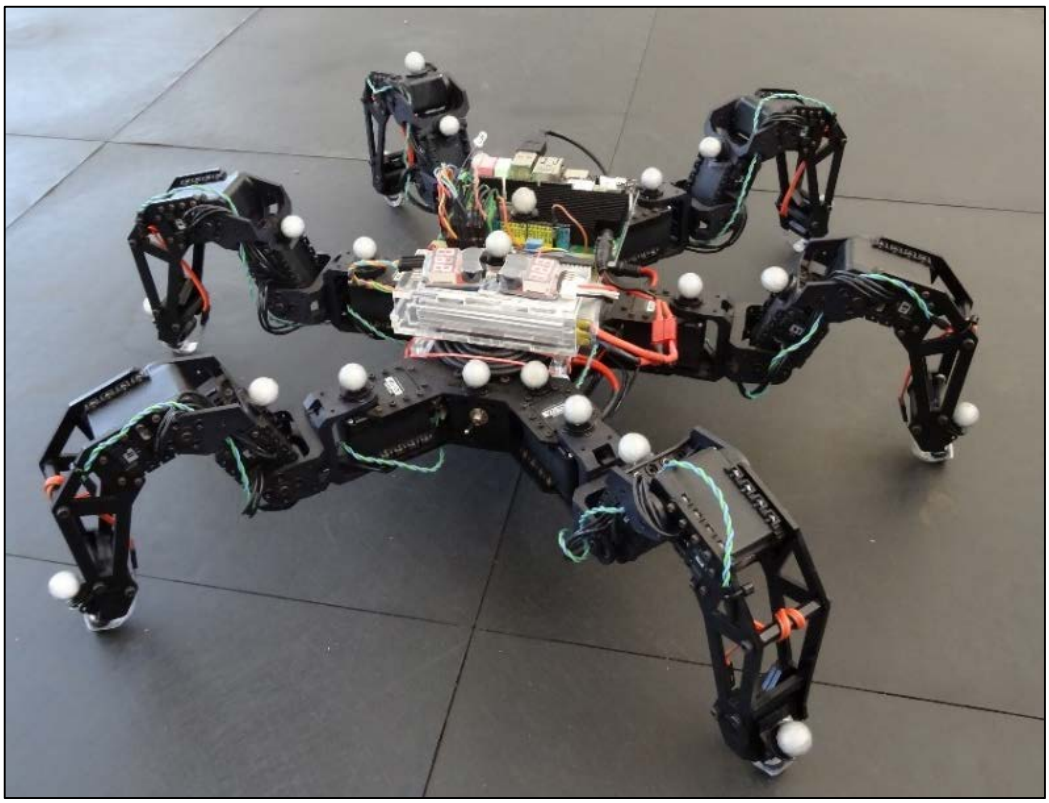

Figure 7. 3: Robot platform with Vicon markers.

Upon start-up of the system, all noise in the Vicon's arena was first filtered out. The system was further calibrated with an accurately calibrated object known as a *wand*. The Vicon calibration concluded with the setting of an origin using the wand. Next, the robot platform, with the reflective markers on it, was placed in the Vicon arena. In order to create an object representing the platform, specific markers were selected and a reference frame location was defined. The reference frame location was set to correspond to the body coordinate frame as defined in the state estimation. The platform's motion was then tracked and recorded through the created object for all of the conducted experiments. Fig. 7.4 shows the Vicon software environment with the created object.

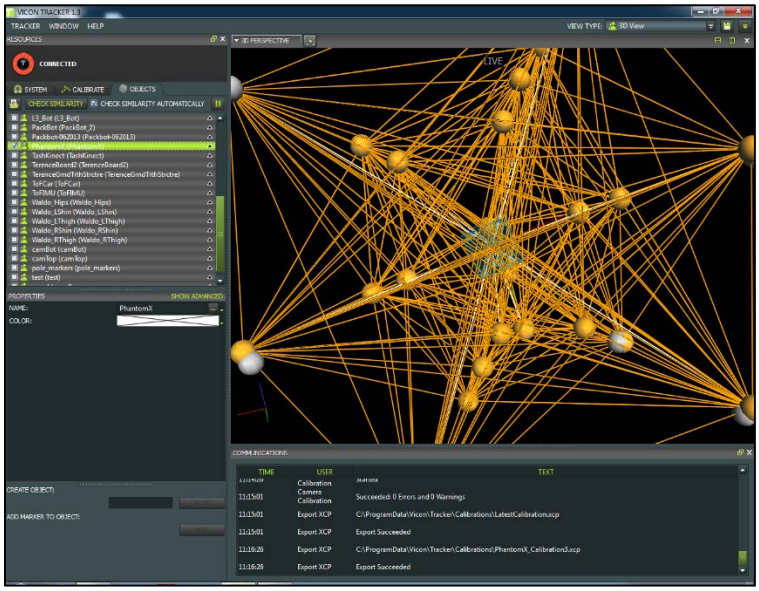

Figure 7. 4: Vicon software environment.

For each time step, t, two vectors describing the reference frame were recorded by the Vicon system. The first was a position vector, $\boldsymbol{r_v} = [x, y, z]$, describing the x, y and z positions of the origin of the reference frame. The second was a quaternion, $\boldsymbol{q_v} = [q_0, q_1, q_2, q_3\ ]$, describing the orientation of the reference frame.

The velocity of the reference frame origin was calculated as the numerical position derivative,

$$\boldsymbol{v}_V = \frac{\Delta \boldsymbol{r_v}}{\Delta \boldsymbol{t}}. \tag{7. 16}$$

The Euler angle vector, defined as

$$\mathbf{u} = [\phi \quad \theta \quad \psi]^T, \tag{7. 17}$$

where, the symbol, ϕ, represents the pitch, the symbol, θ, represents the roll and the symbol, ψ, represents the yaw, were calculated using $\boldsymbol{q_v}$ as follows [83]:

$$\mathbf{u} = \begin{bmatrix} atan2(-2q_1q_3 + 2q_0q_2, q_3^2 - q_2^2 - q_1^2 + q_0^2) \\ asin(2q_2q_3 + 2q_0q_1) \\ atan2(-2q_1q_2 + 2q_0q_3, q_2^2 - q_3^2 + q_0^2 - q_1^2) \end{bmatrix}. \tag{7. 18}$$

7.4.1.2 Robot control

The control of the robot is out of the scope of this study. In order to test the state estimation computed for the robot platform, open source code was uploaded onto the platform's ArbotiX-M Robocontroller which allowed the platform to be controlled by an ArbotiX commander. Both these devices were

included in the PhantomX Mark II kit from Trossen Robotics [51]. The open source code used as firmware for the platform is known as the "PhantomX Hexapod Phoenix Code" and is distributed through Trossen Robotics [88]. The current control approach is limited to relatively even terrain. The firmware was modified to send out the servo positions which increased vibrations on the robot when navigating. The firmware offers a variety of control options including different gait possibilities, body movement and speed control which were used in the experiments conducted.

7.4.2 Results and discussion

This section provides the results obtained from multiple experiments conducted with the robot platform. Due to the limited control of approach of the robot, all the experiments were conducted on relatively even terrain. The experiments were conducted in such a manner to validate the state estimation approach by focussing on the accuracy of the estimates for the full body pose needed for control of a robot.

In order to validate that the state estimation does not depend on a specific gait, two experiments implementing two different gaits were conducted. In both experiments the robot navigated on even terrain in a square form. Since the yaw angle is not fully observable, the experiments were conducted without the robot turning. In the first experiment the robot navigated using a ripple gait while in the second, the robot navigated with a tripod gait. Fig. 7.5 and Fig. 7.6 shows the comparison between the estimated position and the Vicon system's position outputs of the robot with a ripple and a tripod gait respectively.

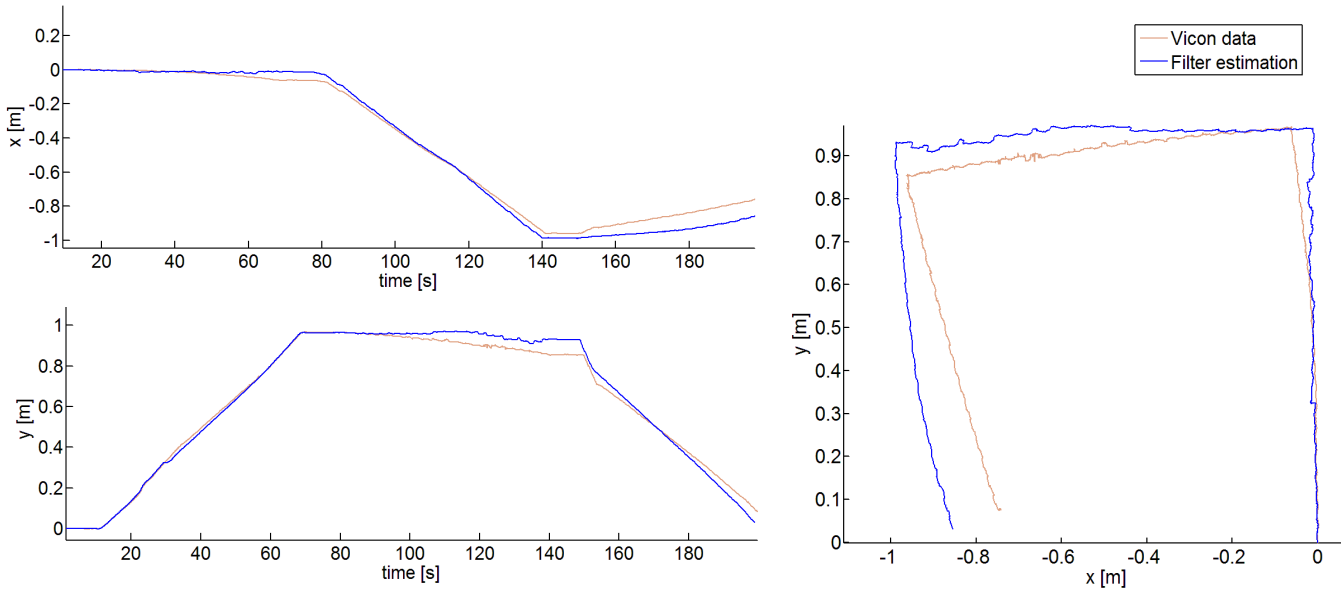

Figure 7. 5: Comparison of the estimated position and the Vicon position outputs for ripple gait.

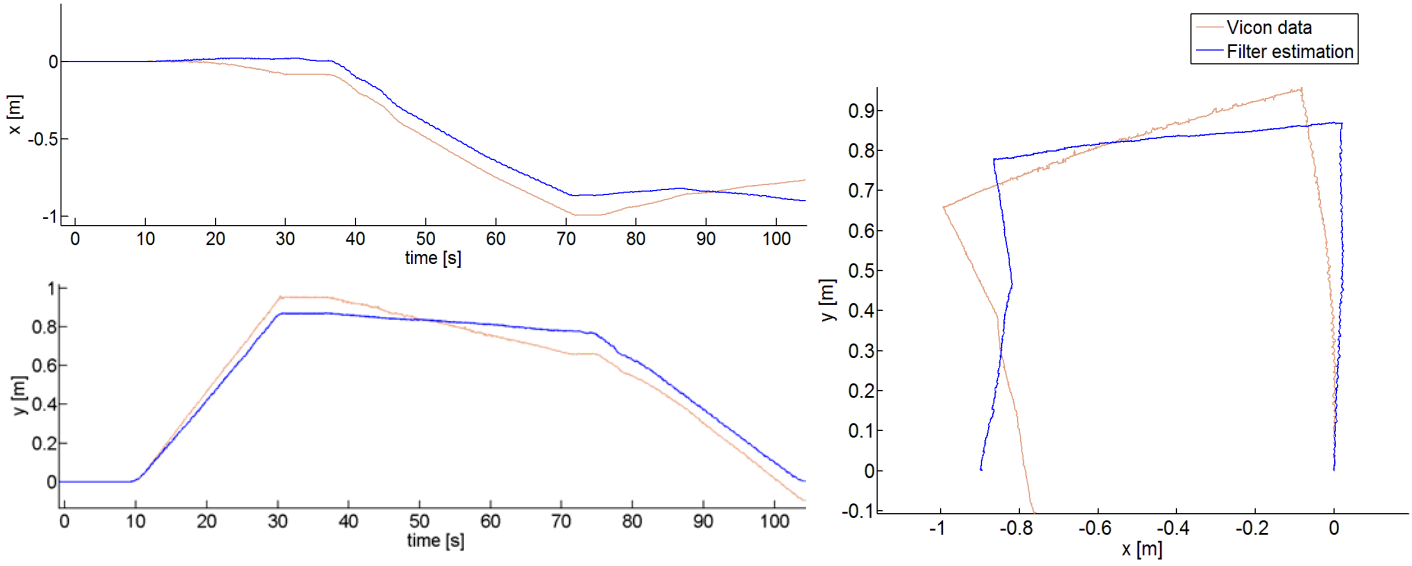

Figure 7. 6: Comparison of the estimated position and the Vicon position outputs for tripod gait.

A small drift in the position estimates occurs in the results of both the experiments. This is due to the position not being fully observable. The ripple gait estimation shows a drift of 5 % in the X-axis position and 1 % in the Y-axis position of the travelled distance. The tripod gait estimation's drift amounts up to 9 % in the X-axis position and 8 % in the Y-axis position of the travelled distance. Increased vibrations on the robot when navigating with tripod gait compared to ripple gait caused the drift difference between the two experiments. The vibrations increase errors in the IMU data, especially in the Z-axis of the body coordinate frame, and is caused by the current control approach. The influence of the vibration of the robot on the estimation can also be noticed in the Z-axis position estimation of the experiments. Fig. 7.7 shows the comparison between the z position estimation of the tripod and ripple experiments.

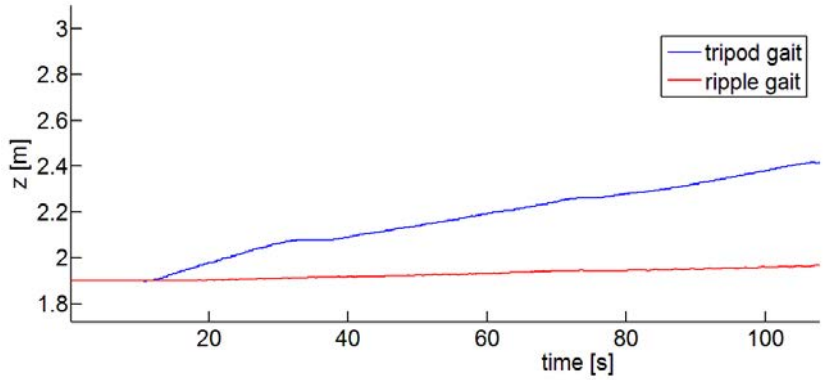

Figure 7. 7: Comparison between the z position estimation of the ripple and tripod experiment.

Bloesch et al. [2] observed a 10 % drift in their estimation results and stated that notable sources of the drift include inaccurate leg kinematics and fault-prone contact detection. Even though the experiments done in this study are not exactly the same as that done by Bloesch et al. [2], it can be

noted that the drift in the position estimation is less than what was recorded in [2]. An accurate kinematic model as well as the use of force sensors to detect the ground contact is notable improvements implemented in this study that can account for a smaller drift.

In order to validate the Z-axis position state estimation, a third experiment was conducted. Here, the robot's feet were kept at one position while its body moved up and down. By keeping the feet still, the vibrations of the robot were decreased. Fig 7.8 shows the comparison between the estimated z position and the z position outputs of the Vicon system.

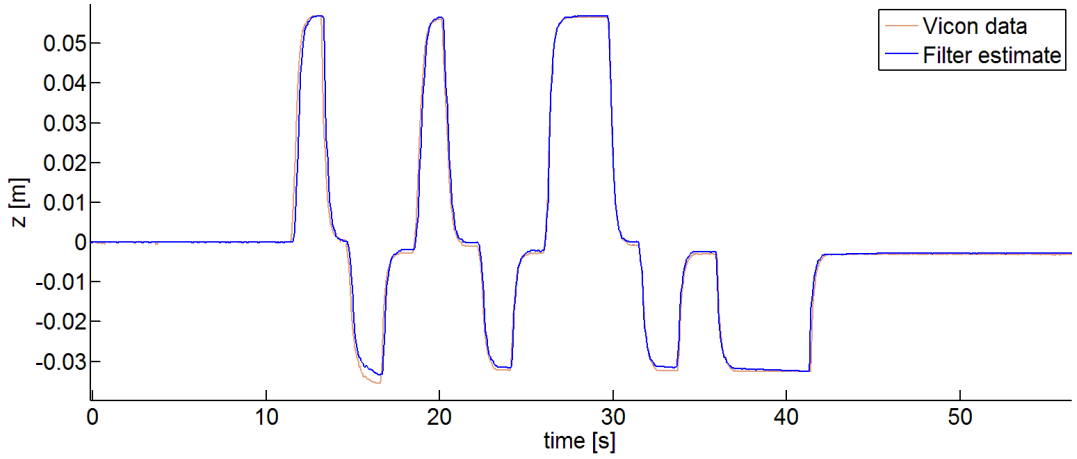

Figure 7. 8: Comparison between the estimated z position and the z position outputs of the Vicon system.

From Fig. 7.8 one can conclude that the movement of the robot body alone can be tracted very accurately. This is further verified when one examines the Z-axis velocity estimation of the same experiment. Fig. 7.9 shows the comparison between the estimated z velocity and the z position's numerical derivatives of the Vicon system's output. The resulting RMS error value of this comparison is $0.0186\ \mathrm{m/s}$, showing that the velocity can be tracked very accurately.

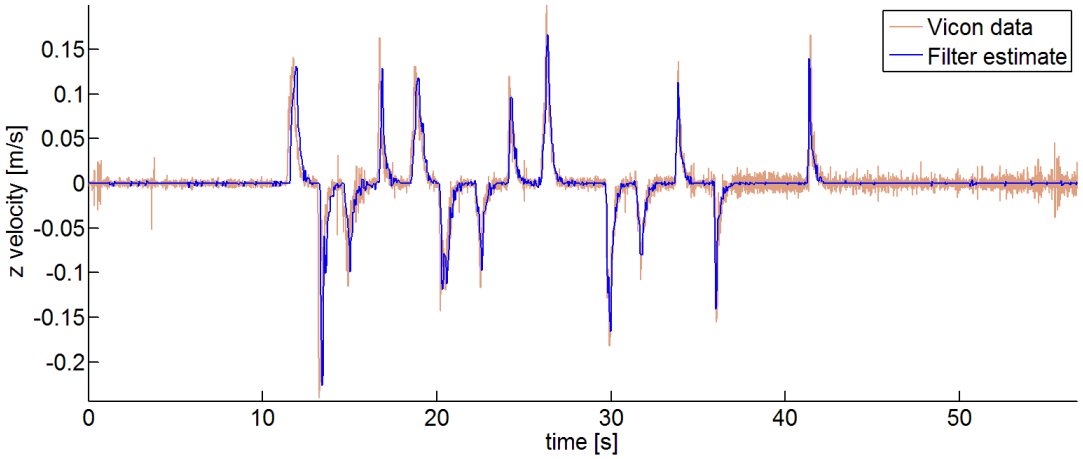

Figure 7. 9: Comparison between the estimated *Z* axis velocity and the numerical z-position derivatives of the Vicon output.

Next, an experiment was conducted to investigate the yaw, pitch and roll estimations when only the body is moving. Here, the robot body performed a set of clockwise and anti-clockwise turns followed by a set of forward and backward tilting and ended with a set of sideways tilting. Fig. 7.10 shows the comparison between the estimated yaw, pitch and roll angles and the Vicon system's orientation outputs. This experiment validated very precise estimation for the robot body moving with the angular RMS error 0.0138 rad for the yaw, 0.0069 rad for the pitch, and 0.0119 rad for the roll.

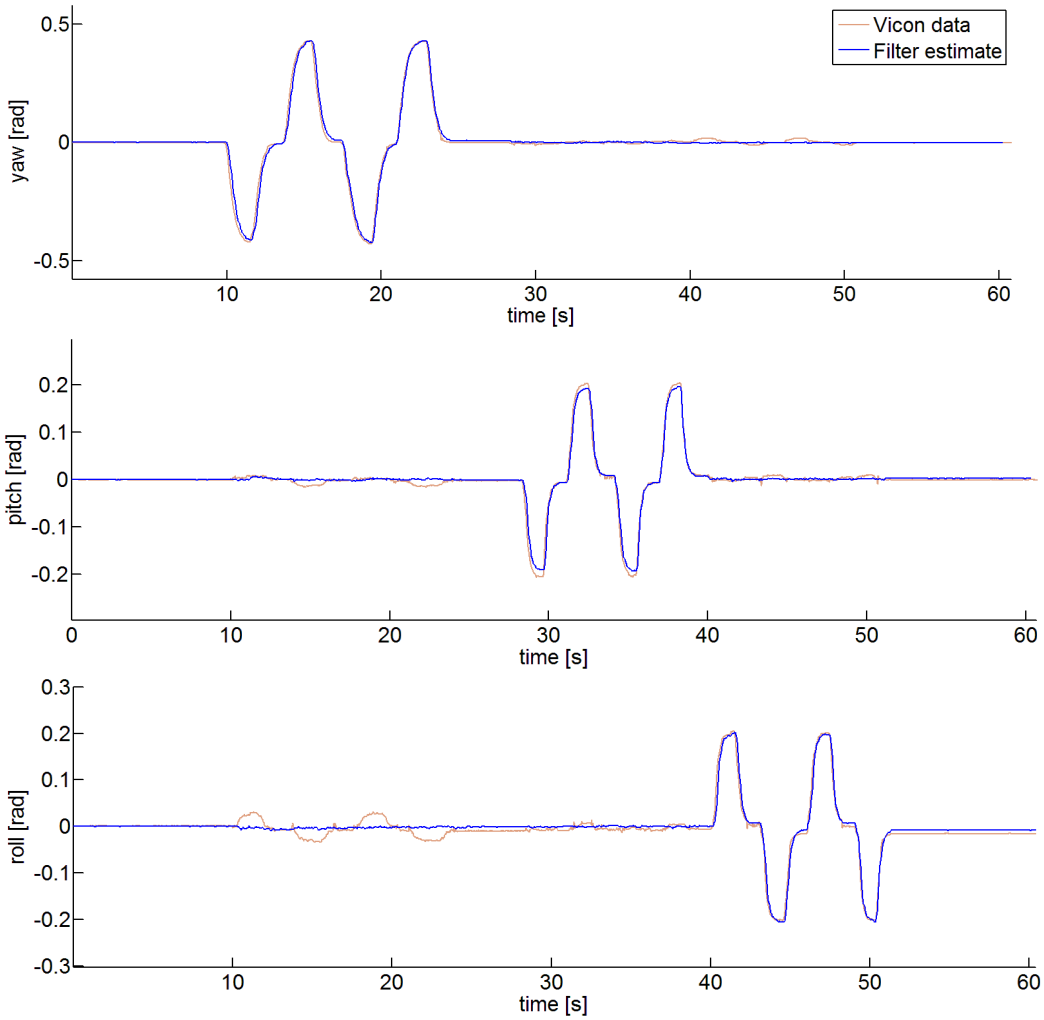

Figure 7. 10: Comparison between the estimated yaw, pitch and roll angles and the orientation outputs of the Vicon system.

Since the yaw isn't fully observable, a drift in the yaw estimation is expected while the robot is navigating. The following two experiments were conducted to investigate any possible drift in the yaw estimation. In both experiments the robot navigated on even terrain producing multiple turns using ripple gait. In the first experiment the angles of the turns were small (less than $90°$). Fig. 7.11 shows the comparison between the estimated yaw and the Vicon system's yaw output for this experiment. The comparison between the estimated position and the Vicon system's position outputs is also

provided as context. With this experiment an angle RMS error of $0.136\ \text{rad}$ was recorded for the yaw.

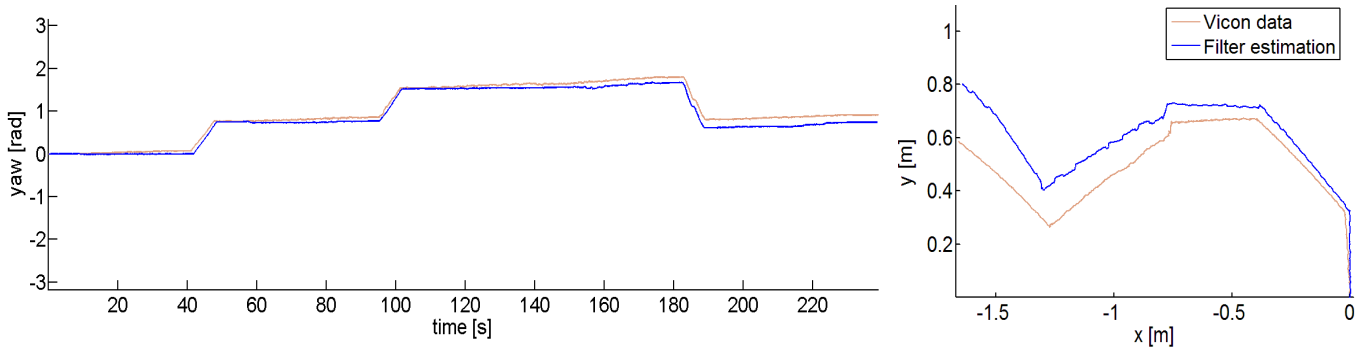

Figure 7. 11: Comparison between the estimated yaw and position and the Vicon system's yaw and position outputs for small turns by the robot.

In the second experiment the angles of the turns were large (more than $90°$). Fig. 7.12 shows the comparison between the estimated yaw and the Vicon system's yaw output for the second experiment. Again, the comparison between the estimated position and the Vicon system's position outputs is also provided. With this experiment the angle RMS error of the yaw was $0.0946\ \text{rad}$. From the experiments shown in Fig. 7.11 and Fig. 7.12, it can be concluded that the yaw drift in the estimation is very small and almost unnoticeable.

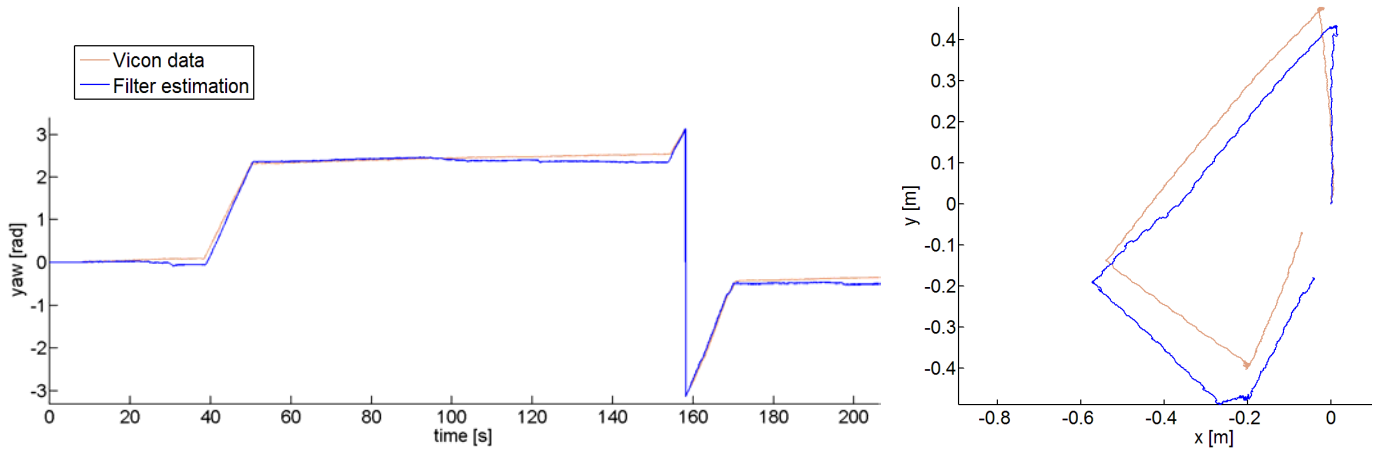

Figure 7. 12: Comparison between the estimated yaw and position and the Vicon system's yaw and position outputs for large turns by the robot.

In order to validate the velocity estimations when the robot is navigating, two experiments using different gaits were conducted. Fig 7.13 shows the comparison between the estimated velocity and the Vicon system's numerical position derivatives for the robot navigating just over 4 m using ripple gait. Fig 7.14 shows the same comparison for the robot navigating with tripod gait.

Because all three axis velocity estimates are fully observable, the velocity can be tracked very accurately. This is validated with the resulting RMS error values that are summarised in Table 7.1.

Table 7. 2: RMS error values for ripple and tripod gait velocities.

	RMS error [m/s]	
Axis velocity [m/s]	Ripple gait experiment	Tripod gait experiment
x	0.034	0.079
y	0.0427	0.0689
z	0.0258	0.0452

A notable source for the higher RMS error values for the tripod gait compared to the ripple gait is again due to the increased vibrations of the robot when navigating using tripod gait. The RMS error values recorded in these experiments are comparable to the results published in [2].

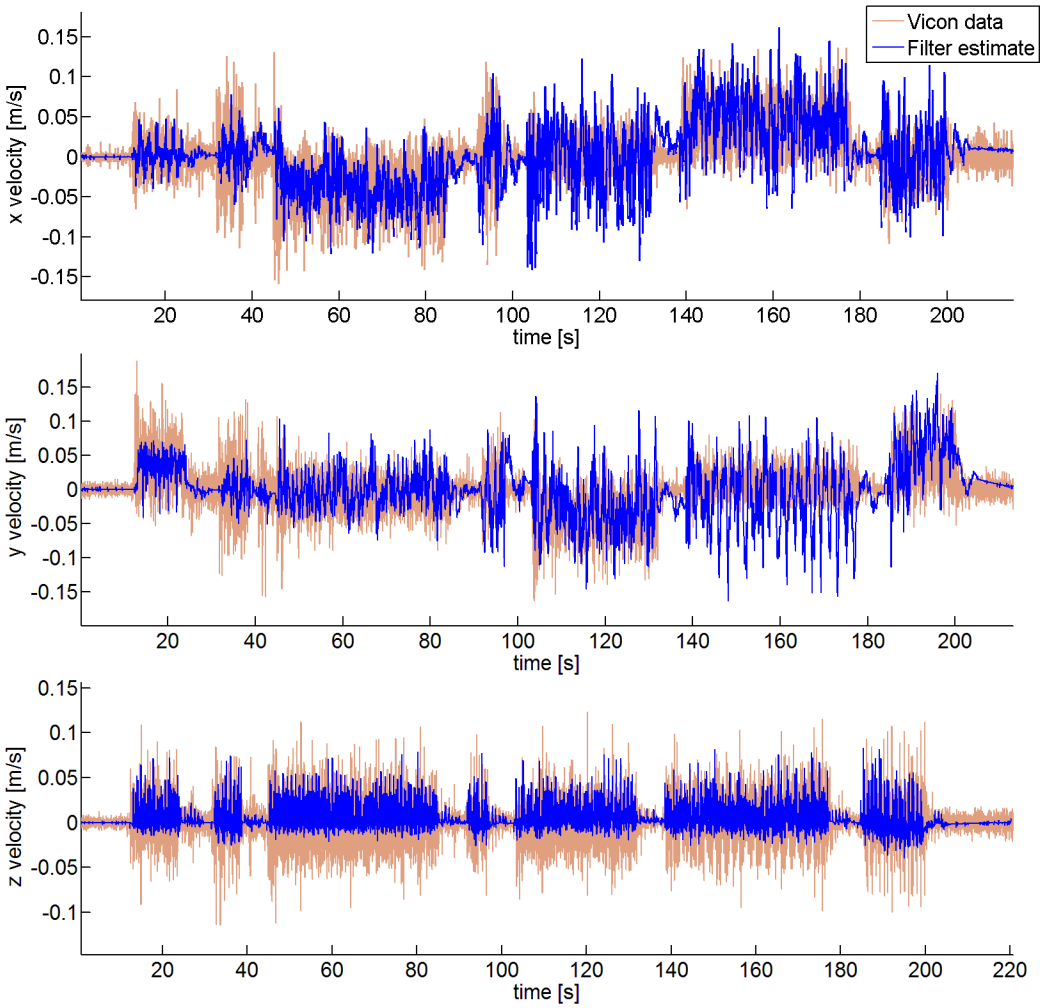

Figure 7. 13: Comparison between the estimated velocity and the Vicon system's numerical position derivatives for the robot navigating using ripple gait.

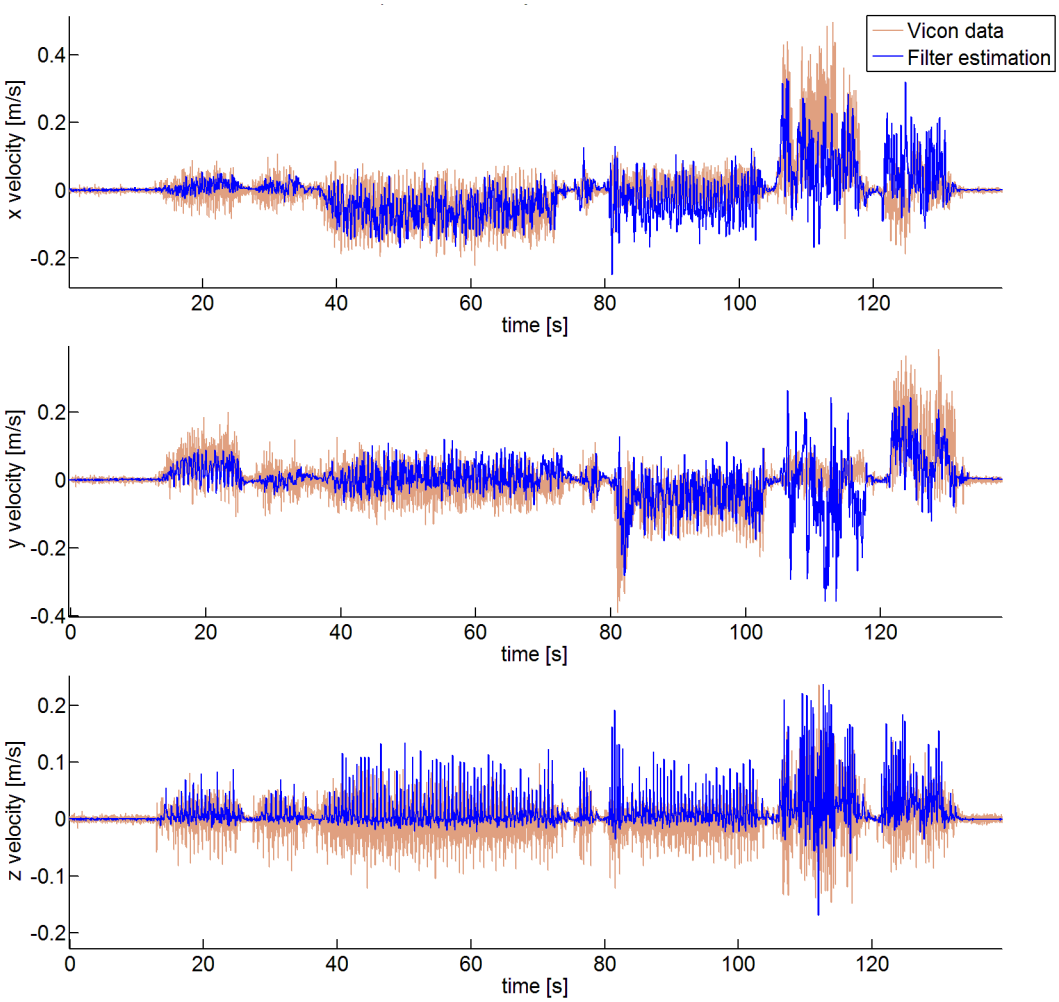

Figure 7. 14: Comparison between the estimated velocity and the Vicon system's numerical position derivatives for the robot navigating using tripod gait.

For the experiment shown in Fig. 7.13, where the robot is navigating in ripple gait, the comparison between the position estimates and the Vicon system's position outputs are provided in Fig. 7.15. Fig. 7.15 includes the foot position estimates for leg one, four and five, as defined by Fig. 4.8. This figure shows how the robot actions can accurately be tracked by following the foot position estimates. The robot's starting position is with its centre of body position at $\boldsymbol{r} = [0,0,0]$. From the positions of the feet, one can determine that the robot is facing forward in the positive y direction.

The robot's movements can now be derived from Fig 7.15 as follows:

- The robot walked forward for ± 0.4 m,
- then turned just over $90°$ anti-clockwise,
- walked forward for ± 1.5 m,
- turned just under $90°$ anti-clockwise,
- walked forward for ± 1 m,
- waked sideways (left) for ± 1.5 m,

- and ended by walking backwards $\pm$ 0.6 m.

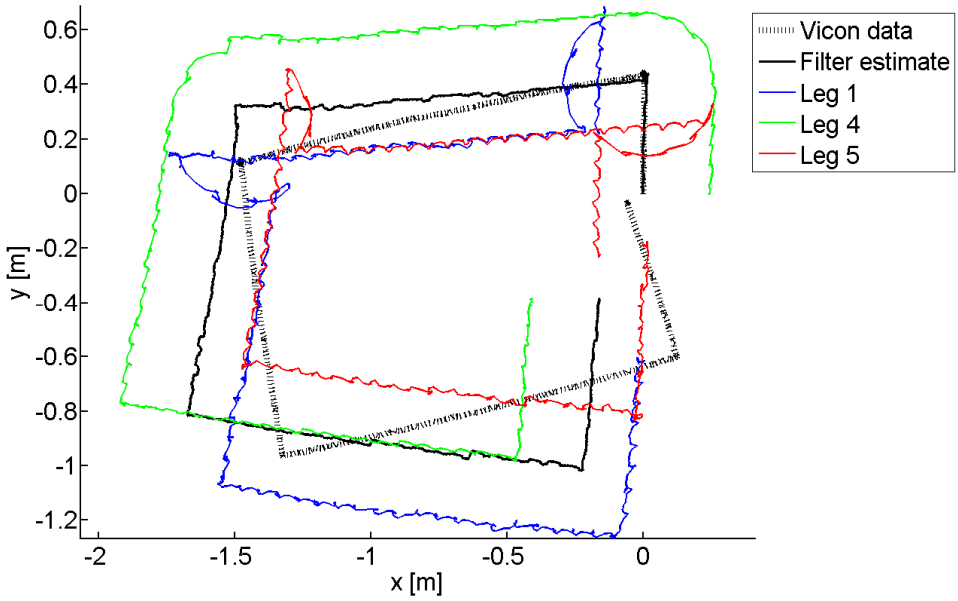

Figure 7. 15: Comparison of the position estimation of the centre of body and feet of leg 1, 4 and 5, and the Vicon system's position outputs for the centre of the robot body.

From the results it was shown that even though the position and yaw isn't fully observable, only a slight drift was recorded in the position estimates and the yaw drift showed to be almost unnoticeable. It was further shown that the velocity, pitch and roll can be tracked very accurately. From the results of all the experiments conducted, the state estimation approach implemented in this study was validated.

7.5 Conclusion

This chapter discussed the implementation and results for the conducted study. The kinematic model derived in Chapter 4 was verified by comparing its outputs to the foot positions of a computer assembly model of the robot platform. A small error, about 2 mm in the X-axis calculation of the leg kinematic model, was found. This error is caused by the round foot end of the robot and was included in the kinematic noise parameter, $\boldsymbol{n}_{s,i}$, verifying the kinematic model.

The implementation of the state estimation equations derived in Chapter 6 was discussed next. Here, the implementation of the EKF in Matlab® was explained by providing and discussing the main program's architecture. The initial noise parameters of the EKF were also derived. In order to compensate for inaccuracies in the filter model, the initial noise parameters were empirically tuned until the EKF provided the best results. The final noise parameters used in the filter were provided in

Table 7.1. The discussion on the implementation of the state estimation concluded with the derivation of the initial state vector and covariance matrix needed by the EKF.

Lastly, the state estimation results were discussed. Numerous experiments were conducted where the state estimation outputs of the robot platform were compared to a ground truth measurements taken by a Vicon system. As the control of the robot is out of the scope of this study, these experiments were conducted with a limited control approach on relatively even terrain. Even though it was verified that the state estimation does not depend on specific locomotion gaits, increased vibrations of the robot for certain gaits caused by the robot control, influenced the estimation results. As result, the drift in the position estimation for ripple gait was less than for tripod gait. For both locomotion gaits, the position drift noticed was under $9\ \%$, less than what was recorded in [2].

With an experiment where the robot body was tilted and turned, the estimation of the yaw pitch and roll was validated. Here, angular RMS errors of less than $0.01\ \mathrm{rad}$ was recorded. Since the yaw isn't fully observable, further experiments were conducted where the yaw drift was investigated for the robot navigating with smaller and larger turns. It was concluded that the yaw drift is very small and almost unnoticeable. The velocity estimation were evaluated with two experiments where the robot was navigating randomly using ripple and tripod gaits. For the ripple gait, RMS errors of less than $0.04\ \mathrm{m/s}$ were recorded. For the tripod gait, RMS errors of less than $0.08\ \mathrm{m/s}$ were recorded. These experiments showed that the velocity can be accurately tracked. The state estimation results concluded by showing how the robot's actions can be tracked by considering the estimation of the foot positions together with the estimation of the centre of the robot body.

All of the experiments conducted showed comparable results to those found by Bloesch et al.[2]. With the validation of the state estimation for the hexapod robot using only proprioceptive sensors, this study concludes.

Chapter 8: Conclusion and future work

"Imagination is more important than knowledge.

Knowledge is limited. Imagination encircles the world."

~ *Albert Einstein*

8.1 Summary of work done

This study started with a need identified for the development of a robot that can operate in almost any land-based environment. In Chapter 2 research focussed and directed this need to the problem statement of this study: the development of a state estimation approach for a hexapod platform using only proprioceptive sensors. Through a literature study presented in Chapter 3, a commercial hexapod robot and common proprioceptive sensors were acquired. A framework for the state estimation of the hexapod platform was also identified. The framework was based on the fusion of the robot's kinematics with inertial sensor data. Hereafter, the sensory devices were integrated onto the hexapod robot to develop the robot platform used to validate this study.

It was identified that the state estimation framework will require a kinematic model of the robot platform. Therefore, in Chapter 4 a kinematic model for the robot platform was derived. This was done using the Denavit-Hartenberg notation. As no measurement details about the hexapod robot is provided by the manufacturers, this derivation is seen as a contribution made by this study. A measurement model for the kinematic model, needed by the state estimation, was also derived.

In Chapter 5 all of the sensory devices needed for the state estimation were discussed. The data acquisition method was also discussed and implemented. To account for errors in the sensor measurements, measurement models were derived that were used in the state estimation equations. The state estimation framework presented by Bloesch et al. [2] was then adopted for the hexapod platform. The state estimation methodology and the derivation of the state estimation equations were discussed in Chapter 6. All of the state estimation equations were derived for the hexapod platform in order to provide six degrees of freedom information about the robot base. In addition, the foot positions of the robot were also estimated and force sensors in the robot's feet were used to provide ground contact status.

The state estimation equations were then implemented in Matlab® for evaluation. This was discussed in Chapter 7. Initial noise parameters were derived for the EKF. With the robot recording sensor data,

a few simple experiments were used to derive an initial state vector and covariance matrix needed by the EKF. These experiments were also used to empirically tune the noise parameters until the EKF provided the most accurate state estimation. Final experiments were then conducted to compare the state estimation results with ground truth measurements. The state estimation approach was then validated.

8.2 Evaluation of state estimation approach

In this study a state estimation framework was successfully used to develop a state estimation methodology and derive state estimation equations for a hexapod platform. The state estimation methodology implemented uses an EKF to fuse the robot kinematics with IMU measurements. The filter can handle any gait as well as unstructured terrain with the assumption of limited foot slippage. It estimates the position, velocity and orientation at the robot's centre. This results in a full six degrees of freedom pose estimation of the robot base. As mentioned in Chapter 2, a six degrees of freedom pose estimation is especially important for the stability control of legged robots navigating in unstructured terrain.

Furthermore, the positions of the feet of the robot and the bias quantities of the IMU is also estimated. The state estimation approach can also be interpreted as a simultaneous localisation and mapping algorithm, where the estimated foot contact positions can be used to build a map. The use of only proprioceptive sensors as input to the state estimator is important. This will allow the robot to be controlled without having to rely on exteroceptive sensors such as a GPS or camera.

The state estimation approach was verified and validated in Chapter 7. Even though the absolute position is not fully observable, a drift in the position estimate of less than $5\,\%$ of the distance travelled was recorded when ripple gait was used for the robot's locomotion. This drift percentage is lower than recorded by Bloesh et al. [2]. The inclusion of the force sensors for ground detection and an accurate kinematic model are notable sources for this improvement. The estimation of the velocity of the robot base was very precise yielding RMS error values of less than $0.04\ \mathrm{m/s}$ for the robot using ripple gait. The roll and pitch estimations was also very precise and the expected yaw drift showed to be almost unnoticeable. These results are all comparable to those found by Bloesch et al. [2]

When evaluating the state estimation approach, one can conclude that it can easily be implemented on low-cost commercially available hexapod robots using common low-cost sensory devices. Its accuracy is ideal for further research and the development of control algorithms and robotic applications.

8.3 Improvements and future work

In order to improve the current state estimation methodology the inclusion of measurements of the forces acting on the legs of the robot can be considered. By adding leg force estimations, the operating safety of the servo motors can be monitored. This can provide vital information, especially when the robot is navigating autonomously in an unstructured environment.

In the paper “Neural virtual sensors for terrain adaptation of walking machines.” presented by Estremera et al. [62] a virtual force sensor is presented. The virtual force sensor uses sensory information from joint position feedback to eliminate the need for physical force sensors in the robots feet. The research done by Estremera et al. [62] let to the following hypothesis with regards to improvements and future work.

By comparing the full body estimate with the force information from the force sensors, a virtual sensor can be developed that will estimate the forces in the body and the ground contact of the feet. After a virtual force sensor is designed and trained the physical force sensors in the feet of the hexapod can be eliminated from the robot design. This will result in a state estimation that makes use of more sensory information than the one presented by Bloesch et al. [2] but has the same amount of physical sensors.

Future work can also include handling the absolute position and yaw estimations that isn’t fully observable. Apart from the triaxial accelerometer and the triaxial gyroscope, the IMU used in this study also has a triaxial magnetometer. By including the magnetometer measurements in the state estimation algorithms, one can expect a reduction in the yaw drift noticed in the current estimation approach.

It is important to note that the state estimation for a legged robot should only rely on proprioceptive sensors for stability control. However, by including measurements from a GPS, the absolute position can be estimated. The estimation will therefore still only rely on the proprioceptive sensors but an additional exteroceptive sensor can be used to correct the robots absolute position whenever needed.

Possible future work with regard to the robot platform include the development of a control approach that uses the state estimation as derived in this study. This will allow further testing of the state estimation approach as well as development toward an end application. Since the platform is classified as low-cost, it can easily be replaced. Therefore, the platform can be sent into dangerous situations. End applications of the robotic platform is mainly focussed on search and rescue missions.

8.4 Conclusion

The objective of this study was to develop and implement a state estimation approach for a hexapod robot that only relies on proprioceptive sensors. The approach had to be easily implemented on a low-cost commercially available hexapod robot with common low-cost sensors. From the results it is shown that such an approach was developed and successfully implemented.

The state estimation approach was validated and can now be used to develop and test control algorithms for hexapod robots.

APPENDIX

Appendix A: Code

Matlab code

In order to verify and validate the state estimation methodology derived in this study, the state estimation equations were implemented in Matlab®. All of the Matlab® code is available on the dissertation cd in the "Matlab code" folder. The code is commented in detail with the function names corresponding to the discussion in Chapter 7.

Arduino code

This section discusses the open-source "*PhantomX Hexapod Phoenix Code*" firmware and the modifications that were made to the firmware code for the control of the robot platform used in this study. The open-source firmware along with detailed documentation on how to implement it can be found at [88].

Compared to the original firmware supplied by the distributers of the PhantomX hexapod, the Phoenix code provide life-like walking gaits and much more features. Some of the features used in this study include: translate mode, rotate mode, speed control, Z- axis control and a variety of different gait options. The specific firmware version used in this study can be found in the "Arduino code" folder included in the dissertation cd.

Two modifications were implemented in the firmware code. The first addressed the servo motor's position feedback needed for the state estimation developed in this study. Here, a timer was implemented in order to send out the servo positions every $50\ \mathrm{ms}$. This was done by reading the present position value in the "AX_PRESENT_POSITION_L" register of each Dynamixel servo motor's microcontroller into an array. The second modification involved the implementation of a software serial library in order to communicate the position feedback array to the UDOO single board computer used to capture all the sensor data.

In the "Arduino code" folder, the executable program named "PhantomX_V2_Commander-_AX12_Stock_Rev_a" was loaded as firmware onto the robot platform for this study. In "Phoenix_Code.h" the "SoftwareSerial.h" and the "SimpleTimer.h" files were included and a software

serial named “mySerial”, was opened at 115200 baud rate. In “Phoenix_Driver_AX12.h” the “SoftwareSerial.h” and the “SimpleTimer.h” files were included again and the RX and TX hardware pins for “mySerial” was assigned. These pins were physically connected to input pins on the UDOO to create the serial communication line. A timer named “timer” was also declared and a function named “BeenPos” was included. This function reads all 18 servo positions into an array and sends it out on the software serial line. The “BeenPos” function is called every 50 ms by the timer.

Python code

This section expands on the discussion provided in Chapter 5 about the executable program used to acquire and collect the sensory data from the sensory devices. The program was implemented in Python IDE on the UDOO single board computer that was integrated onto the robot platform. The complete program code is included on the dissertation cd in the folder “Python code”.

The program starts by entering a *WHILE loop* that monitors if the sensor data collection should start. The start and stop condition for the program is controlled by a hardware button that is connected to a general in-out pin (gpio) with identification number 123, of the UDOO. Whenever the push button is triggered, the register value of the pin it is connected to change from 0 to 1. In the *WHILE loop* the register of this pin is constantly opened and read until its value is 1. The following lines of code implements the opening and reading of the register:

```
button_read = open("/sys/class/gpio/gpio123/value",'r')
val = button_read.read(1)
```

Here, “/sys/class/gpio/gpio123/value" is the directory to the pin-123, and 'r' opens this directory in *read* mode. When “val” is equal to 1, the following is implemented in an *IF* condition: Firstly, an LED connected to gpio56 is turned on for visual conformation to the person operating the platform. This is implemented by opening the directory of gpio56 in *write* mode, ‘w’, and writing the value 1 in it:

```
led_on =  open("/sys/class/gpio/gpio56/value",'w')
led_on.write('1')
```

For conformation in the operating system on the UDOO, the program also writes “BEGIN” to the Python IDE:

```
print("BEGIN")
```

Hereafter, the setup of serial communication with the IMU is implemented. The 3DM-GX3-25 device was connected to one of the USB ports on the UDOO. In the *WHILE* loop the communication with the USB port is established by calling the function “open_Inertial()”. This function uses a serial library to

communicate with the 3DM-GX3-25 device. The communication protocol of the 3DM-GX3-25 can be found on the MicroStrain website [80]. The serial communication between the UDOO and the IMU was established with the following code:

```
def open_Inertial():
    global inertial
    inertial = serial.Serial(
        port='/dev/ttyACM0',
        baudrate=115200,
        parity=serial.PARITY_NONE,
        stopbits=serial.STOPBITS_ONE,
        bytesize=serial.EIGHTBITS,
        timeout=1
    )
    inertial.close()
    inertial.open()
    return inertial
```

Next, the serial communication needed in order to read the servo positions send through a software serial communication protocol from the ArbotiX board to the UDOO was established. The output from the ArbotiX board was connected to the “ttymxc3” port on the UDOO. The following code was used to establish communication with this port:

```
def open_Serial():
    global ser
    ser = serial.Serial(port='/dev/ttymxc3',
        baudrate=115200,
        parity=serial.PARITY_NONE,
        stopbits=serial.STOPBITS_ONE,
        bytesize=serial.EIGHTBITS,
        timeout=1
    )
    ser.close()
    ser.open()
    return ser
```

After the serial communication setup was done, a text file was created in which all the sensory data will be stored and the *WHILE* loop was exited. A second *WHILE* loop was then entered. In this loop the end of the program condition is monitored. The *WHILE* loop starts by again investigating the value of gpio123. This time, a value of 1, created if the push button on the robot is triggered, indicates that the data collection should stop. If a value of 1 is recorded, the output in gpio56 is set to 0, turning the LED connected to gpio56 off. The word "END" is also written in the Python IDE and the program closes.

While the value in gpio123 is not 1, the servo motor position feedback is read with the function "get_Servos()". This function reads the 18 servo positions and combines them into a string that is returned. The function makes use of another function called "readlineCR()" to search for the end of the array, indicated by the character "\r", as send from the ArbotiX board. The code for the "readlineCR()" function follows:

```
def readlineCR(self):
    eol = b'\r'
    leneol = len(eol)
    line = bytearray()
    while True:
        c = self.read(1)
        if c:
            line += c
            if line[-leneol:] == eol:
                break
        else:
            break
    return bytes(line)
```

The code for the "get_Servos()" function follows:

```
def get_Servos():
    global str_s
    str_servo = ''
    str_s = readlineCR(ser)
    ser.flushInput()
    b_a = bytearray(str_s)
    x = 0
```

```
        while x < 18 :
            str_servo = str_servo + str(b_a[x]) + ','
            x = x + 1
        a_bytes = str_s
        a_bytes = (' '.join(["{0:b}".format(x) for x in a_bytes]))
        return str_servo
```

After the servo positions are collected, another *WHILE* loop is entered. In this loop the remaining sensor data is collected. First all of the IMU data is read with the “get_Inertial_data()” function. From the data communication protocol of the IMU it was established that the characters “ue” indicated the *end of line* and a total of 56 characters will be send to the UDOO containing the IMU measurements. The IMU measurements were read into a string called “str_i” and returned. Hereafter, the inertial measurements string was converted into an array containing hex values.

Following the data communication protocol as set out by MicroStrain, the array, called “bytes_s”, was then used to obtain the internal time stamp of the IMU, the acceleration measurement, the angular rate measurement and the quaternion measurement. Each of these quantities were calculated with different functions that uses an *offset* value as input. The offset value indicates the start position in the array where the values that are needed to calculate a specific quantity can be found.

For the time stamp, the offset value is 52. The time stamp was calculated with the following function:

```
    def get_Time(offset):
        x_binary = ""
        y_binary = ""
        z_binary = ""
        xyz = offset
        time1 = (int(str_i[xyz]))
        time1 = time1 * (pow(255,3))
        time2 = (int(str_i[xyz+1]))
        time2 = time2 * pow(255,2)
        time3 = (int(str_i[xyz+2]))
        time3 = time3 * (255)
        time4 = (int(str_i[xyz+3]))
        time_stamp = time1 + time2 + time3 + time4
        time_stamp = (time_stamp)/62500
```

```
        return str(time_stamp)
```

For the acceleration measurement the offset is 6, and for the angular rate measurement the offset is 20. The function that was used to calculate the acceleration measurement and the angular rate measurement follows:

```
def get_Acc(str_i,offset):
    x_binary = ""
    y_binary = ""
    z_binary = ""
    xyz = offset
    while xyz < (offset+13):
        if xyz < (offset+4):
            x_binary = x_binary + dec_to_bin(int(str_i[xyz]))
        else:
            if (xyz >= (offset+4)) and (xyz< offset+8):
                y_binary = y_binary + dec_to_bin(int(str_i[xyz]))
            else:
                z_binary = z_binary + dec_to_bin(int(str_i[xyz]))
        xyz = xyz + 1
    x_Val = get_Value(x_binary)
    y_Val = get_Value(y_binary)
    z_Val = get_Value(z_binary)
    return_val = str(x_Val) + ',' + str(y_Val) + ',' + str(z_Val)
    return str(return_val)
```

The offset for the quaternion measurement is 34. The quaternion measurement is calculated with the following function:

```
def get_Quad(str_i,offset):
    q_0 = ""
    q_1 = ""
    q_2 = ""
    q_3 = ""
    xyz = offset
    while xyz < (offset+17):
```

```
            if xyz < (offset+4):
                q_0 = q_0 + dec_to_bin(int(str_i[xyz]))
            else:
                if (xyz >= (offset+4)) and (xyz< offset+8):
                    q_1 = q_1 + dec_to_bin(int(str_i[xyz]))
                else:
                    if (xyz >= (offset+8)) and (xyz< offset+12):
                        q_2 = q_2 + dec_to_bin(int(str_i[xyz]))
                    else:
                        q_3 = q_3 + dec_to_bin(int(str_i[xyz]))
            xyz = xyz + 1
        q0_Val = get_Value(q_0)
        q1_Val = get_Value(q_1)
        q2_Val = get_Value(q_2)
        q3_Val = get_Value(q_3)
        return_val = str(q0_Val) + ',' + str(q1_Val) + ',' + str(q2_Val)+ ',' +
    str(q3_Val)
        return str(return_val)
```

After all the inertial measurements were collected the foot contact status was collected. The force sensors in the robot's feet were integrated into a circuit, given in Appendix B, to provide the ground contact status. For each robot leg, the ground contact status was sent to a gpio pin on the UDOO. The following is a summary of the specific gpio pin assigned for each leg:

- Leg one: gpio134
- Leg two: gpio127
- Leg three: gpio140
- Leg four: gpio125
- Leg five: gpio138
- Leg six: gpio136

The registers of all of these pins were read and their values were used to indicate the ground contact status. All of the inertial measurements, the servo position measurements and the ground contact status were then written in the text file.

Appendix B: IMU datasheet [74]

LORD PRODUCT DATASHEET

3DM-GX3® -25

Miniature Attitude Heading Reference System

The **3DM-GX3®** -25 is a high-performance, miniature Attitude Heading Reference System (AHRS), utilizing MEMS sensor technology. It combines a triaxial accelerometer, triaxial gyro, triaxial magnetometer, temperature sensors, and an on-board processor running a sophisticated sensor fusion algorithm to provide static and dynamic orientation, and inertial measurements.

Features & Benefits

Best in Class

- precise attitude estimations
- high-speed sample rate & flexible data outputs
- high performance under vibration and high *g*

Easiest to Use

- smallest, lightest industrial AHRS available
- simple integration supported by SDK and comprehensive API

Cost Effective

- reduced cost and rapid time to market for customer's applications
- aggressive volume discount schedule

Applications

Accurate guidance, orientation and positioning under dynamic conditions such as:

- Inertial Aiding of GPS
- Unmanned Vehicle Navigation
- Platform Stabilization, Artificial Horizon
- Antenna and Camera Pointing
- Health and Usage Monitoring of Vehicles
- Reconnaissance, Surveillance, and Target Acquisition
- Robotic Control
- Personnel Tracking

System Overview

The **3DM-GX3®** -25 offers a range of fully calibrated inertial measurements including acceleration, angular rate, magnetic field, deltaTheta and deltaVelocity vectors. It can also output computed orientation estimates including Euler angles (pitch, roll, and heading (yaw)), rotation matrix and quaternion. All quantities are fully temperature compensated and are mathematically aligned to an orthogonal coordinate system. The angular rate quantities are further corrected for g-sensitivity and scale factor non-linearity to third order. The 3DM-GX3® -25 architecture has been carefully designed to substantially eliminate common sources of error such as hysteresis induced by temperature changes and sensitivity to supply voltage variations. Gyro drift is eliminated in AHRS mode by referencing magnetic North and Earth's gravity and compensating for gyro bias. On-board coning and sculling compensation allows for use of lower data output rates while maintaining performance of a fast internal sampling rate. For those users, integrators or OEMs who develop their own orientation and navigation applications, the 3DM-GX3® -25 is shipped with a complete Data Communications Protocol guide that provides access to the powerful LORD MicroStrain® Inertial Packet Protocol (MIP). Applications of your own design can readily be developed in any coding language and on any computing platform including microprocessors. The 3DM-GX3® -25 is initially sold as a starter kit consisting of an AHRS+GPS module, RS-232 or USB communication and power cable, software CD, user manual and quick start guide.

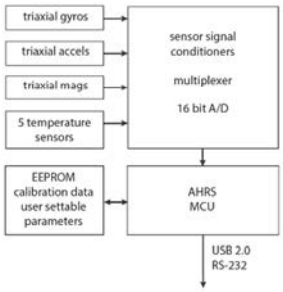

best of sensors expo 2009
Silver Level Winner

LORD MicroStrain®
SENSING SYSTEMS

3DM-GX3® -25 Miniature Attitude Heading Reference System

Specifications

AHRS Specifications

Attitude and Heading	
Attitude heading range	360° about all 3 axes
Accelerometer range	±5*g* standard
Gyroscope range	±300°/sec standard
Static accuracy	±0.5° pitch, roll, heading typical for static test conditions
Dynamic accuracy	±2.0° pitch, roll, heading for dynamic (cyclic) test conditions and for arbitrary angles
Long term drift	eliminated by complimentary filter architecture
Repeatability	0.2°
Resolution	<0.1°
Data output rate	up to 1000 Hz
Filtering	sensors sampled at 30 kHz, digitally filtered (user adjustable) and scaled into physical units; coning and sculling integrals computed at 1 kHz
Output modes	acceleration, angular rate, and magnetic field deltaTheta, deltaVelocity, Euler angles, quaternion, rotation matrix
General	
A/D resolution	16 bits SAR oversampled to 17 bits
Interface options	USB 2.0 or RS232
Baud rate	115,200 bps to 921,600 bps
Power supply voltage	+3.2 to +16 volts DC
Power consumption	80 mA @ 5 volts with USB
Connector	micro-DB9
Operating temperature	-40° C to +70° C
Dimensions	44 mm x 24 mm x 11 mm - excluding mounting tabs, width across tabs 37 mm
Weight	18 grams
ROHS	compliant
Shock limit	500 *g*
Software utility	CD in starter kit (XP/Vista/Win7/Win8 compatible)
Software development kit (SDK)	complete data communications protocol and sample code

Senror Specifications

	Accels	Gyros	Mags
Measurement range	±5 *g*	±300°/sec	±2.5 Gauss
Non-linearity	±0.1 % fs	±0.03 % fs	±0.4 % fs
In-run bias stability	±0.04 mg	18°/hr	—
Initial bias error	±0.002 *g*	±0.25°/sec	±0.003 Gauss
Scale factor stability	±0.05 %	±0.05 %	±0.1 %
Noise density	80 µg/√Hz	0.03°/sec/√Hz	100 µGauss/√Hz
Alignment error	±0.05°	±0.05°	±0.05°
User adjustable bandwidth	225 Hz max	440 Hz max	230 Hz max
Sampling rate	30 kHz	30 kHz	7.5 kHz max
Options			
Accelerometer range	±1.7 *g*, ±16 *g*, ±50 *g*		
Gyroscope range	±50°/sec, ±600°/sec, ±1200°/sec		

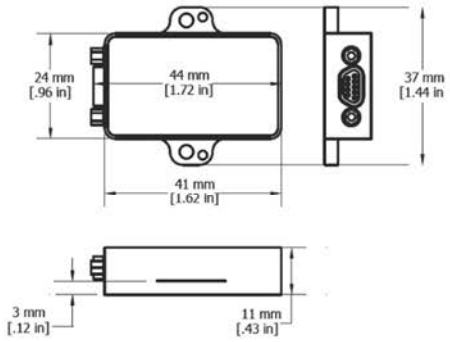

8400-0033 rev. 003

LORD Corporation
MicroStrain® Sensing Systems
459 Hurricane Lane,
Suite 102
Williston, VT 05495 USA
www.microstrain.com
ph: 800-449-3878
fax: 802-863-4093
sales@microstrain.com
Patent Pending

Appendix C: Force Sensors

Data sheet [73]

FlexiForce®
Standard Force & Load Sensors Model # A201

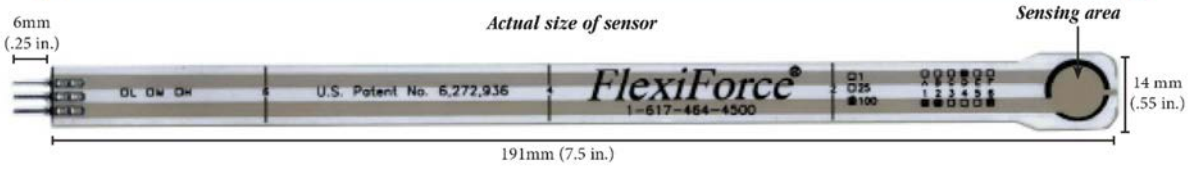

Physical Properties

Thickness	0.203 mm (0.008 in.)
Length	191 mm (7.5 in.)*
	optional trimmed lengths: 152 mm (6 in.), 102 mm (4 in.), 51 mm (2 in.)
Width	14 mm (0.55 in.)
Sensing Area	9.53 mm (0.375 in.) diameter
Connector	3-pin Male Square Pin (center pin is inactive)
Substrate	Polyester (ex: Mylar)
Pin Spacing	2.54 mm (0.1 in.)

✓ **ROHS Compliant**

** Length does not include pins, please add approximately 6mm (0.25 in.) for pin length for a total length of approximately 197 mm (7.75 in).*

Standard Force Ranges (as tested with circuit shown below)

0 - 1 lb. (4.4 N)
0 - 25 lb. (111 N)
0 - 100 lb. (445 N)

In order to measure forces above 100 lb (up to 1000 lb), apply a lower drive voltage (-0.5 V, -0.10 V, etc.) and reduce the resistance of the feedback resistor (1kΩ min.) Conversely, the sensitivity can be increased for measurement of lower forces by increasing the drive voltage or resistance of the feedback resistor.

Recommended Circuit

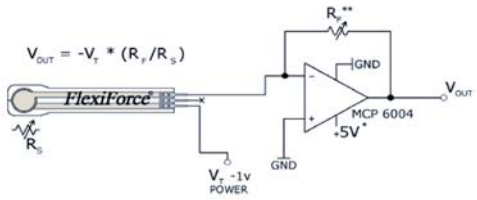

- * Supply Voltages should be constant
- ** Reference Resistance R_F is 1kΩ to 100kΩ
- Sensor Resistance R_S at no load is >5MΩ
- Max recommended current is 2.5mA

Typical Performance Evaluation Conditions

Linearity (Error)	< ±3%	Line drawn from 0 to 50% load
Repeatability	< ±2.5% of full scale	Conditioned sensor, 80% of full force applied
Hysteresis	< 4.5 % of full scale	Conditioned sensor, 80% of full force applied
Drift	< 5% per logarithmic time scale	Constant load of 25 lb (111 N)
Response Time	< 5µsec	Impact load, output recorded on oscilloscope
Operating Temperature	-40°F - 140°F (-40°C - 60°C)	*Time required for the sensor to respond to an input force*

*Force reading change per degree of temperature change = ±0.2%/°F (0.36%/°C)

Tekscan, Inc. 307 West First Street South Boston, MA 02127-1309 USA tel: 617.464.4500/800.248.3669 fax: 617.464.4266
e-mail: marketing@tekscan.com URL: www.tekscan.com

Tekscan

Rev N_9.30.13

Circuit

A comparator circuit was used to acquire the foot contact status of the robot. Fig. B.1 shows the designed comparator circuit. For each foot a LM324 operational amplifier was implemented to provide the ground contact status output. For, $\mathrm{R_1} = 0\ \Omega$ to $20\ \mathrm{k\Omega}$, the inverting input voltage of the operational amplifier is calculated as,

$$V(-) = \frac{\mathrm{VCC} \times \mathrm{R_2}}{\mathrm{R_2} + \mathrm{R_1}} = \frac{5\ \mathrm{V} \times 10\ \mathrm{k\Omega}}{10\ \mathrm{k\Omega} + \mathrm{R_1}} = 5 \text{ to } 1.67\ \mathrm{V}. \quad \text{(B. 1)}$$

For the force sensor output $\mathrm{R_s} = \infty\ \Omega$ to $0\ \Omega$, the non-inverting voltage input of the operational amplifier is calculated as,

$$V(+) = \frac{\mathrm{VCC} \times \mathrm{R_s}}{\mathrm{R_s} + \mathrm{R_3}} = \frac{5\ \mathrm{V} \times 10\ \mathrm{k\Omega}}{\mathrm{R_s} + 100\ \mathrm{k\Omega}} = 0 \text{ to } 5\ \mathrm{V}. \quad \text{(B. 2)}$$

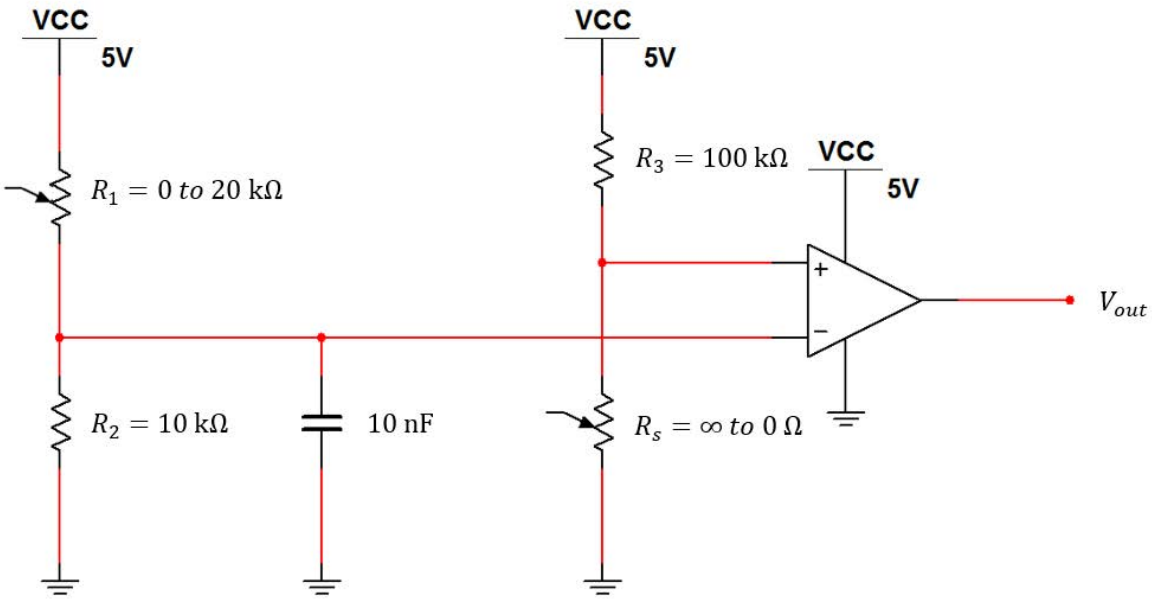

Figure B. 1: Comparator circuit with force sensors.

When the non-inverting voltage is higher than the inverting voltage, the operational amplifier's output voltage will be high. When the non-inverting voltage is lower than the inverting voltage, the operational amplifier's output will be zero. The output of each of the operational amplifiers were connected to general in-out pins on the UDOO.

REFERENCES

[1] L. Minati and A. Zorat, “A tree architecture with hierarchical data processing on a sensor-rich hexapod robot,” *Adv. Robot.*, vol. 16, no. 7, pp. 595–608, Jan. 2002.

[2] M. Bloesch, M. Hutter, M. A. Hoepflinger, S. Leutenegger, C. Gehring, C. D. Remy, and R. Siegwart, “State Estimation for Legged Robots-Consistent Fusion of Leg Kinematics and IMU.,” in *Robotics: Science and Systems*, 2012.

[3] N. Rotella, M. Bloesch, L. Righetti, and S. Schaal, “State Estimation for a Humanoid Robot,” in *arXiv preprint arXiv: 1402.5450*, 2014.

[4] Vicon, “Vicon.” [Online]. Available: www.vicon.com.

[5] M. H. Raibert, “Legged robots,” *Commun. ACM*, vol. 29, no. 6, pp. 499–514, May 1986.

[6] S. Bartsch, T. Birnschein, F. Cordes, D. Kühn, P. Kampmann, J. Hilljegerdes, S. Planthaber, M. Römmermann, and F. Kirchner, “Spaceclimber: Development of a six-legged climbing robot for space exploration,” in *Robotics (ISR), 2010 41st International Symposium on and 2010 6th German Conference on Robotics (ROBOTIK)*, 2010, pp. 1265–1272.

[7] Z. J. M. Ding Xilun, Wang Zhiying, Rovetta Alberto, “Locomotion Analysis of Hexapod Robot,” in *Climbing and Walking Robots*, B. Miripour, Ed. 2010, pp. 291–311.

[8] P. Gonzalez de Santos, J. a. Cobano, E. Garcia, J. Estremera, and M. a. Armada, “A six-legged robot-based system for humanitarian demining missions,” *Mechatronics*, vol. 17, no. 8, pp. 417–430, Oct. 2007.

[9] M. Ahmed, M. R. Khan, M. M. Billah, and S. Farhana, “A Novel Navigation Algorithm for Hexagonal Hexapod Robot,” *Am. J. Eng. Appl. Sci.*, vol. 3, no. 2, pp. 320–327, Feb. 2010.

[10] U. Asif and J. Iqbal, “An Approach to Stable Walking over Uneven Terrain Using a Reflex-Based Adaptive Gait,” *J. Control Sci. Eng.*, vol. 2011, pp. 1–12, 2011.

[11] O. Ekeberg, M. Blümel, and A. Büschges, “Dynamic simulation of insect walking.,” *Arthropod Struct. Dev.*, vol. 33, no. 3, pp. 287–300, Jul. 2004.

[12] M. Konyev, F. Palis, Y. Zavgorodniy, A. Melnikov, A. Rudskiy, A. Telesh, U. Schmucker, and V. Rusin, “Walking Robot ‘ANTON’: Design, Simulation, Experiments,” in *Advances In Mobile Robotics - Proceedings of the Eleventh International Conference on Climbing and Walking Robots and the Support Technologies for Mobile Machines*, 2008, pp. 922–929.

[13] A. Roennau, T. Kerscher, and R. Dillmann, “Design and kinematics of a biologically-inspired leg for a six-legged walking machine,” in *2010 3rd IEEE RAS & EMBS International Conference on Biomedical Robotics and Biomechatronics*, 2010, pp. 626–631.

[14] R. Siegwart, I. R. Nourbakhsh, and D. Scaramuzza, *Introduction to Autonomous Mobile Robots*, 2nd Editio. Cambrige, Massachusetts: The MIT Press, Massachusetts Institute of Technology, 2011.

[15] P. G. de Santos, E. Garcia, R. Ponticelli, and M. Armada, "Minimizing Energy Consumption in Hexapod Robots," *Adv. Robot.*, vol. 23, no. 6, pp. 681–704, Jan. 2009.

[16] D. Belter, P. Łabęcki, and P. Skrzypczyński, "Map-based adaptive foothold planning for unstructured terrain walking," in *2010 IEEE International Conference on Robotics and Automation*, 2010, pp. 5256–5261.

[17] D. Belter and P. Skrzypczynski, "Integrated Motion Planning for a Hexapod Robot Walking on Rough Terrain," in *Preprints of the 18th IFAC World Congress*, 2011, pp. 6918–6923.

[18] M. Schilling, T. Hoinville, J. Schmitz, and H. Cruse, "Walknet, a bio-inspired controller for hexapod walking.," *Biol. Cybern.*, vol. 107, no. 4, pp. 397–419, Aug. 2013.

[19] M. Grabowska, E. Godlewska, J. Schmidt, and S. Daun-Gruhn, "Quadrupedal gaits in hexapod animals - inter-leg coordination in free-walking adult stick insects.," *J. Exp. Biol.*, vol. 215, no. Pt 24, pp. 4255–66, Dec. 2012.

[20] K. Walas and D. Belter, "Messor-Versatile walking robot for search and rescue missions," *J. Autom. Mob. Robot. Intell. Syst.*, vol. 5, no. 2, pp. 28–34, 2011.

[21] B. H. Wilcox, "ATHLETE: A cargo and habitat transporter for the moon," in *2009 IEEE Aerospace conference*, 2009, pp. 1–7.

[22] A. Chilian, H. Hirschmuller, and M. Gorner, "Multisensor data fusion for robust pose estimation of a six-legged walking robot," in *2011 IEEE/RSJ International Conference on Intelligent Robots and Systems*, 2011, pp. 2497–2504.

[23] P.-C. Lin, H. Komsuoglu, and D. E. Koditschek, "Sensor data fusion for body state estimation in a hexapod robot with dynamical gaits," *IEEE Trans. Robot.*, vol. 22, no. 5, pp. 932–943, Oct. 2006.

[24] K. C. Galloway, G. C. Haynes, B. D. Ilhan, A. M. Johnson, R. Knopf, G. A. Lynch, B. N. Plotnick, M. White, and D. E. Koditschek, "X-RHex: A highly mobile hexapedal robot for sensorimotor tasks," 2010.

[25] A. M. Johnson, M. T. Hale, G. C. Haynes, and D. E. Koditschek, "Autonomous legged hill and stairwell ascent," in *2011 IEEE International Symposium on Safety, Security, and Rescue Robotics*, 2011, pp. 134–142.

[26] M. Kalakrishnan, J. Buchli, P. Pastor, and S. Schaal, "Learning locomotion over rough terrain using terrain templates," in *2009 IEEE/RSJ International Conference on Intelligent Robots and Systems*, 2009, pp. 167–172.

[27] A. Irawan and K. Nonami, "Force Threshold-Based Omni-directional Movement for Hexapod Robot Walking on Uneven Terrain," in *2012 Fourth International Conference on Computational Intelligence, Modelling and Simulation*, 2012, pp. 127–132.

[28] M. Kalakrishnan, J. Buchli, P. Pastor, M. Mistry, and S. Schaal, “Fast, robust quadruped locomotion over challenging terrain,” in *2010 IEEE International Conference on Robotics and Automation*, 2010, pp. 2665–2670.

[29] F. Delcomyn, “From Insect Sense Organs to Biomimetic Walking Robots [Exploratory DSP],” *IEEE Signal Process. Mag.*, vol. 25, no. 1, pp. 134–137, 2008.

[30] X. Zhao and Q. Luo, “Survey on robot multi-sensor information fusion technology,” in *2008 7th World Congress on Intelligent Control and Automation*, 2008, pp. 5019–5023.

[31] B. Siciliano and O. Khatib, *Springer Handbook of Robotics*. Berlin: Springer, 2008.

[32] U. Saranli, A. Avci, and M. C. Ozturk, “A Modular Real-Time Fieldbus Architecture for Mobile Robotic Platforms,” *IEEE Trans. Instrum. Meas.*, vol. 60, no. 3, pp. 916–927, Mar. 2011.

[33] S. Kaliyamoorthy and R. D. Quinn, “Force Sensors in Hexapod Locomotion,” *Int. J. Rob. Res.*, vol. 24, no. 7, pp. 563–574, Jul. 2005.

[34] G. A. Aydemir and A. Saranlı, “Characterization and calibration of MEMS inertial sensors for state and parameter estimation applications,” *Measurement*, vol. 45, no. 5, pp. 1210–1225, Jun. 2012.

[35] F. Caron, E. Duflos, D. Pomorski, and P. Vanheeghe, “GPS/IMU data fusion using multisensor Kalman filtering: introduction of contextual aspects,” *Inf. Fusion*, vol. 7, no. 2, pp. 221–230, Jun. 2006.

[36] a. Noureldin, R. Sharaf, a. Osman, and N. El-Sheimy, “INS/GPS data fusion technique utilizing radial basis functions neural networks,” *PLANS 2004. Position Locat. Navig. Symp. (IEEE Cat. No.04CH37556)*, pp. 280–284.

[37] M. Reinstein and M. Hoffmann, “Dead Reckoning in a Dynamic Quadruped Robot Based on Multimodal Proprioceptive Sensory Information,” *IEEE Trans. Robot.*, vol. 29, no. 2, pp. 563–571, Apr. 2013.

[38] T. Whelan, H. Johannsson, M. Kaess, J. J. Leonard, and J. McDonald, “Robust real-time visual odometry for dense RGB-D mapping,” in *2013 IEEE International Conference on Robotics and Automation*, 2013, no. i, pp. 5724–5731.

[39] B. Morisset, R. B. Rusu, A. Sundaresan, K. Hauser, M. Agrawal, J.-C. Latombe, and M. Beetz, “Leaving Flatland: Toward real-time 3D navigation,” in *2009 IEEE International Conference on Robotics and Automation*, 2009, pp. 3786–3793.

[40] A. Weckenmann, X. Jiang, K.-D. Sommer, U. Neuschaefer-Rube, J. Seewig, L. Shaw, and T. Estler, “Multisensor data fusion in dimensional metrology,” *CIRP Ann. - Manuf. Technol.*, vol. 58, no. 2, pp. 701–721, Jan. 2009.

[41] Z. Zhang, “Microsoft Kinect Sensor and Its Effect,” *IEEE Multimed.*, vol. 19, no. 2, pp. 4–10, Feb. 2012.

[42] B. Khaleghi, A. Khamis, F. O. Karray, and S. N. Razavi, “Multisensor data fusion: A review of the state-of-the-art,” *Inf. Fusion*, vol. 14, no. 1, pp. 28–44, Jan. 2013.

[43] J. Z. Sasiadek, “Sensor fusion,” *Annu. Rev. Control*, vol. 26, no. 2, pp. 203–228, Jan. 2002.

[44] H. Bostrom, S. F. Andler, M. Brohede, R. Johansson, A. Karlsson, J. van Laere, L. Niklasson, M. Nilsson, A. Persson, and T. Ziemke, “On the definition of information fusion as a field of research,” Institutionen för kommunikation och information, University of Skövde, Skövde, Tech. Rep. HS- IKI -TR-07-006, 2007.

[45] S. Manoiu-Olaru, M. Nitulescu, and V. Stoian, “Hexapod robot. Mathematical support for modeling and control,” in *System Theory, Control, and Computing (ICSTCC), 2011 15th International Conference on*, 2011, pp. 1–6.

[46] V. Dürr, J. Schmitz, and H. Cruse, “Behaviour-based modelling of hexapod locomotion: linking biology and technical application.,” *Arthropod Struct. Dev.*, vol. 33, no. 3, pp. 237–50, Jul. 2004.

[47] A. Schneider, J. Paskarbeit, M. Schaeffersmann, and J. Schmitz, “HECTOR, a new hexapod robot platform with increased mobility-control approach, design and communication,” in *Advances in Autonomous Mini Robots*, Springer Berlin Heidelberg, 2012, pp. 249–264.

[48] S. A. A. Moosavian and A. Dabiri, “Dynamics and planning for stable motion of a hexapod robot,” in *2010 IEEE/ASME International Conference on Advanced Intelligent Mechatronics*, 2010, pp. 818–823.

[49] A. Preumont, P. Alexandre, and D. Ghuys, “Gait analysis and implementation of a six leg walking machine,” in *Fifth International Conference on Advanced Robotics ’Robots in Unstructured Environments*, 1991, pp. 941–945 vol.2.

[50] S. K.-K. Chu and G. K.-H. Pang, “Comparison between different model of hexapod robot in fault-tolerant gait,” *IEEE Trans. Syst. Man, Cybern. - Part A Syst. Humans*, vol. 32, no. 6, pp. 752–756, Nov. 2002.

[51] “Trossen Robotics: PhantomX AX Hexapod Mark II Kit.” [Online]. Available: http://www.trossenrobotics.com/phantomx-ax-hexapod.aspx. [Accessed: 02-Oct-2013].

[52] “RobotShop: Lynxmotion T-Hex 18DOF Hexapod Walking Robot Kit.” [Online]. Available: http://www.robotshop.com/productinfo.aspx?pc=RB-Lyn-349&lang=en-US. [Accessed: 02-Oct-2013].

[53] “RobotShop: DFRobot Robot Hexapod Kit.” [Online]. Available: http://www.robotshop.com/productinfo.aspx?pc=RB-Dfr-125&lang=en-US. [Accessed: 02-Oct-2013].

[54] “DFRobot: Hexapod Robot Kit.” [Online]. Available: http://www.dfrobot.com/index.php?route=product/product&product_id=515#.UkvxcZ_cMQM. [Accessed: 02-Oct-2013].

[55] F. Orderud, “Comparison of kalman filter estimation approaches for state space models with nonlinear measurements.,” in *of Scandinavian Conference on Simulation and Modeling*, 2005, no. 7491, pp. 1–8.

[56] M. S. Arulampalam, S. Maskell, N. Gordon, and T. Clapp, “A tutorial on particle filters for online nonlinear/non-Gaussian Bayesian tracking,” *IEEE Trans. Signal Process.*, vol. 50, no. 2, pp. 174–188, 2002.

[57] K. György, A. Kelemen, and L. Dávid, “Unscented Kalman Filters and Particle Filter Methods for Nonlinear State Estimation,” *Procedia Technol.*, vol. 12, pp. 65–74, 2014.

[58] O. Welch and G. Bishop. "An introduction to the Kalman filter". Tech. Rep., UNC-CH Computer Science Technical Report 95041, 1995.

[59] E. Krotkov and R. Hoffman, “Terrain mapping for a walking planetary rover,” *IEEE Trans. Robot. Autom.*, vol. 10, no. 6, pp. 728–739, 1994.

[60] J. T. Machado and M. F. Silva, “An overview of legged robots,” in *International Symposium on Mathematical Methods in Engineering*, 2006.

[61] B. Gassmann, F. Zacharias, J. M. Zollner, and R. Dillmann, “Localization of Walking Robots,” in *Proceedings of the 2005 IEEE International Conference on Robotics and Automation*, 2005, no. April, pp. 1471–1476.

[62] J. Estremera, P. G. de Santos, and J. a. López-Orozco, “Neural virtual sensors for terrain adaptation of walking machines,” *J. Robot. Syst.*, vol. 22, no. 6, pp. 299–311, Jun. 2005.

[63] J. a. Cobano, J. Estremera, and P. Gonzalez de Santos, “Location of legged robots in outdoor environments,” *Rob. Auton. Syst.*, vol. 56, no. 9, pp. 751–761, Sep. 2008.

[64] S. Chitta, P. Vemaza, R. Geykhman, and D. D. Lee, “Proprioceptive localilzatilon for a quadrupedal robot on known terrain,” in *Proceedings 2007 IEEE International Conference on Robotics and Automation*, 2007, no. April, pp. 4582–4587.

[65] M. Reinstein and M. Hoffmann, “Dead reckoning in a dynamic quadruped robot: Inertial navigation system aided by a legged odometer,” in *2011 IEEE International Conference on Robotics and Automation*, 2011, pp. 617–624.

[66] H. Chao, C. Coopmans, L. Di, and Y. Chen, “A comparative evaluation of low-cost IMUs for unmanned autonomous systems,” in *2010 IEEE Conference on Multisensor Fusion and Integration*, 2010, pp. 211–216.

[67] D. Bhatt, P. Aggarwal, P. Bhattacharya, and V. Devabhaktuni, “An enhanced MEMS error modeling approach based on Nu-Support Vector Regression.,” *Sensors (Basel).*, vol. 12, no. 7, pp. 9448–66, Jan. 2012.

[68] M. De Agostino, A. M. Manzino, and M. Piras, “Performances comparison of different MEMS-based IMUs,” in *IEEE/ION Position, Location and Navigation Symposium*, 2010, pp. 187–201.

[69] D. Gebre-Egziabher, “Modeling and bounding low cost inertial sensor errors,” in *2008 IEEE/ION Position, Location and Navigation Symposium*, 2008, pp. 1122–1132.

[70] A. Noureldin, T. B. Karamat, M. D. Eberts, and A. El-Shafie, “Performance Enhancement of MEMS-Based INS/GPS Integration for Low-Cost Navigation Applications,” *IEEE Trans. Veh. Technol.*, vol. 58, no. 3, pp. 1077–1096, Mar. 2009.

[71] J. Fraden, *Handbook of Modern Sensors*, 4th ed. New York, NY: Springer New York, 2010.

[72] J. Craig, John, *Introduction to robotics: mechanics and control*, 3rd ed. Pearson Education Limited, 2005.

[73] Tekscan, “Tekscan, FlexiForce Sensors.” [Online]. Available: http://www.tekscan.com/flexible-force-sensors. [Accessed: 17-Sep-2014].

[74] “LORD Microstrain sensing systems, Inertial sensors.” [Online]. Available: http://www.microstrain.com/inertial/3DM-GX3-25. [Accessed: 17-Sep-2014].

[75] UDOO, “UDOO.” [Online]. Available: http://www.udoo.org/. [Accessed: 17-Sep-2014].

[76] Microstrain, “3DM-GX3-15 3DM-GX3-25 Mounting Diagram.” [Online]. Available: http://files.microstrain.com/3DM-GX3-15 3DM-GX3-25 Mounting Diagram.pdf. [Accessed: 17-Sep-2014].

[77] “Trossen robotics: Dynamixel servos.” [Online]. Available: http://www.trossenrobotics.com/dynamixel-ax-12-robot-actuator.aspx. [Accessed: 17-Sep-2014].

[78] E. Tira-Thompson, "Digital servo calibration and modeling," Robotics Institute, Pittsburgh, PA, Tech. Rep. CMU-RI-TR-09-41, March 2009.

[79] MicroStrain Inc., “3DM-GX3-25 Miniature Attitude Heading Reference System Data Sheet.” [Online]. Available: http://files.microstrain.com/3DM-GX3-25-Attitude-Heading-Reference-System-Data-Sheet.pdf.

[80] MicroStrain Inc., “3DM-GX3-25 single byte data comunication protocol.” [Online]. Available: http://files.microstrain.com/3DM-GX3-25 Single Byte Data Communications Protocol.pdf.

[81] A. Papoulis and S. U. Pillai, *Probability, random variables, and stochastic processes*, 4th ed. McGraw-Hill, 2002.

[82] J. Diebel, “Representing attitude: Euler angles, unit quaternions, and rotation vectors,” Stanford Univ., Stanford, CA, Tech. Rep., 2006

[83] N. Trawny and S. I. Roumeliotis, “Indirect Kalman filter for 3D attitude estimation,” University of Minnesota, Dept. of Comp. Sci. & Eng., Tech. Rep. 2005-002, Mar. 2005.

[84] N. Trawny and S. I. Roumeliotis, “Indirect Kalman Filter for 3D Attitude Estimation,” 2005.

[85] J. Gallier and D. Xu, “Computing exponentials of skew-symmetric matrices and logarithms of orthogonal matrices,” *Int. J. Robot. Autom.*, vol. 17, no. 4, 2002.

[86] J. Sola, “Quaternion kinematics for the error-state KF,” 2014. [Online]. Available: http://www.iri.upc.edu/people/jsola/JoanSola/objectes/notes/kinematics.pdf.

[87] P. Furgale, J. Maye, J. Rehder, and T. Schneider, “IMU Noise Model and Intrinsics,” 2014. [Online]. Available: https://github.com/ethz-asl/kalibr/wiki/IMU-Noise-Model-and-Intrinsics.

[88] Trossen Robotics, “PhantomX Hexapod Phoenix Code.” [Online]. Available: http://learn.trossenrobotics.com/10-interbotix/crawlers/phantomx-hexapod/68-phoenix-code.